University of Alberta

Ultrasonic Dispersion of Cylindrical Guided Waves in Bovine Tibia

by

Luning Wang 

A thesis submitted to the Faculty of Graduate Studies and Research
in partial fulfillment of the requirements for the degree of

Master of Science

Department of Radiology and Diagnostic Imaging

Department of Mechanical Engineering

Edmonton, Alberta
Spring 2008

Your file Votre référence
ISBN: 978-0-494-45904-1
Our file Notre référence
ISBN: 978-0-494-45904-1

Abstract

Guided waves have been observed to travel long distance through thickness in long bones and potentially provide valuable information about bone properties and microstructures. In this work, cylindrical ultrasound guided waves in bovine tibia using axial transmission technique were investigated. Numerical simulation and phantom data were used to verify the analytic procedures and complement the study. The 2-D power spectrum of the bone data was estimated using the periodogram. The spectral results showed four distinct energy clusters. Theoretical dispersion curves based on a viscoelastic cylindrical tube filled with liquid were computed to assist the modal identification. Four high-order longitudinal cylindrical guided wave modes were identified to associate with the clusters. The time signatures of the two strongest modes demonstrated dispersive wave trains, which were in agreement with the theoretical results. This study demonstrated that cylindrical longitudinal guided waves were dominant in bovine tibia at large distance from the transmitter.

To my parents and my wife

Acknowledgements

I will give my sincerest and deepest thanks and gratitude to my supervisors, Dr. Lawrence. H. Le and Dr. Ben P.-Y. Ben Jar, for their patient guidance, constant interests and encouragements throughout the duration of my graduate work. Especially thanks to Dr. Le for his creating the atmosphere of shared learning which is so important for true learning. He gives the opportunity for me to enter into a new physical world. Also my thanks to Dr. Le for his help and support on my personal life. This thesis would not have been conceivable without your helping and suggestions.

My thanks also to Dr. Mauricio. D. Sacchi who gave me guidance on my work. I deeply appreciate his interest, advice and encouragement throughout the project. His eager involvement and insight were invaluable. I give my thanks to Dr. Dean Ta at Fudan University, China. I learned a lot and have benefited from the discussion with him during his staying in our lab. I owe my thanks to Dr. Edmond Lou for his supporting the work.

I am also grateful to Miss Rui Zheng in our Ultrasonic Material Characterization and Imaging Laboratory for her immeasurable contributions to my work. I also thank to Mr. Chengye Fan and Mrs. Tik Man Dick of the Department of Mechanical Engineering for their help: they are.

I thank the following departments and organizations for providing financial assistance: Department of Radiology and Diagnose Imaging, Department of Mechanical Engineering University of Alberta, NSERC, Capital Health and Edmonton Orthopedic Research Committee.

My thanks due again to Dr. Jingli Luo in Department of Chemical Engineering at University of Alberta for her supporting and understanding during the preparation of this thesis in the first term of my PhD study.

Finally but not least, my thanks to my parents and my wife for their understanding, supporting and unwavering faith in me throughout the duration of my work. My thesis is dedicated to you all.

Table of Contents

Chapter 1 Introduction 1
1.1 Bone tissue 1
1.2 Bone structure 1
1.3 Osteoporosis 3
1.4 Current radiation-based methods 4
1.5 Ultrasonic techniques to study bone 5
1.5.1 Transverse transmission techniques 6
1.5.2 Axial transmission technique 7
1.6 Objectives and outlines of this thesis 10

Chapter 2 Propagation of Guided Waves in Plate and Fluid-Filled Cylinder 11
2.1 Guided wave propagation in a free plate 12
2.1.1 Symmetric modes 14
2.1.2 Antisymmetric modes 17
2.2 Guided wave propagation in fluid-filled cylinders 18
2.3 From elasticity to anelasticity 31
2.4 Calculating the dispersion curves 32

Chapter 3 Spectral Estimation of Ultrasound Signals 34
3.1 Periodogram method 34
3.2 Autoregressive (AR) estimation 36

Chapter 4 Experimental Studies of Ultrasound Propagation in Phantom and Bovine Tibia 44
4.1 Experimental setup and materials 45
4.1.1 Experimental setup and data acquisition 45
4.1.2 Phantom specimen 46
4.1.3 Bone specimen 47

4.2 Discussion of Experimental Results 47
4.2.1 Phantom data 47
4.2.2 Bone specimen 51

Chapeter 5 Conclusions and Some Comments on Future Direction 75

Bibliography 75

Appendix A Some Fundamentals Relevant to Ultrasound Wave Propagation 84
A.1 Stress and strain 84
A.2 Equations of motion 86
A.3 Wave motion and particle polarization 88
A.3.1 Longitudinal wave 89
A.3.2 Shear wave 89
A.4 Reflection and transmission of P-SV waves across a solid-solid interface 91

Appendix B The Cylindrical Coordinates 100
B.1 The Laplacian 100
B.2 Stress and strain components 101

Appendix C Bessel functions and the derivatives 103
C.1 Bessel functions 103
C.2 Derivatives of Bessel functions 105
C.3 Derivatives of modified Bessel functions 105

Appendix D On the Coefficient Matrix D 107
D.1 The element D_{ij} 107
D.2 The determinant of D when $n = 0$ 113

List of Tables

Figure 2.1 Choice of the functions Z_n and W_n (Gazis, 1959; Rose, 1999; Pavlakovic and Lowe, 2001). Equation (2.60) defines p^2 and q^2 23

Figure 4.1 Parameters of the bone model used to generate dispersion curves 53

Figure 4.2 Parameters of the phantom model used to generate dispersion curves 53

List of Figures

Figure 1.1 A sketch of cortical and trabecular bone 2

Figure 1.2 Comparison of normal bone and bone with osteoporosis 4

Figure 1.3 A Schematic of transverse transmission technique 7

Figure 1.4 A schematic diagram of an experimental setup: (1) transmitter and (2) receiver 8

Figure 1.5 A schematic diagram of propagation of guided waves in layered materials 9

Figure 2.1 Geometry of a plate 12

Figure 2.2 Schematics of the deformation of the plate and particle movement directions of (a) symmetric and (b) antisymmetric modes of wave propagation 15

Figure 2.3 Geometry of a fluid-filled cylindrical tube 19

Figure 3.1 1-*D* Hamming window with window length $L = 7$, 11, and 15 40

Figure 3.2 2-*D* Hamming window with window length $L = 11$ 40

Figure 3.3 Power spectral densities: (a) periodogram; (b) AR estimation of $p=15$; (c) AR estimation of $p=25$; (d) AR estimation of $p=40$ 42

Figure 3.4 Comparison of *k*-spectra at 0.375 MHz from Figure 3.3 (a)-(d): (a) Spectra normalized by the maximum value of the spectrum from periodogram; (b) self-normalized spectra 43

Figure 4.1 Theoretical dispersion curves of guided waves: (a) cylindrical longitudinal modes; (b) Lamb modes. The cylindrical tube model was an elastic bone model with parameters given in Table 4.1. The plate model was an 8.9 mm thick plate with the same velocities and density as those of the bone model. The asterisk (*) in (a) denotes previous works using cylindrical tube model; otherwise, plate model was used ([1]-[5] indicates Nicholson, *et al*, 2002, Lefebvre, *et al*, 2002, Protopappas, et al, 2006, Lee and Yoon, 2004, Ta, *et al*, 2006, respectively) 54

Figure 4.2 Experimental setup: (a) overview of experimental setup; (b) setup for phantom; (c) setup for bovine tibia 56

Figure 4.3 A nylon tube; the vertical bars indicate the region of investigation 57

Figure 4.4 An x-ray computed tomographic image of the bovine tibia. The vertical bars indicate the region of investigation 57

Figure 4.5 Echogram of the phantom data: (a) original data without normalized; (b) self normalized data 58

Figure 4.6 Self-normalized echograms of phantom dataset with 4 mm interval shown in Figure 4.5(b). The theoretical arrival time of the bulk compressional wave, bulk shear wave and Rayleigh wave are superimposed 59

Figure 4.7 Echogram of the phantom data: (a) before muting. The red line indicates the cut off of the muting window; (b) after muting 60

Figure 4.8 The 2-D periodogram of the phantom data 61

Figure 4.9 Theoretical dispersion curves of longitudinal guided wave modes of a nylon tube. The parameter is given by the phantom model in Table 4.2 .62

Figure 4.10 The dispersion diagram of phantom superimposed by the theoretical dispersion curves. The parameters of the phantom model used are given in Table 4.2 63

Figure 4.11 128-points Tukey tapers with different *r*-values 64

Figure 4.12 Source signals: (a) real signal (Panametrics C548) and (b) simulated wavelet by Disperse 65

Figure 4.13 The time signatures of different guided wave modes measured at 53 mm offset: (a-b) experimental data after bandpass filtering; (c-d) simulation. The parameters used for simulation are given by the phantom model in Table 1. The real amplitudes can be obtained by multiplying the displayed amplitudes by the respective scaling factors: (a) 0.029, (b) 0.053, (c) 0.4, and (d) 0.72. P1 and P2 refer to the two strongest clusters in Figure 4.10 66

Figure 4.14 Simulated data: dispersion diagram superimposed by the theoretical dispersion curves. The parameters of the phantom model used are given in Table 4.2 67

Figure 4.15 Echogram of the bovine tibia data: (a) original data without normalized; (b) self normalized data 68

Figure 4.16 Echogram of measurements of bovine tibia with a spacing interval of 4 mm: (a) real signals; (b) self-normalized signals. The theoretical arrival time of the bulk compressional wave, bulk shear wave and Rayleigh wave are superimposed 69

Figure 4.17 Echogram of the bovine tibia data: (a) before muting. The red line indicates the cut off of the muting window; (b) after muting 70

Figure 4.18 The 2-D periodogram of bovine tibia 71

Figure 4.19 Theoretical dispersion curves of longitudinal guided waves mode in bovine tibia. The parameters used are given in Table 4.1: (a) without attenuation; (b) with attenuation 72

Figure 4.20 The dispersion diagram of bovine tibia superimposed by the theoretical dispersion curves. The parameters of the bone model used are given in Table 4.1 73

Figure 4.21 The time signatures of different guided wave modes measured at 53 mm offset: (a-b) experimental data after bandpass filtering; (c-d) simulation. The parameters used for simulation are given by the bone model in Table 1. The real amplitudes can be obtained by multiplying the displayed amplitudes by the respective scaling factors: (a) 0.01, (b) 0.0048, (c) 0.14, and (d) 0.08. B1 and B2 refer to the two strongest clusters in Fig. 4.19 74

Figure A.1 Stress components acting on the surface of a cubic volume element 86

Figure A.2 Geometry and polarization of *S*-wave 90

Figure A.3 Interaction of *P-SV* waves at the boundary of two solid-solid half-spaces: (a) Downgoing incident *P*-wave; (b) Downgoing incident *SV*-wave; (c) Upgoing incident *P*-wave; (d) Upgoing incident *SV*-wave 93

List of Abbreviations

1-*D*	One dimension
2-*D*	Two dimension
AR	Auto regressive
FAS	First arrival signal
FFT	Fast Fourier transforms
LAS	Late arrival signal
NDE	Nondestructive evaluation
PSD	Power spectrum density

Chapter 1

Introduction

1.1 Bone tissue

The bone tissue is a matrix surrounding widely separated cells. The matrix is contained about 25 % water, 25 % protein fibers, and 50 % mineral salts (Tortora and Grabowski, 1992). There are four major types of bone cells: osteoprogenitor cells, osteoblasts, osteocytes and osteoclasts. Osteoprogenitor cells are general cells and can undergo mitosis and develop into osteoblasts. Osteoblasts are cells that form from bone and can secrete collagen and other organic components to build bone. Osteocytes are major cells of bone tissue and are derived from osteoblasts which are usually found on the surfaces of bone and maintain daily cellular activities of bone tissue. Osteoclasts are developed from circulating monocytes and settle on the surfaces of bone and function in bone resorption (Tortora and Grabowski, 1992).

1.2 Bone structure

Bone is a composite material composed of organic and inorganic phases. By weight, approximately 70% of the tissue is mineral or inorganic matter, water composes 5% to 8%, and the organic or extracellular matrix makes up the reminder. Bones come in many shapes and sizes, and at a macroscopic level bone can be classified according to shape. Four principal types can be identified: long bones (e.g. humerus, femur, radius); short bones (metacarpal and phalanx); flat bones (skull and ribs); and irregular bones (vertebrae). Anatomically, two forms of bone are distinguishable: the cortical and the trabecular bone. The cortical bone appears as a solid continuous mass in which spaces can be viewed only with the aid of a

microscope. Eighty percent of skeletal bone mass is cortical bone; but, because of its density, it has small surface area. Trabecular bone (also called spongy bone) is an inner spongy structure that resembles honeycomb, which has a relatively large surface area, but forms a smaller portion of the skeleton, accounting for twenty percent of bone mass. The solid part of cancellous bone is called trabecular bone. The spaces between the trabecular bones are filled with bone marrow, which consists of fat and cellular components of blood constituents. Cortical bone has four times the mass of trabecular bone, although the metabolic turnover rate of trabecular bone is eight times faster than that of cortical bone because bone turnover is a surface event, and trabecular bone has a greater surface area than cortical bone. Functionally, cortical bone mainly fulfills the mechanical and protective functions, and trabecular bone the metabolic function (Njeh, *et al*, 1999; Bone Anatomy Review, 1999; Tortora and Grabowski, 1992). Figure 1.1 displays a sketch of the cortical and trabecular part of bone.

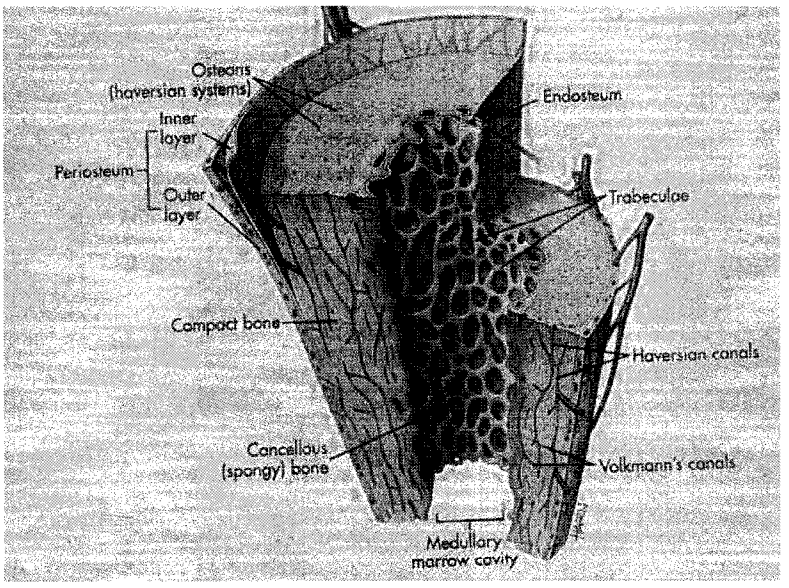

Figure 1.1 A sketch of cortical and trabecular bone (taken from http://137.222.110.150/calnet/musculo/page3.htm)

1.3 Osteoporosis

Osteoporosis, which is a worldwide metabolic bone disease, is characterized by reduced bone mass and deteriorated microstructure of bone tissue (Njeh *et al*, 1999). A panel from the National Institute of Health Consensus Conference defined osteoporosis as 'a disease characterized by low bone mass and microarchitectural deterioration of bone tissue, leading to enhanced bone fragility and a consequent increase in fracture risk' (Official website of International Osteoporosis Foundation, 2007). Based on statistical results, 1.4 million Canadians suffer from osteoporosis. One in four women and one in eight men over the age of 50 has osteoporosis (Brown *et al*, 2002). However, the disease can strike at any age. The cost of treating osteoporosis and the bone fractures due to osteoporosis is estimated to be $1.9 billion each year in Canada alone (Official website of Osteoporosis Canada, 2007). Long term, hospital and chronic care account for the majority of these costs. Given the increasing proportion of older people in the population, these costs will likely rise.

The disease of osteoporosis is a silent, progressive, skeletal disorder characterized by compromised bone strength pertaining to an increased risk of fracture. Bone strength reflects the integration of two main features: bone density and bone quality. Bone density is expressed as grams of mineral per area or volume. Bone quality refers to architecture, turnover, damage accumulation (e.g., micro fractures) and mineralization (NIH Consensus Statement, 2000). Research shows that osteoporosis mostly affects the structure of cancellous bone. Figure 1.2 shows the comparison of normal bone and bone with osteoporosis. Recent study (Copper, *et al*, 2006) shows that osteoporosis also arises from cortical thinning. Figure 1.3 shows the comparison of normal cortical bone and cortical thinning due to osteoporosis.

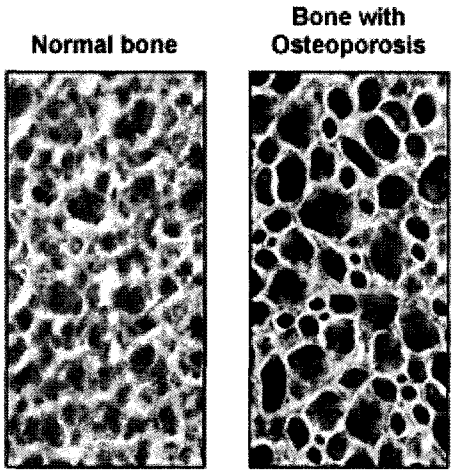

Figure 1.2 Comparison of normal bone and bone with osteoporosis (taken from http://www.osteopathy.com.sg/).

Osteoporosis can be detected from the changing of the structure of trabecular bone (Njeh, *et al*, 1999) or thinning of cortical bone (Copper, *et al*, 2006). Therefore a study of the changing of cortical bone can be used to assess and monitor the degree of osteoporosis.

1.4 Current radiation-based methods

Current radiation-based methods to study osteoporosis include radiographic photo-densitometry, radiographic absorptiometry, single photon absorptiometry (SPA), dual photon absorptiometry (DPA), dual energy X-ray absorptiometry (DEXA), peripheral DXA, and quantitative computed tomography (QCT) (Bonnick and Lewis, 2002). All these methods are based on photon absorptiometry techniques. The difference in the attenuation of the photon energy by different tissues is responsible for the contrast on the film. The SPA and DPA use the radioactive isotope source of photon energy, which has one photoelectric peak for SPA or have two photoelectric peaks for DPA to separate bone from soft tissue. Today, DEXA has effectively replaced DPA in both research and clinical practice (Yu, 2005). The

underlying principles of DEXA are the same as those of DPA, but radioactive isotope is replaced by X-ray source. The benefits are dramatically shorter scan times and there is no source decay. QCT uses X-ray source to perform computed tomography and provides a 3D measurement of bone density. The drawbacks of these techniques are the radiation dose and the unavailability of the expensive setup for routine use (Sievänen, *et al*, 1996). Furthermore, these methods can not provide the architectural information or elasticity of the bone, which are important for bone strength determination (Njeh, *et al*, 1999).

1.5 Ultrasonic techniques to study bone

Ultrasonic nondestructive evaluation (*NDE*) testing methods were used extensively in defect detection in structures and material characterization (Rose, 1999; Kundu, 2004). Ultrasonic techniques have widely been applied to study skeletal system for over four decades. It has the advantages over those radiation-based methods due to its portability, lack of radiation, ease of use, and low cost. Moreover, previous research results have shown that quantitative ultrasound (QUS) holds promise to provide the elastic stiffness information and evaluate bone strength noninvasively (Laugier, 2006; Siffert and Kaufman, 2007; Glüer, 2007).

Ultrasound is mechanical wave and its propagation is affected by the density, elasticity and micro-architectures of bones. Propagation velocity and attenuation are two major parameters for ultrasound assessment on bone. Theismann and Pfander (1949) firstly reported the ultrasonic attenuation coefficient and propagation speed in human skull (Ji, 1998). Yoon and Katz (1976) firstly reported the elastic stiffness of cortical bone of human femur by using ultrasound. They found out the elastic stiffness of human femur was with about 1×10^{10} N/m^2. Behari and Singh (1981) detected the ultrasound propagation in '*in vivo*' long bone. The velocity of ultrasound of long bone was 3500 m/s with the attenuation coefficient 12 dB/MHz/cm. Ashman and his collegues (1987, 1988) reported the Young's modulus of cancellous bone along the bearing axis using both contact pulse transmission and continuous wave

techniques. Their results showed that Young's modulus obtained by ultrasound was about 23 MPa and was accurate than traditional mechanical methods. Rho (1996) measured the elastic properties of human cortical and cancellous bones along the axial, circumferential and radial direction. His results showed the axial direction with largest Young's modulus and the radial direction with least one. Lowet and Perre (1996) produced the method to measure the velocity of bone and proved that the bulk compressional wave velocity in bone is about 4000 m/s. They also simulated the fracture and healing period of long bone and obtained the expression to calculate the velocity on injury bone.

1.5.1 Transverse transmission techniques

Langton, *et al* (1984) firstly proposed the application of ultrasonic technique in clinical diagnosis of osteoporosis. The technique is displayed in Figure 1.3 and is so-called transverse transmission technique. The method proposed is called broadband ultrasonic attenuation (BUA). In this technique, two broadband ultrasonic transducers with 1 MHz center frequency were set in a water tank, one serving as a transmitter and the other as a receiver. The heel (mostly cancellous bone) was placed in the water bath between two transducers and the attenuation of the beam through the cancellous bone was measured relative to water alone. The BUA essentially measures insertion loss, found by comparing the amplitude spectrum of an ultrasonic pulse through bone with that through a reference medium, typically water. The term BUA is the gradient in dB/MHz, evaluated by linear regression. Results obtained by Langton and his colleagues showed that BUA value was higher for those healthy bone than that of osteoporotic bone. Following Langton, *et al*'s work, transverse transmission technique and BUA value of bone have been focused by a number of researchers. Strelitzki, *et al* (1996), Nicholson, *et al* (1996) and Droin, *et al* (1998) found out that negative dispersion happened in majority of bone samples. Chaffaï, *et al* (2000) and Wear (2001) showed that the BUA approximately depended linearly on

frequency and BUA gradient is considered to be diagnostic to osteoporosis (Fellah, 2004).

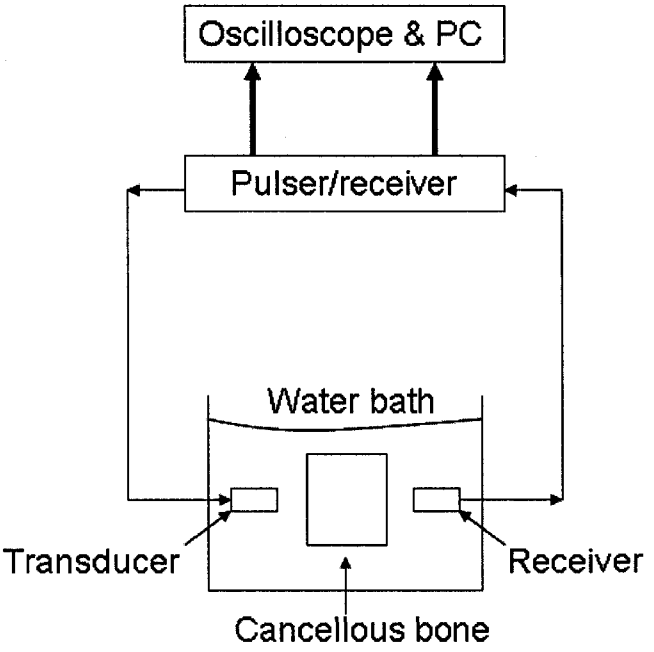

Figure 1.3 A Schematic diagram of transverse transmission technique.

1.5.2 Axial transmission technique

Recently, axial transmission techniques have been applied on ultrasonic measurement on studying long bones such as femur and tibia (Saulgozis *et al*, 1996; Bossy *et al*, 2002; Lee and Yoon, 2004; Moilanen, *et al*, 2006, 2007; Zheng, *et al*, 2007). This technique requires the source and receiver transducers located on the same side of the bone. The time signals can be obtained by these two transducers fixed with a constant distance or different locations by moving the receiver away from the source. Figure 1.4 portraits the schematic of axial transmission setup and the positions of two transducers.

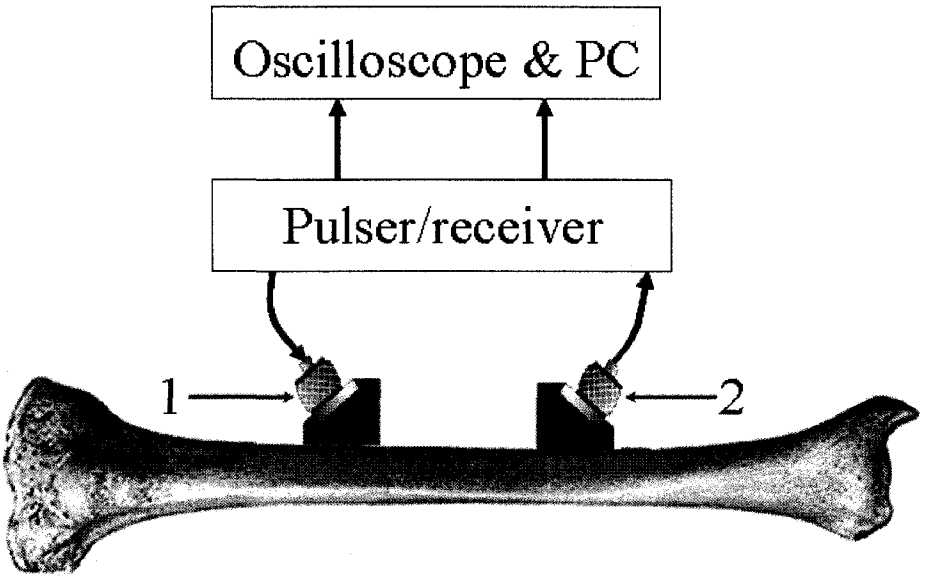

Figure 1.4 A schematic diagram of an experimental setup: (1) transmitter and (2) receiver.

Using axial transmission technique, Camus and his colleagues (2000) studied the lateral wave (head wave) in '*in vivo*' bone and found out that it had a potential to evaluate the mechanical properties of cortical bone. Other researchers (Nicholson, *et al*, 2002; Tatarinov, *et al*, 2005; Dodd, *et al* 2007) applied axial transmission technique to obtain the first arriving signal (*FAS*) of both *in vivo* and *in intro* of ultrasound in cortical bone. In their results, *FAS* was captured by dividing distance of wave propagation by bulk wave velocity in cortical bone and the incline of cortical bone was also considered during calculation. The *FAS* was a simple method to assess the cortical bone property. However, *FAS* failed to work when the wavelength was large and comparable to the cortical thickness (Nicholson, *et al*, 2002; Moilanen, *et al*, 2004). Lefebvre, *et al* (2002) established a method to obtain the echographic matrix signals using axial transmission method and applied bidimensional Fourier transform for bone characterization. Their method was also able to evaluate the mechanical properties like Young's modulus and cortical bone thickness.

In recent years, guided wave (Rose, 1999; Kundu, 2004) propagation was paid more attention onto ultrasonic measurement in long bone (Lefebvre, *et al*, 2002;

Moilanen, *et al*, 2004; Ta, *et al*, 2006). Guided wave was firstly applied in mechanical engineering for nondestructive evaluation (*NDE*) (Viktorov, 1967). The generation of guided wave is because of multiple reflections and interaction of bulk longitudinal and shear wave during propagation between the layers of materials (Rose, 1999; Kundu, 2004). Figure 1.5 shows the schematic of guided wave propagation in a layered material. Former studies showed that guided wave has the advantages on long track propagation. It can bring more information on bones during propagation.

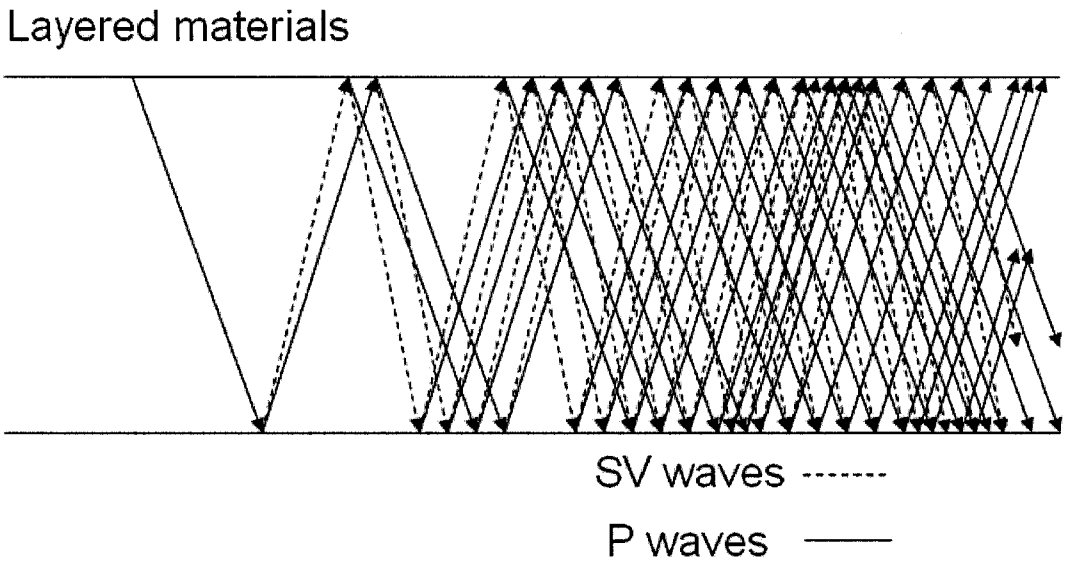

Figure 1.5 A schematic diagram of propagation of guided waves in layered materials.

Lamb wave is the fundamental form of guided wave propagating in plate (Viktorov, 1967). Detailed derivation of guided wave will be shown in chapter 2. Some researchers showed that Lamb wave with plate model was closed to cylindrical guided wave for those cortical bone samples with thinner outer shell (Lefebvre, *et al*, 2002; Protopappas, *et al,* 2006). So they selected Lamb wave to deal with the problems. Lefebvre, *et al* (2002) and Lee and Yoon (2004) applied plate model to mimic cortical bone. Their results showed that the lowest antisymmetric Lamb mode

(A0) and the lowest symmetric mode (S0) were the most dominant modes guided wave during propagation in long bone with thin cortical shell. Nicholson, *et al* (2002) also found out that phase velocity of A0 and S0 modes were sensitive with the change of cortical thickness. Protopappas, *et al* (2006) showed that Lamb wave other than lowest antisymmetric and symmetric modes, such as S2 and A3 were also dominant during wave propagation either in healthy or healing cortical bone.

Guided waves propagating in cylinders are more complicated than those in plate. Ta, *et al* (2006) firstly reported to apply a hollow elastic cylindrical tube model to mimic the long bone and study the ultrasonic wave propagation in long bone. They found out that two low order longitudinal guided wave modes, L(0,2) and L(0,3), were with dominant energy during propagation in hollow long bone. However, there is shortcoming of plate model and hollow cylinder model due to thoughtless with multilayer of cortical bone and marrow as well as the attenuation of cortical bone and morrow. The difference among plate model, hollow bone model and fluid-filled bone model, especially for bone samples with thick cortical part was significant.

1.6 Objectives and outlines of this thesis

The objectives of this thesis are to use a cylinder model to study guided waves propagating in bovine bone. The model that is used to interpret phantom and bone data is a liquid-filled cylindrical tube. The outline of the thesis is as follows. Chapter 1 provides a brief introduction of bone tissues and structures. This chapter also overviews the application of ultrasound in bone study. Chapter 2 provides, as a review, a detailed theoretical derivation of guided wave propagation in free plate and liquid-filled cylindrical tube. Dispersion relations will be derived to compute dispersion characteristics. Chapter 3 discusses the signal processing methods to interpret the experimental data. The periodogram and autoregressive (*AR*) method to estimate power density spectrum was compared. Discussions of experimental data obtained from phantom and bovine tibia will be given in Chapter 4. This thesis will be concluded in chapter 5 with brief discussion of future direction.

Chapter 2

Propagation of Guided Waves in Plate and Fluid-Filled Cylinder

Propagation in ultrasonic guided wave propagation in bone has been studied in recent years (Bossy, *et al*, 2002; Lefebvre, *et al*, 2002; Nicholson, *et al*, 2002; Tatarinov, *et al*, 2005; Propotpappas, *et al*, 2006; Dodd, *et al*, 2007). In most works, long bone was modeled by a free plate (Propotpappas, *et al*, 2006) bounded below and above by air or a plate overlying water, which mimics marrow. Lamb modes such as A0, S0 and S2 have been observed in experimental data (Nicholson, *et al*, 2002; Lee and Yoon, 2004; Tatarinov, *et al*, 2005; Propotpappas, *et al*, 2006). Lamb wave theory provides a simplistic model to understand interaction of guided waves with bone tissues. Long bones are effectively irregular cylindrical tubes filled with marrow. Guided wave propagation in cylindrical tube is a complex wave phenomenon. Guided wave energy from the cortical bone leaks into the underlying marrow and the leaked energy will be reflected back to the overlying cortex. The reflection of the leaked energy influences the characteristics of the modal dispersion. Based on this argument, free plate theory will perhaps underestimate the effects of the underlying marrow on the dispersion characteristics (Lefebvre, *et al*, 2002; Ta, *et al*, 2006).

In this chapter, starting with the first principles, the dispersion relationships of plane guided waves in plates and cylindrical guided waves in a fluid-filled cylinder will be derived.

2.1 Guided wave propagation in a free plate

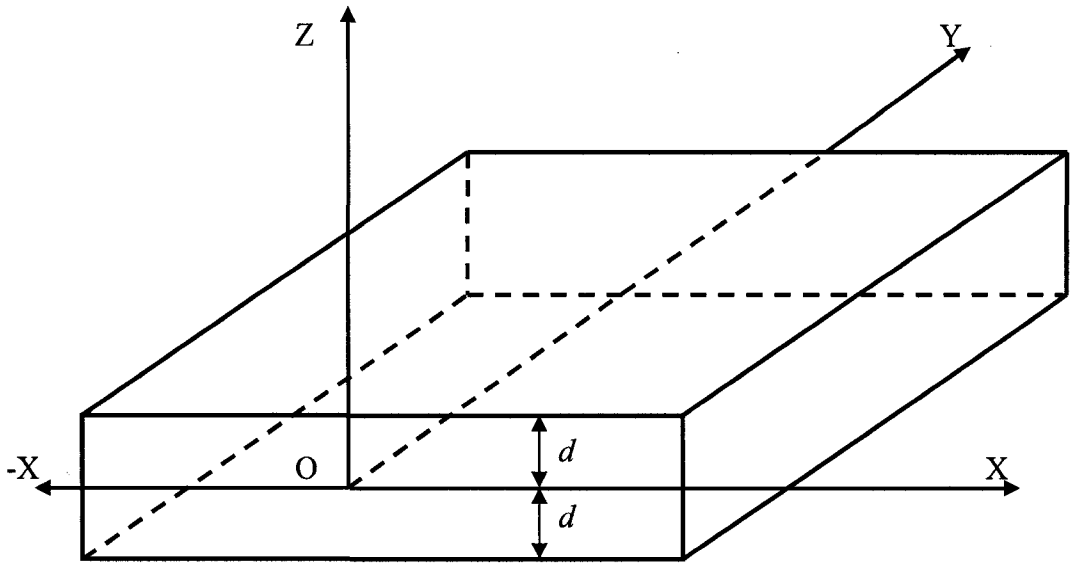

Figure 2.1 Geometry of a plate.

Figure 2.1 displays the geometry of a plate. The density, longitudinal and shear wave velocity are denoted respectively by ρ, c_L and c_S. The plate has a finite thickness $2d$ in the z-direction but extends infinitely along the x- and y-direction. A Cartesian coordinate system is placed in the midplane of the plate. The two horizontal planes normal to the z-axis are stress-free at $z = \pm d$. The plate with a stress-free condition is known as a free plate.

Longitudinal and shear wave motions confined in the x-z plane propagating along the x-direction were considered. In terms of the potentials, ϕ and ψ, the displacement $\vec{f} = (u, v, w)$ within the plate is (Appendix A.3)

$$\vec{f} = \nabla\phi + \nabla \times (0, \psi, 0) \tag{2.1}$$

where the first term is curl-free and the second term is divergence-free. The corresponding displacement components are

$$u = \frac{\partial \phi}{\partial x} + \frac{\partial \psi}{\partial z} \quad ,$$

$$v = 0 \quad , \tag{2.2}$$

$$w = \frac{\partial \phi}{\partial z} - \frac{\partial \psi}{\partial x} \quad ,$$

and the stress components are

$$T_{zx} = T_{xz} = \mu\left(\frac{\partial w}{\partial x} + \frac{\partial u}{\partial z}\right) = \mu\left(\frac{\partial^2 \phi}{\partial x \partial z} - \frac{\partial^2 \psi}{\partial x} + \frac{\partial^2 \psi}{\partial z}\right) \tag{2.3}$$

and

$$T_{zz} = \lambda\left(\frac{\partial u}{\partial x} + \frac{\partial w}{\partial z}\right) + 2\mu\left(\frac{\partial w}{\partial z}\right) = \lambda\left(\frac{\partial^2 \phi}{\partial x^2} + \frac{\partial^2 \psi}{\partial z^2}\right) + 2\mu\left(\frac{\partial^2 \phi}{\partial z^2} - \frac{\partial^2 \psi}{\partial x \partial z}\right) \quad . \tag{2.4}$$

We assume ϕ and ψ take the following form (Rose, 1999 and Kundu, 2003)

$$\phi(x,z,t) = \left[A_1 \sin(pz) + A_2 \cos(pz)\right] \exp\left[i(kx - \omega t)\right] \tag{2.5}$$

and

$$\psi(x,z,t) = \left[B_1 \sin(qz) + B_2 \cos(qz)\right] \exp\left[i(kx - \omega t)\right] \tag{2.6}$$

where A_1, A_2, B_1, and B_2 are the unknown constants,

$$p^2 = \frac{\omega^2}{c_L^2} - k^2 \quad , \tag{2.7}$$

$$q^2 = \frac{\omega^2}{c_S^2} - k^2 \quad , \tag{2.8}$$

$$c_L{}^2 = \sqrt{\frac{\lambda + 2\mu}{\rho}} \quad , \tag{2.9}$$

$$c_S{}^2 = \sqrt{\frac{\mu}{\rho}} \quad , \tag{2.10}$$

and λ and μ are the Lamé's constants. By substituting (2.5)-(2.6) into (2.2)-(2.4) and ignoring the harmonic factor $\exp\left[i\left(kx - \omega t\right)\right]$, we obtain the displacement and stress components in terms of the unknown constants

$$u = ik\left[A_1 \sin(pz) + A_2 \cos(pz)\right] + q\left[B_1 \cos(qz) - B_2 \sin(qz)\right] \quad , \tag{2.11}$$

$$w = p\left[A_1 \cos\left(pz\right) - A_2 \sin\left(pz\right)\right] - ik\left[B_1 \sin\left(qz\right) + B_2 \cos\left(qz\right)\right] \quad , \tag{2.12}$$

$$\begin{aligned} T_{zx} = {} & 2i\mu kp\left[A_1 \cos\left(pz\right) - A_2 \sin\left(pz\right)\right] + \\ & \left(k^2 - q^2\right)\left[B_1 \sin\left(qz\right) + B_2 \cos\left(pz\right)\right] \quad , \end{aligned} \tag{2.13}$$

$$\begin{aligned} T_{zz} = {} & -\lambda\left(k^2 + p^2\right)\left[A_1 \sin\left(pz\right) + A_2 \cos\left(pz\right)\right] - \\ & 2\mu p^2\left[A_1 \sin\left(pz\right) + A_2 \cos\left(pz\right)\right] - \\ & 2i\mu kq\left[B_1 \cos\left(qz\right) + B_2 \sin\left(qz\right)\right] \quad . \end{aligned} \tag{2.14}$$

Following Graff (1975), Rose (1999) and Kundu (2003), we split the solutions into symmetric and antisymmetric modes. For symmetric mode, the wave motion is symmetric with respect to the midplane of the plate [Figure 2.2(a)] and for antisymmetric mode; the motion is antisymmetric with respect to the midplane of the plate [Figure 2.2 (b)].

2.1.1 Symmetric modes

For symmetric modes,

$$\phi = A_2 \cos(pz) \quad , \tag{2.15}$$

$$\psi = B_1 \sin(qz) \quad , \tag{2.16}$$

and thus

$$u = ikA_2 \cos(pz) + qB_1 \cos(qz) \quad , \tag{2.17}$$

$$w = -pA_2 \sin(pz) - ikB_1 \sin(qz) \quad , \tag{2.18}$$

$$T_{zx} = \mu\left[-2ikpA_2 \sin(pz) + (k^2 - q^2)B_1 \sin(qz)\right] \quad , \tag{2.19}$$

and

$$\begin{aligned} T_{zz} &= -\lambda(k^2 + q^2)A_2 \cos(pz) - 2\mu\left[p^2 A_2 \cos(pz) + ikqB_1 \cos(qz)\right] \\ &= -\left(\lambda k^2 + \lambda p^2 + 2\mu p^2\right)A_2 \cos(pz) - 2i\mu kqB_1 \cos(qz) \quad . \end{aligned} \tag{2.20}$$

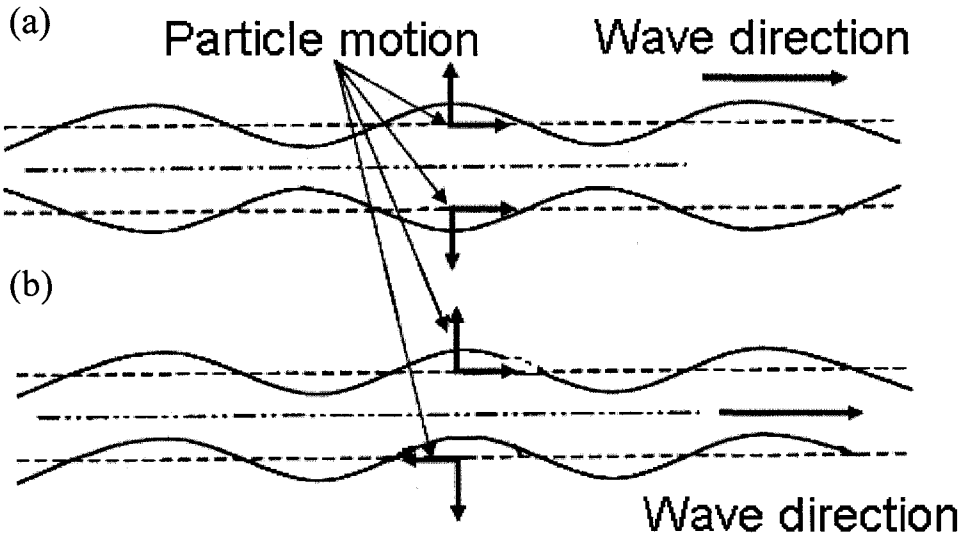

Figure 2.2 Schematics of the deformation of the plate and particle movement directions of (a) symmetric and (b) antisymmetric modes of wave propagation.

The two unknown constants A_2 and B_1 can be found by applying the stress-free conditions at the boundary $z = d$

$$T_{zx} = -2i\mu kpA_2 \sin(pd) + \mu(k^2 - q^2)B_1 \sin(qd) = 0 \tag{2.21}$$

and

$$T_{zz} = -\left(\lambda k^2 + \lambda p^2 + 2\mu p^2\right) A_2 \cos(pd) - 2i\mu kqB_1 \cos(qd) = 0 \quad . \tag{2.22}$$

Equation (2.21) and (2.22) can also be written in matrix form

$$\begin{bmatrix} -2i\mu kp\sin(pd) & \mu(k^2 - q^2)\sin(qd) \\ -\left(\lambda k^2 + \lambda p^2 + 2\mu p^2\right)\cos(pd) & -2i\mu kq\cos(qd) \end{bmatrix} \begin{bmatrix} A_2 \\ B_1 \end{bmatrix} = 0 \quad . \tag{2.23}$$

To find the nonzero solutions of A_2 and B_1, we require the determinant of the coefficient matrix to be vanished. So

$$\det \begin{bmatrix} -2i\mu kp\sin(pd) & \mu(k^2 - q^2)\sin(qd) \\ -\left(\lambda k^2 + \lambda p^2 + 2\mu p^2\right)\cos(pd) & -2i\mu kq\cos(qd) \end{bmatrix} = 0 \quad , \tag{2.24}$$

$$\begin{aligned} 4\mu k^2 pq \sin(pd)\cos(qd) = \\ \left(k^2 - q^2\right)\left(\lambda k^2 + \lambda p^2 + 2\mu p^2\right)\sin(qd)\cos(pd) \quad , \end{aligned} \tag{2.25}$$

$$\frac{\sin(qd)\cos(pd)}{\sin(pd)\cos(qd)} = \frac{4\mu k^2 pq}{\left(\lambda k^2 + \lambda p^2 + 2\mu p^2\right)\left(k^2 - q^2\right)} \quad , \tag{2.26}$$

or

$$\frac{\tan(qd)}{\tan(pd)} = \frac{4k^2 qp\mu}{(\lambda k^2 + \lambda p^2 + 2\mu p^2)(k^2 - q^2)} \quad . \tag{2.27}$$

Equation (2.26) can also be found by using the boundary condition $z = -d$ in (2.21) and (2.22). The denominator on the right-hand-side of (2.27) can be further simplified as

$$\begin{aligned}\lambda k^2+\lambda p^2+2\mu p^2 &= \lambda(k^2+p^2)+2\mu p^2 = (\rho c_L^2-2\mu)(k^2+p^2)+2\mu p^2 \\ &= \rho c_L^2\left(k^2+p^2\right)-2\mu k^2 = \rho\omega^2-2\rho c_s^2 k^2 \\ &= \rho c_s^2\left(\frac{\omega^2}{c_s^2}-2k^2\right)=\rho c_s^2\left(q^2-k^2\right) \\ &= \mu\left(q^2-k^2\right) \quad .\end{aligned} \tag{2.28}$$

Substituting (2.28) into (2.27), we obtain

$$\frac{\tan(qd)}{\tan(pd)} = -\frac{4k^2pq}{(q^2-k^2)^2} \quad . \tag{2.29}$$

Equation (2.29) is known as Rayleigh-Lamb dispersion equation for the symmetric modes. The dispersion equation provides the phase velocity information of each frequency component. It is common to plot the phase velocities versus the product of frequency and thickness ($f\times d$). Due to the periodicity π of the tangent function, higher symmetric wave modes are possible and are denoted by $S0$, $S1$, $S2$,..., where S implies the symmetric modes.

2.1.2 Antisymmetric modes

Similarly for antisymmetric modes,

$$\phi = A_1\sin(pz) \quad , \tag{2.30}$$

$$\psi = B_2\cos(qz) \quad , \tag{2.31}$$

and thus

$$u = ikA_1\sin(pz)-qB_2\sin(qz) \quad , \tag{2.32}$$

$$w = pA_1\cos(pz)-ikB_2\cos(qz) \quad , \tag{2.33}$$

$$T_{zx} = \mu\left[2ikpA_1\cos(pz)+(k^2-q^2)B_2\cos(qz)\right] \quad , \tag{2.34}$$

$$T_{zz} = -\lambda(k^2+q^2)A_1\sin(pz)-2\mu\left[p^2A_1\sin(pz)-ikqB_2\sin(qz)\right] \quad . \tag{2.35}$$

The two unknowns A_1 and B_2 can be solved by the boundary conditions at $z = d$:

$$\sigma_{zx} = 2i\mu kpA_1 \cos(pd) + \mu(k^2 - q^2)B_2 \cos(qd) = 0 \quad , \tag{2.36}$$

and

$$\sigma_{zz} = -\left(\lambda k^2 + \lambda p^2 + 2\mu p^2\right) A_1 \sin\left(pd\right) + 2i\mu kqB_2 \cos\left(qd\right) = 0 \quad . \tag{2.37}$$

Following the same procedure for symmetric modes, we obtain

$$\frac{\tan(qd)}{\tan(pd)} = -\frac{(q^2 - k^2)^2}{4k^2 pq} \tag{2.38}$$

which is the Rayleigh-Lamb dispersion equation for antisymmetric mode. Higher order modes of antisymmetric modes are denotes by $A0$, $A1$, $A2$,..., where A implies the symmetric modes.

2.2 Guided wave propagation in fluid-filled cylinders

Guided wave propagating in a cylinder is a complex phenomenon. There are three possible guided wave modes traveling along the axis of the cylinders: longitudinal, torsional and flexural modes (Rose, 1999). The longitudinal and torsional modes are axisymmetric modes, but the flexural modes are antisymmetric modes. Guided wave propagation in hollow cylinders such as shells and pipes has been studied by many investigators (Copper and Naghdi, 1957; Gazis, 1959; Graff, 1975; Rose, 1999; Kundu, 2003). Guided wave propagation in fluid-filled cylinder was also fruitfully investigated (Kumar, 1971; Lowe, 1995; Elvira-Segura, 2000) especially in borehole geophysics (Peterson, 1973; Randall and Stanke, 1988; Sinha, *et al*, 1992).

A cylindrical tube model with inner and outer radii, a and b, respectively was considered in this study (Figure 2.3). The wall thickness is h (h=b-a). The tube

material has density ρ_c, longitudinal wave velocity $c_{L,c}$ and shear wave velocity $c_{S,c}$, where the subscript "*c*" denotes cylinder. The tube is filled with fluid with density ρ_f, longitudinal wave velocity $c_{L,f}$ where the subscript "*f*" denotes fluid. The wave speeds are related to the elastic constants by

$$c_{L,c} = \sqrt{\frac{\lambda_c + 2\mu_c}{\rho}} \quad , \quad c_{S,c} = \sqrt{\frac{\mu_c}{\rho}} \quad , \text{ and } \quad c_{L,f} = \sqrt{\frac{\lambda_f}{\rho}} \tag{2.39}$$

where λ_c and μ_c are the Lamé's constants of the solid and λ_f is the bulk modulus of the fluid.

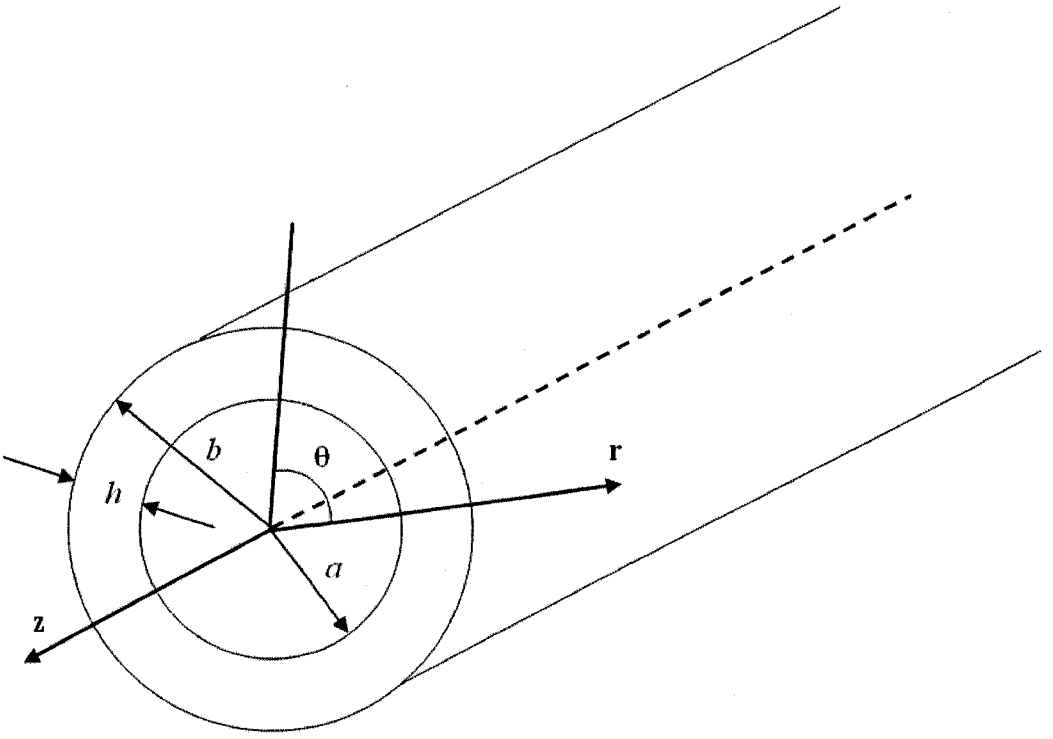

Figure 2.3 Geometry of a fluid-filled cylindrical tube.

The equation of motion for an isotropic elastic equation is (A.19)

$$\rho\frac{\partial^2\vec{u}}{\partial t^2}=(\lambda+\mu)\nabla\left(\nabla\cdot\vec{u}\right)+\mu\nabla^2\vec{u} \tag{2.40}$$

where the displacement field $\vec{u}$ is given by (A.20) and (A.21)

$$\vec{u}=\nabla\phi+\nabla\times\vec{H} \quad . \tag{2.41}$$

The scalar potential ϕ and the vector potential $\vec{H}$ satisfy the wave equation (A.25) and (A.28), respectively

$$\nabla^2\phi=\frac{1}{c_L^2}\frac{\partial^2\phi}{\partial t^2} \tag{2.42}$$

and

$$\nabla^2\vec{H}=\frac{1}{c_S^2}\frac{\partial^2\vec{H}}{\partial t^2} \quad . \tag{2.43}$$

Let ϕ and $\vec{H}=\left(H_r,H_\theta,H_z\right)$ take the following forms in the cylindrical coordinates (Gazis, 1959; Pavlakovic and Lowe, 2001)

$$\phi=f(r)\cos n\theta\cos\left(\omega t+kz\right) \quad , \tag{2.44}$$

$$H_r=h_r(r)\sin n\theta\sin\left(\omega t+kz\right) \quad , \tag{2.45}$$

$$H_\theta=h_\theta(r)\cos n\theta\sin\left(\omega t+kz\right) \quad , \tag{2.46}$$

and

$$H_z=h_z(r)\sin n\theta\cos\left(\omega t+kz\right) \quad . \tag{2.47}$$

Substituting (2.44)-(2.47) in (2.42) and (2.43), expressing the Laplacian in cylindrical coordinates (see Appendix B) and simplifying yield

$$\frac{\partial^2 f}{\partial r^2}+\frac{1}{r}\frac{\partial f}{\partial r}-\left[\frac{n^2}{r^2}-\left(\frac{\omega^2}{c_L^2}-k^2\right)\right]f=0 \quad , \tag{2.48}$$

$$\frac{\partial^2 h_r}{\partial r^2}+\frac{1}{r}\frac{\partial h_r}{\partial r}+\frac{1}{r^2}\left(-n^2 h_r+2nh_\theta-h_r\right)-k^2 h_r+\frac{\omega^2}{c_S^2}h_r=0 \quad , \tag{2.49}$$

$$\frac{\partial^2 h_\theta}{\partial r^2}+\frac{1}{r}\frac{\partial h_\theta}{\partial r}+\frac{1}{r^2}\left(-n^2 h_\theta+2nh_r-h_\theta\right)-k^2 h_\theta+\frac{\omega^2}{c_S^2}h_\theta=0 \quad , \tag{2.50}$$

and

$$\frac{\partial^2 h_z}{\partial r^2}+\frac{1}{r}\frac{\partial h_z}{\partial r}-\left[\frac{n^2}{r^2}-\left(\frac{\omega^2}{c_S^2}-k^2\right)\right]h_z=0 \quad . \tag{2.51}$$

We define

$$h_1=\frac{1}{2}\left(h_r-h_\theta\right) \tag{2.52}$$

and

$$h_2=\frac{1}{2}\left(h_r+h_\theta\right) \quad . \tag{2.53}$$

The second-order partial differential equations governing h_1 and h_2 can be found by subtracting (2.49) from (2.50) and adding (2.49) and (2.50)

$$\frac{\partial^2 h_1}{\partial r^2}+\frac{1}{r}\frac{\partial h_1}{\partial r}-\left(\frac{(n+1)^2}{r^2}-q^2\right)h_1=0 \quad , \tag{2.54}$$

and

$$\frac{\partial^2 h_2}{\partial r^2}+\frac{1}{r}\frac{\partial h_2}{\partial r}-\left(\frac{(n-1)^2}{r^2}-q^2\right)h_2=0 \tag{2.55}$$

Equations (2.48), (2.51), (2.54), and (2.55) are the Bessel's equations (Appendix C)

$$B_{n,pr}\left(f\right)=0 \quad , \tag{2.56}$$

$$B_{n,qr}\left(h_z\right)=0 \quad , \tag{2.57}$$

$$B_{n+1,qr}\left(h_1\right)=0 \quad , \tag{2.58}$$

and

$$B_{n-1,qr}(h_2) = 0 \tag{2.59}$$

where

$$p^2 = \frac{\omega^2}{c_L^2} - k^2 \quad \text{and} \quad q^2 = \frac{\omega^2}{c_S^2} - k^2 \quad . \tag{2.60}$$

The general solutions to equations (2.56) through (2.59) are (Appendix C)

$$f = A_1 Z_n(\hat{p}r) + B_1 W_n(\hat{p}r) \quad , \tag{2.61}$$

$$h_z = A_2 Z_n(\hat{q}r) + B_2 W_n(\hat{q}r) \quad , \tag{2.62}$$

$$h_1 = A_3 Z_{n+1}(\hat{q}r) + B_3 W_{n+1}(\hat{q}r) \quad , \tag{2.63}$$

and

$$h_2 = \hat{A} Z_{n+1}(\hat{q}r) + \hat{B} W_{n+1}(\hat{q}r) \tag{2.64}$$

where

$$\hat{p} = |p| \, , \quad \hat{q} = |q| \quad , \tag{2.65}$$

and A_1, B_1, A_2, B_2, A_3, B_3, $\hat{A}$, and $\hat{B}$ are the unknown coefficients. Depending on whether p or q is real or imaginary, the functions Z_n and W_n will be the Bessel or modified Bessel functions of the first and second kind. Table 2.1 provides the classification. The coefficients have physical meaning. The coefficients A_1, A_2, and A_3 represent the downgoing *P*, *SV* and *SH* waves while the coefficients B_1, B_2, and B_3 represent the upgoing *P*, *SV* and *SH* waves.

The gauge invariance principle implies that the displacement field corresponding to an equivoluminal potential field can be derived by a combination of the other two equivoluminal potentials (Gazis, 1959; Lowe, 2001). Thus we set $h_2 = 0$ and obtain

$$h_r = -h_\theta = h_1 \quad . \tag{2.66}$$

Therefore, only three radially dependent variables, f, h_1 and h_z are required to describe the scalar potential ϕ and the vector potential $\vec{H}$ in Equations (2.44)-(2.47).

Equations (2.61)-(2.63) describe the general solutions of solids in cylindrical coordinates. For the fluid tube, since the fluid does not support shear motion, only acoustic or longitudinal wave is possible and the solution takes the following form

$$f_f = A_4 Z_n\left(\hat{p}_f r\right) + B_4 W_n\left(\hat{p}_f r\right) \tag{2.67}$$

where $p_f^2 = \frac{\omega^2}{c_{L,f}^2} - k^2$ and $\hat{p}_f = \left|p_f\right|$. When the inner radius of the cylinder is very small, the second term will go to infinity (Kumar, 1972; Sinha, *et al*, 1992).

$$\lim_{r\to 0} W_n\left(\hat{p}_f r\right) \to -\infty \quad . \tag{2.68}$$

Table 2.1 Choice of the functions Z_n and W_n (Gazis, 1959; Rose, 1999; Pavlakovic and Lowe, 2001). Equation (2.60) defines p^2 and q^2.

when $p^2, q^2 > 0$	when $p^2 < 0, q^2 > 0$	when $p^2, q^2 < 0$
$\gamma_1 = 1$	$\gamma_1 = -1$	$\gamma_1 = -1$
$\gamma_2 = 1$	$\gamma_2 = 1$	$\gamma_2 = -1$
$Z_n(\hat{p}r) = J_n(\hat{p}r)$	$Z_n(\hat{p}r) = I_n(\hat{p}r)$	$Z_n(\hat{p}r) = I_n(\hat{p}r)$
$W_n(\hat{p}r) = Y_n(\hat{p}r)$	$W_n(\hat{p}r) = K_n(\hat{p}r)$	$W_n(\hat{p}r) = K_n(\hat{p}r)$
$Z_n(\hat{q}r) = J_n(\hat{q}r)$	$Z_n(\hat{q}r) = J_n(\hat{q}r)$	$Z_n(\hat{q}r) = I_n(\hat{q}r)$
$W_n(\hat{q}r) = Y_n(\hat{q}r)$	$W_n(\hat{q}r) = Y_n(\hat{q}r)$	$W_n(\hat{q}r) = K_n(\hat{q}r)$

This is physically not permissible because the solution should be bounded. Thus we set $B_4 = 0$ (Kumar, 1972; Sinha, *et al*, 1992). This implies that only downgoing

longitudinal wave exist and the upgoing longitudinal wave is ignored. This is a valid assumption because the reflections from the deeper portion of the tube are very weak and can be ignored.

Now we have seven unknown constants A_1, B_1, A_2, B_2, A_3, B_3, and A_4. To determine the seven unknowns implicit in (2.61)-(2.63) and (2.68), seven boundary conditions are required. The required boundary conditions involve three stress components T_{rr}, $T_{r\theta}$, T_{rz} and the normal displacement component u_{rr} (Gazis, 1959; Sinha *et al*, 1992; Rose, 1999):

$$T_{rr}|_{r=b} = 0 \quad , \tag{2.69}$$

$$T_{r\theta}|_{r=b} = 0 \quad , \tag{2.70}$$

$$T_{rz}|_{r=b} = 0 \quad . \tag{2.71}$$

$$T_{rr}|_{r=a+} = T_{rr}|_{r=a-} \quad , \tag{2.72}$$

$$T_{r\theta}|_{r=a} = 0 \quad , \tag{2.73}$$

$$T_{rz}|_{r=a} = 0 \quad , \tag{2.74}$$

and

$$u_{rr}|_{r=a+} = u_{rr}|_{r=a-} \quad . \tag{2.75}$$

The first three boundary conditions (2.69)-(2.71) describe the stress-free conditions at the outer surface. Equation (2.72) requires that the normal stresses are continuous at the solid and liquid interface. The '+' indicates that interface is approached from the solid side and the '-' indicates that the interface is approached from fluid side. Equations (2.73) and (2.74) state that the shear stress vanishes in the fluid. The last boundary condition (2.75) describes the normal displacements are continuous at the inner surface.

By expressing the displacement $\vec{u}$ defined by equation (2.41) in cylindrical coordinates as $\vec{u} = (u_r, u_\theta, u_z)$ (Achenbach, 1975, pp.73-74):

$$u_r = \frac{\partial \phi}{\partial r} + \frac{1}{r}\frac{\partial H_z}{\partial \theta} - \frac{\partial H_\theta}{\partial z} \quad , \tag{2.76}$$

$$u_\theta = \frac{1}{r}\frac{\partial \phi}{\partial \theta} + \frac{\partial H_r}{\partial z} - \frac{\partial H_z}{\partial r} \quad , \tag{2.77}$$

$$u_z = \frac{\partial \phi}{\partial z} + \frac{1}{r}\frac{\partial (H_\theta r)}{\partial r} - \frac{1}{r}\frac{\partial H_r}{\partial \theta} \quad , \tag{2.78}$$

and replacing the potentials by equations (2.44)-(2.47), the stress components of solid take the following form (Appendix B.2)

$$\begin{aligned} T_{rr} &= \lambda_c \left(\frac{\partial u_r}{\partial r} + \frac{1}{r}\frac{\partial u_\theta}{\partial \theta} + \frac{u_r}{r} + \frac{\partial u_z}{\partial z} \right) + 2\mu_c \frac{\partial u_r}{\partial r} \\ &= \lambda_c \left(\frac{\partial^2 \phi}{\partial r^2} + \frac{1}{r^2}\frac{\partial^2 \phi}{\partial \theta^2} + \frac{1}{r}\frac{\partial \phi}{\partial r} + \frac{\partial^2 \phi}{\partial z^2} \right) + 2\mu_c \left(\frac{\partial^2 \phi}{\partial r^2} + \frac{1}{r^2}\frac{\partial^2 H_z}{\partial r \partial \theta} - \frac{1}{r^2}\frac{\partial H_z}{\partial \theta} - \frac{\partial^2 H_\theta}{\partial r \partial z} \right) \\ &= \lambda_c \nabla^2 \phi + 2\mu_c \left(\frac{\partial^2 \phi}{\partial r^2} + \frac{1}{r^2}\frac{\partial^2 H_z}{\partial r \partial \theta} - \frac{1}{r^2}\frac{\partial H_z}{\partial \theta} - \frac{\partial^2 H_\theta}{\partial r \partial z} \right) \\ &= \left\{ -\lambda_c \left(p_c^2 + k^2 \right) f_c + 2\mu_c \left[f_c'' + \frac{n}{r}\left(h_z' - \frac{1}{r} h_z \right) + k h_1' \right] \right\} \cos n\theta \cos(\omega t + kz) \quad , \end{aligned} \tag{2.79}$$

$$\begin{aligned} T_{r\theta} &= \mu_c \left(\frac{\partial u_\theta}{\partial r} - \frac{u_\theta}{r} + \frac{1}{r}\frac{\partial u_r}{\partial \theta} \right) \\ &= \mu_c \left(\frac{2}{r}\frac{\partial^2 \phi}{\partial r \partial \theta} - \frac{2}{r^2}\frac{\partial \phi}{\partial \theta} + \frac{\partial^2 H_r}{\partial r \partial z} - \frac{1}{r}\frac{\partial H_z}{\partial z} - \frac{\partial^2 H_z}{\partial r^2} + \frac{1}{r}\frac{\partial H_z}{\partial r} + \frac{1}{r^2}\frac{\partial^2 H_z}{\partial \theta^2} - \frac{1}{r}\frac{\partial^2 H_\theta}{\partial \theta \partial z} \right) \\ &= -\mu_c \left(-\frac{2n}{r^2} f_c + \frac{2n}{r} f_c' + 2h_z'' + q^2 h_z + \frac{(n+1)k}{r} h_1 - k h_1' \right) \sin n\theta \cos(\omega t + kz) \quad , \end{aligned} \tag{2.80}$$

and

$$
\begin{aligned}
T_{rz} &= \mu_c\left(\frac{\partial u_r}{\partial z}+\frac{\partial u_z}{\partial r}\right) \\
&= \mu_c\left(\frac{\partial^2\phi}{\partial r\partial z}+\frac{1}{r}\frac{\partial^2 H_z}{\partial z\partial\theta}-\frac{\partial^2 H_\theta}{\partial z^2}+\frac{\partial^2\phi}{\partial r\partial z}+\frac{1}{r}\frac{\partial H_\theta}{\partial r}-\frac{H_\theta}{r^2}+\frac{\partial^2 H_\theta}{\partial r^2}-\frac{1}{r}\frac{\partial^2 H_r}{\partial r\partial\theta}+\frac{1}{r^2}\frac{\partial H_r}{\partial\theta}\right) \\
&= -\mu_c\left\{2kf_c'+\frac{n}{r}kh_z+\left(\frac{n(n+1)}{r^2}+k^2-q^2\right)h_1+\frac{n}{r}h_1'\right\}\cos n\theta\sin(\omega t+kz)
\end{aligned}
\tag{2.81}
$$

where the prime and double primes denote first and second derivatives with respect to the radial variable r. In order to derive equation (2.80), we use the following equality

$$
\lambda_c\nabla^2\phi=\frac{\lambda_c}{c_{L,c}^2}\frac{\partial^2\phi}{\partial t^2}=-\lambda_c\frac{\omega^2}{c_{L,c}^2}\phi=-\lambda_c\left(p_c^2+k^2\right)\phi \tag{2.82}
$$

where equations (2.42), (2.44) and (2.60) are consulted. In equations (2.79) and (2.80), the Bessel's equations

$$
\frac{\partial^2 h_1}{\partial r^2}+\frac{1}{r}\frac{\partial h_1}{\partial r}-\left(\frac{(n+1)^2}{r^2}-q^2\right)h_1=0 \tag{2.83}
$$

and

$$
\frac{\partial^2 h_z}{\partial r^2}+\frac{1}{r}\frac{\partial h_z}{\partial r}-\left(\frac{n^2}{r^2}-q^2\right)h_z=0 \tag{2.84}
$$

are used. The stress component of fluid is similar to (2.79) without the shear term

$$
T_{rr}^f=\left[-\lambda_f\left(p_f^2+k^2\right)f_f\right]\cos n\theta\cos(\omega t+kz)\quad . \tag{2.85}
$$

The displacement components u_{rr} of solid and fluid are, respectively,

$$
u_{rr}^c=\frac{\partial\phi}{\partial r}+\frac{1}{r}\frac{\partial H_z}{\partial\theta}-\frac{\partial H_\theta}{\partial z}=\left(f_c'+\frac{n}{r}h_z+kh_1\right)\cos n\theta\cos(\omega t+kz)\quad , \tag{2.86}
$$

and

$$u_{rr}^{f} = \frac{\partial \phi}{\partial r} = f_f' \cos n\theta \cos(\omega t + kz) \quad . \tag{2.87}$$

Using the stress components given by (2.79) – (2.81) and (2.85), the displacement components, (2.86) and (2.87), and ignoring the harmonic term, the seven boundary conditions (2.69) – (2.75) can be posed in the following forms:

$$\lambda_c \left(p_c^2 + k^2\right) f_c - 2\mu_c \left[f'' + \frac{n}{r} h_z' - \frac{n}{r^2} h_z + k h_1' \right]\Bigg|_{r=b} = 0 \quad , \tag{2.88}$$

$$\mu_c \left[-\frac{2n}{r^2} f_c + \frac{2n}{r} f_c' + 2h_z'' + q_c^2 h_z - k h_1' + \frac{(n+1)k}{r} h_1 \right]\Bigg|_{r=b} = 0 \quad , \tag{2.89}$$

$$\mu_c \left[2k f_c' + \frac{nk}{r} h_z + k^2 h_1 + \frac{n}{r} h_1' + \left(\frac{n(n+1)}{r^2} - q_c^2 \right) h_1 \right]\Bigg|_{r=b} = 0 \quad , \tag{2.90}$$

$$\lambda_c \left(p_c^2 + k^2\right) f_c - 2\mu_c \left[f_c'' + \frac{n}{r} h_z' - \frac{n}{r^2} h_z + k h_1' \right]\Bigg|_{r=a^+} = \lambda_f \left(p_f^2 + k^2\right) f_f \Big|_{r=a^-} \quad , \tag{2.91}$$

$$\mu_c \left[-\frac{2n}{r^2} f_c + \frac{2n}{r} f_c' + 2h_z'' + q_c^2 h_z - k h_1' + \frac{(n+1)k}{r} h_1 \right]\Bigg|_{r=a} = 0 \quad , \tag{2.92}$$

$$\mu_c \left[2k f_c' + \frac{nk}{r} h_z + k^2 h_1 + \frac{n}{r} h_1' + \left(\frac{n(n+1)}{r^2} - q_c^2 \right) h_1 \right]\Bigg|_{r=a} = 0 \quad , \tag{2.93}$$

and

$$f_c' + \frac{n}{r} h_z + k h_1 \Big|_{r=a^+} = f_f' \Big|_{r=a^-} . \tag{2.94}$$

Expressing f, h_1, h_z, and f_f in terms of the Bessel functions defined by (2.61) - (2.63) and (2.67) gives

$$\lambda_c\left(p_c^2+k^2\right)\left[A_1Z_n\left(\hat{p}_cr\right)+B_1W_n\left(\hat{p}_cr\right)\right]-$$
$$2\mu_c\left\{\left[A_1Z_n''\left(\hat{p}_cr\right)+B_1W_n''\left(\hat{p}_cr\right)\right]+\frac{n}{r}\left[A_2Z_n'\left(\hat{q}_cr\right)+B_2W_n'\left(\hat{q}_cr\right)\right]-\right. \tag{2.95}$$
$$\left.\frac{n}{r^2}\left[A_2Z_n\left(\hat{q}_cr\right)+B_2W_n\left(\hat{q}_cr\right)\right]+k\left[A_3Z_{n+1}'\left(\hat{q}_cr\right)+B_3W_{n+1}'\left(\hat{q}_cr\right)\right]\right\}\Big|_{r=b}=0 \quad ,$$

$$\mu_c\left\{-\frac{2n}{r^2}\left[A_1Z_n\left(\hat{p}_cr\right)+B_1W_n\left(\hat{p}_cr\right)\right]+\frac{2n}{r}\left[A_1Z_n'\left(\hat{p}_cr\right)+B_1W_n'\left(\hat{p}_cr\right)\right]+\right.$$
$$2\left[A_2Z_n''\left(\hat{q}_cr\right)+B_2W_n''\left(\hat{q}_cr\right)\right]+q_c^2\left[A_2Z_n\left(\hat{q}_cr\right)+B_2W_n\left(\hat{q}_cr\right)\right]-$$
$$k\left[A_3Z_{n+1}'\left(\hat{q}_cr\right)+B_3W_{n+1}'\left(\hat{q}_cr\right)\right]+ \tag{2.96}$$
$$\left.\frac{(n+1)k}{r}\left[A_3Z_{n+1}\left(\hat{q}_cr\right)+B_3W_{n+1}\left(\hat{q}_cr\right)\right]\right\}\Big|_{r=b}=0 \quad ,$$

$$\mu_c\left\{2k\left[A_1Z_n'\left(\hat{p}_cr\right)+B_1W_n'\left(\hat{p}_cr\right)\right]+\frac{nk}{r}\left[A_2Z_n\left(\hat{q}_cr\right)+B_2W_n\left(\hat{q}_cr\right)\right]+\right.$$
$$\frac{n}{r}\left[A_3Z_{n+1}'\left(\hat{q}_cr\right)+B_3W_n'\left(\hat{q}_cr\right)\right]+ \tag{2.97}$$
$$\left.\left[\frac{n(n+1)}{r^2}+k^2-q_c^2\right]\left[A_3Z_{n+1}\left(\hat{q}_cr\right)+B_3W_n\left(\hat{q}_cr\right)\right]\right\}\Big|_{r=b}=0 \quad .$$

$$\lambda_f\left(p_f^2+k^2\right)A_4Z_n\left(\hat{p}_fr\right)-\lambda_c\left(p_c^2+k^2\right)\left[A_1Z_n\left(\hat{p}_cr\right)+B_1W_n\left(\hat{p}_cr\right)\right]+$$
$$2\mu_c\left\{A_1Z_n''\left(\hat{p}_cr\right)+B_1W_n''\left(\hat{p}_cr\right)+\frac{n}{r}\left[A_2Z_n'\left(\hat{q}_cr\right)+B_2W_n'\left(\hat{q}_cr\right)\right]-\right.$$
$$\left.\frac{n}{r^2}\left[A_2Z_n\left(\hat{q}_cr\right)+B_2W_n\left(\hat{q}_cr\right)\right]+k\left[A_3Z_{n+1}'\left(\hat{q}_cr\right)+B_3W_{n+1}'\left(\hat{q}_cr\right)\right]\right\}\Big|_{r=a}=0 \quad , \tag{2.98}$$

$$\mu_c\left\{-\frac{2n}{r^2}\left[A_1 Z_n(\hat{p}_c r)+B_1 W_n(\hat{p}_c r)\right]+\frac{2n}{r}\left[A_1 Z_n'(\hat{p}_c r)+B_1 W_n'(\hat{p}_c r)\right]+\right.$$
$$2\left[A_2 Z_n''(\hat{q}_c r)+B_2 W_n''(\hat{q}_c r)\right]+q_c^2\left[A_2 Z_n(\hat{q}_c r)+B_2 W_n(\hat{q}_c r)\right]-$$
$$\left.k\left[A_3 Z_{n+1}'(\hat{q}_c r)+B_3 W_{n+1}'(\hat{q}_c r)\right]+\frac{(n+1)k}{r}\left[A_3 Z_{n+1}(\hat{q}_c r)+B_3 W_{n+1}(\hat{q}_c r)\right]\right\}\Bigg|_{r=a}=0 \quad , \tag{2.99}$$

$$\mu_c\left\{2k\left[A_1 Z_n'(\hat{p}_c r)+B_1 W_n'(\hat{p}_c r)\right]+\frac{nk}{r}\left[A_2 Z_n(\hat{q}_c r)+B_2 W_n(\hat{q}_c r)\right]+\right.$$
$$\frac{n}{r}\left[A_3 Z_{n+1}'(\hat{q}_c r)+B_3 W_n'(\hat{q}_c r)\right]+ \tag{2.100}$$
$$\left.\left[\frac{n(n+1)}{r^2}+k^2-q_c^2\right]\left[A_3 Z_{n+1}(\hat{q}_c r)+B_3 W_n(\hat{q}_c r)\right]\right\}\Bigg|_{r=a}=0 \quad ,$$

and

$$A_1 Z_n'(\hat{p}_c r)+B_1 W_n'(\hat{p}_c r)+\frac{n}{r}A_2 Z_n(\hat{p}_c r)+\frac{n}{r}B_2 W_n(\hat{p}_c r)+$$
$$kA_3 Z_n(\hat{p}_c r)+kB_3 W_n(\hat{p}_c r)\Big|_{r=a}=A_4 Z_n'(\hat{p}_f r)\Big|_{r=a^-} \quad . \tag{2.101}$$

The set of seven equations defined by (2.95) - (2.101) can be cast in a matrix form

$$\begin{pmatrix} D_{11} & D_{12} & D_{13} & D_{14} & D_{15} & D_{16} & D_{17} \\ D_{21} & D_{22} & D_{23} & D_{24} & D_{25} & D_{26} & D_{27} \\ D_{31} & D_{32} & D_{33} & D_{34} & D_{35} & D_{36} & D_{37} \\ D_{41} & D_{42} & D_{43} & D_{44} & D_{45} & D_{46} & D_{47} \\ D_{51} & D_{52} & D_{53} & D_{54} & D_{55} & D_{56} & D_{57} \\ D_{61} & D_{62} & D_{63} & D_{64} & D_{65} & D_{66} & D_{67} \\ D_{71} & D_{72} & D_{73} & D_{74} & D_{75} & D_{76} & D_{77} \end{pmatrix} \cdot \begin{pmatrix} A_1 \\ B_1 \\ A_2 \\ B_2 \\ A_3 \\ B_3 \\ A_4 \end{pmatrix} = 0 \tag{2.102}$$

where the element D_{ij} are defined by Equations (D.1) – (D.49) in Appendix D. In order to obtain nonzero solutions for the unknowns $\left[A_1, B_1, A_2, B_2, A_3, B_3, A_4\right]^T$, we require the determinant of coefficient matrix to be zero, which is

$$\left|D_{ij}\right| = 0, \left(i, j = 1 \cdots 7\right) \quad . \tag{2.103}$$

Equation (2.103) dictates the dispersion curves for three guided wave modes:

longitudinal modes: $L\ (0, m)$, m=1, 2, 3, ...;

torsional modes: $T\ (0, m)$; m=1, 2, 3, ...;

and

flexural modes: $F\ (n, m)$, n = 1, 2, 3, ... and m = 1, 2, 3, ...

The first two modes are axisymmetric and the other is non-axisymmetric. The particle polarization of the longitudinal modes is in the (r, z) plane. The polarization of the torsional modes is confined to the θ direction. For flexural modes, the polarization vector is along all three directions. Both the experimental configuration and the transducer-wedge systems considered in this work emphasize longitudinal guided wave modes. There is no torsional wave. The flexural modes, if there is any, will be extremely weak (Zemanek, 1971; Silk and Bainton, 1979; Rose, 1999). Thus we consider n = 0 and the longitudinal modes. If n = 0, then the equation (2.103) can be decomposed as the product of subdeterminants (Appendix D.2) as

$$\begin{aligned} \mathbf{D} &= \begin{vmatrix} D_{11} & D_{12} & D_{15} & D_{16} & 0 \\ D_{31} & D_{32} & D_{35} & D_{36} & 0 \\ D_{41} & D_{42} & D_{45} & D_{46} & D_{47} \\ D_{61} & D_{62} & D_{65} & D_{66} & 0 \\ D_{71} & D_{72} & D_{75} & D_{76} & D_{77} \end{vmatrix} \begin{vmatrix} D_{23} & D_{24} \\ D_{53} & D_{54} \end{vmatrix} \\ &= \mathbf{D}_1 \mathbf{D}_2 \end{aligned} \tag{2.104}$$

where

$$\mathbf{D}_1 = \begin{vmatrix} D_{11} & D_{12} & D_{15} & D_{16} & 0 \\ D_{31} & D_{32} & D_{35} & D_{36} & 0 \\ D_{41} & D_{42} & D_{45} & D_{46} & D_{47} \\ D_{61} & D_{62} & D_{65} & D_{66} & 0 \\ D_{71} & D_{72} & D_{75} & D_{76} & D_{77} \end{vmatrix} , \tag{2.105}$$

and

$$\mathbf{D}_2 = \begin{vmatrix} D_{23} & D_{24} \\ D_{53} & D_{54} \end{vmatrix} \quad . \tag{2.106}$$

The solutions of $\mathbf{D}_1 = 0$ and $\mathbf{D}_2 = 0$ corresponding to the longitudinal and torsional modes respectively. In our work, we focus on the solutions of longitudinal modes and the coefficients can be found in Appendix D.

2.3 From elasticity to anelasticity

Ultrasound traveling through materials or bone will experience absorption and scattering. Both mechanisms will give rise to attenuation phenomenon such as diminishing amplitude and pulse boarding. In this work, material absorption was considered. To numerically simulate dispersion curves, material absorption can be introduced by making the wave speed, c, complex

$$c_{elastic} \rightarrow c_{anelastic} = \frac{\omega}{k} \quad . \tag{2.107}$$

When the wave speed is complex, either frequency or wave number is complex. In ultrasound application, the wavenumber is assumed to be complex and the frequency real (Lowe, 1995).

Consider a plane wave along the x direction

$$u = G(f)e^{i(kx-\omega t)} \tag{2.108}$$

where $G(f)$ is the source function. For absorption medium, the wavenumber is complex

$$k = k_{real} + i\alpha \tag{2.109}$$

where k_{real} is the real part of the wavenumber, α is the attenuation coefficient in Nepers per wavelength or dB per traveling distance and $i^2 = -1$. Substituting (2.109) into (2.108) yields

$$u = G(f)e^{-\alpha x}e^{i(kx-\omega t)} \tag{2.110}$$

where each frequency component, f, travels with the phase velocity, $c_{phase} = \frac{2\pi f}{k_r}$. In terms of (2.110), the wave speed can be written as

$$c_{anelastic} = \frac{\omega}{k_r + i\alpha} = \frac{\omega/k_r}{1 + i\frac{\alpha}{k_r}} = \frac{c_{ph}}{1 + i\frac{\alpha}{k_r}} \quad . \tag{2.111}$$

The constant damping loss model (Laster, *et al*, 1965; Nayfeh and Chimenti, 1981; Lowe, 1995) used in (2.109) indicates that the loss per unit distance traveled increases linearly with frequency.

2.4 Calculating the dispersion curves

Guided waves propagate in plates and cylinders in various modes. Each mode can have higher order existence. Each mode travels at a distinct phase velocity which varies with frequency. Plots of phase velocity versus frequency are known as dispersion curves. Studying of dispersion curves is fundamental to the investigation of guided waves.

Equations (2.29) and (2.38) describe the dispersion relationship for guide wave modes in plates. Equation (2.103) provides a complex set of equations to compute the dispersion curves for fluid-filled cylinders. Numerical procedures are available to find the solutions numerically. In this study, a commercial software package, DISPERSE (v.2.0.16B) was used to simulate the dispersion curves. The software was

developed by Pavlakovic and Lowe (2001) of Department of Mechanical Engineering at Imperical College and was widely used for non-destructive testing.

Given the model parameters, there are three possible signed values of the imaginary part of the wavenumbers $k = k_{real} + ik_{imag}$ (Rose, 1999, pp.111)

$$k_{imag} < 0 \quad , \tag{2.112}$$

$$k_{imag} = 0 \quad , \tag{2.113}$$

and

$$k_{imag} > 0 \quad . \tag{2.114}$$

Equation (2.112) describes an exponentially growing wave with distance, which has not been physically observed and mathematically not permissible. Therefore the only solutions are $k_{imag} \geq 0$.

Chapter 3

Spectral Estimation of Ultrasound Signals

Fourier analysis is a powerful tool to study the frequency content of continuous time signals. For time signals of finite length, efficient algorithms based on discrete finite transform (*DFT*) were developed (Naidu, 1995). Estimation of the power spectrum density (*PSD*) of a stationary time series is an important application of Fourier transform. There are two ways to compute the *PSD*. The first approach is generally known as periodogram analysis and based on the direct Fourier transformation of the time series. The second approach is to estimate the autocovariance of the time series and obtain a Fourier transformation of the estimate. Many textbooks such as Stearns and Hush (1990) and Oppenheim, *et al* (1999) provide a good description of the methods. In this chapter, a brief review of the periodogram-based method is provided. A parametric approach, commonly known as autoregressive method to estimate *PSD* by fitting data regressively is presented.

3.1 Periodogram method

Considering a N-point discrete time signal, x_n, n=0, 1, 2, ... N-1 with sampling interval Δt, the signal has been filtered by a bandpass filter to eliminate aliasing. The Fourier transform of the time signal can be written as

$$X(\omega) = \sum_{n=0}^{N-1} x(n) \mathrm{e}^{-j\omega t} \tag{3.1}$$

where $t = n\Delta t$ and the frequency, f and the angular frequency are related by $\omega = 2\pi f$. The Nyquist frequency is given by $f_{Nyquist} = \frac{1}{2\Delta t}$. The power spectrum density, $P(\omega)$ is given by (Lim, 1990, pp. 354)

$$P(\omega) = \frac{1}{N}\left|X(\omega)\right|^2 \quad . \tag{3.2}$$

For a 2-*D* discrete data set, $x(z,t)$ where the space variable is $z = m\Delta z$ and Δz is the spatial sampling interval, the 2-*D* Fourier representation of $x(z,t)$ is

$$X(\omega,k) = \sum_{n=0}^{N-1}\sum_{m=0}^{M-1} x(z,t)e^{-j(\omega t - kz)} \tag{3.3}$$

where k is the spatial frequency or wavenumber in unit cycles per meter. The wavenumber and the wavelength, λ of the signal are related by $k = \frac{2\pi}{\lambda}$ and $k_{Nyquist} = \frac{1}{2\Delta z}$. The 2-*D PSD* estimation is (Lim, 1990, pp.362)

$$P(\omega,k) = \frac{1}{N}\cdot\frac{1}{M}\left|X(\omega,k)\right|^2 \quad . \tag{3.4}$$

The resulting estimate based on (3.4) is called the periodogram. The estimate is not good because the variance does not decrease to zero as the window length increases. However by windowing and averaging, a good estimate can be obtained (Oppenheim, *et al*, 1999).

The smoothing window used is a Hamming window with the following 1-*D* representation (Oppenheim, *et al*, 1999)

$$W(n)=0.54-0.46\cos\left(2\pi\frac{n}{N}\right),\quad 0\le n\le N \tag{3.5}$$

where the window length, L is N+1. The choice of window length is very subjective. Bigger window length will provide more smoothing and thus lose resolution. Figure 3.1 shows three Hamming windows of L= 7, 11 and 15. The 2-*D* Hamming window is

$$W(n_1,n_2)=\left[0.54-0.46\cos\left(2\pi\frac{n_1}{N}\right)\right]\cdot\left[0.54-0.46\cos\left(2\pi\frac{n_2}{N}\right)\right],\quad 0\le n_1,n_2\le N. \tag{3.6}$$

An 11×11 2-*D* Hamming window is displayed in Figure 3.2 which can be obtained by revolving the 1-*D* Hamming window around the vertical axis.

In summary, to obtain an unbiased periodogram estimate, we calculate the *PSD* or periodogram and convolve the periodogram with a 2-*D* Hamming window.

3.2 Autoregressive (*AR*) estimation

Consider a linear stationary process whose output from a linear filter is the input of the past value of the process

$$x_t=\phi_1x_{t-1}+\phi_2x_{t-2}\cdots+\phi_px_{t-p}+\varepsilon_t \tag{3.7}$$

where ε_t is the random noise. The process defined by (3.7) is an autoregressive process of order p, or, more precisely, an *AR* process of order p. Consider a backward shift parameter β

$$\beta x_t=x_{t-1},\quad \beta^2x_t=x_{t-2},\quad \cdots,\quad \beta^nx_t=x_{t-n}\quad . \tag{3.8}$$

Equation (3.7) can be written as

$$x_t - \phi_1 x_{t-1} - \phi_2 x_{t-2} - \cdots - \phi_p x_{t-p} = \varepsilon_t \quad , \tag{3.9}$$

$$\left(1 - \phi_1 \beta - \phi_2 \beta^2 - \cdots - \phi_p \beta^p\right) x_t = \varepsilon_t \quad , \tag{3.10}$$

or

$$\phi(\beta) x_t = \varepsilon_t \tag{3.11}$$

where

$$\phi(\beta) = 1 - \sum_{j=1}^{p} \phi_j \beta^j \quad . \tag{3.12}$$

Thus

$$x_t = \frac{1}{\phi(\beta)} \varepsilon_t = \phi^{-1}(\beta) \varepsilon_t \quad . \tag{3.13}$$

From equation (3.13), the *AR* process can be thought of a stochastic process in which the output x_t from a linear filter with transfer function $\phi^{-1}(\beta)$ when the input is white noise ε_t.

The *PSD* of the *AR* process is (Jenkins and Watts, 1968; Priestley, 1981)

$$P(\omega) = \frac{\sigma_\varepsilon^2}{\left|1 - \sum_{j=1}^{p} \phi_j e^{-j\omega}\right|^2} \tag{3.14}$$

where the expectation value of ε_t is

$$E\left(\varepsilon_t^2\right) = \sigma_\varepsilon^2 \quad . \tag{3.15}$$

In the studies of bone mimicking phantoms and bovine bones, the number of time series acquired is restricted by the topographic condition of the samples. A flat surface is required to place the transducers. The possible number of signal channels

is 50 or 64 depending upon the spatial spacing interval. The Fourier transform of the time series in the time domain is not a problem because each signal has 4000 data points without having recourse to zero-padding. However, in the spatial direction where the transducer is moving away from the transmitting transducer (referring to Figure 4.1(c), there are, say at a fixed time, 50 or 64 spatial points for Fourier transform. The spatial series requires heavy zero-padding to obtain a good representation in the wavenumber or *k*-space. The *AR* method provides an alternative method to compute the spectral estimation.

The *AR* method has been extensively applied in borehole geophysics to determine phase velocities of sonic waves (McClellan, 1986; Lang, *et al* 1987). One of the important factors in the method is to determine the optimal order, p, for the data set at hands. A small order will result in too much smoothing and the spectral estimate will be coarse because some spectral peaks will be missed. However, too large an order will introduce noise into the estimation (Kay and Marple, 1981). It has been suggested (Lang, *et al*, 1987; Tsang and Rader, 1979; Kurkjian, 1985; Mclellan, 1986; Hsu and Esmersoy, 1992) that the range of p lies with $p \in \left[\frac{1}{4}M \sim \frac{1}{2}M\right]$, where M is the number of time series.

To illustrate the idea, we estimated the *PSD* of bone data using *AR* technique. The data was acquired from an ultrasound investigation of a bovine tibia (Figure 4.15) and more details about the acquisition will be provided in Chapter 4. There are 50 measurement records, each of which has 4000 points with 0.05 μs sampling interval. Each record was acquired at 1 mm spatial interval. Figure 3.3(a) shows the periodogram. The result shows four energy clusters with the first two being the strongest. Figures 3.3(b) – (d) show the *AR* estimates of the *PSD*. In Figure 3(b), the low order (p=1.5) *AR* result shows the first three clusters but fails to identify the small and high frequency cluster. With the *AR* order increasing, more energy information appears in the spectral image. Figure 3.3(c) and (d) show the *AR* estimates with order 25 and 40. The high order *AR* results were able to identify the small cluster at high

frequency. To examine the accuracy of estimation further, we compared a *k*-spectra at a fixed, say 0.375 MHz using periodogram and *AR* technique. Figure 3.4(a) displays the spectral curves normalized by periodogram. The *AR* results provide a good estimate of the peak location but fail to approximate the peak amplitude accurately. The low order p=15 *AR* estimation only accounts to 30% of the peak; while the high order p=40 accounts to 75% of the peak. Significant amount of energy was lost in the *AR* technique. Figure 3.4 (b) shows the self-normalized spectral curves. As shown, the location of the peak was accurately located at 120 cycles/meter. The bandwidth was poorly estimated. However, the results show that the *AR* technique is an alternative method to estimate the *PSD* of the signals. Higher order is required to provide an accurate estimation and there is a trade-off between accuracy and computation efficiency.

The study in *AR* process is limited to this chapter. This method and its application has the capabilities to be extended in future researches.

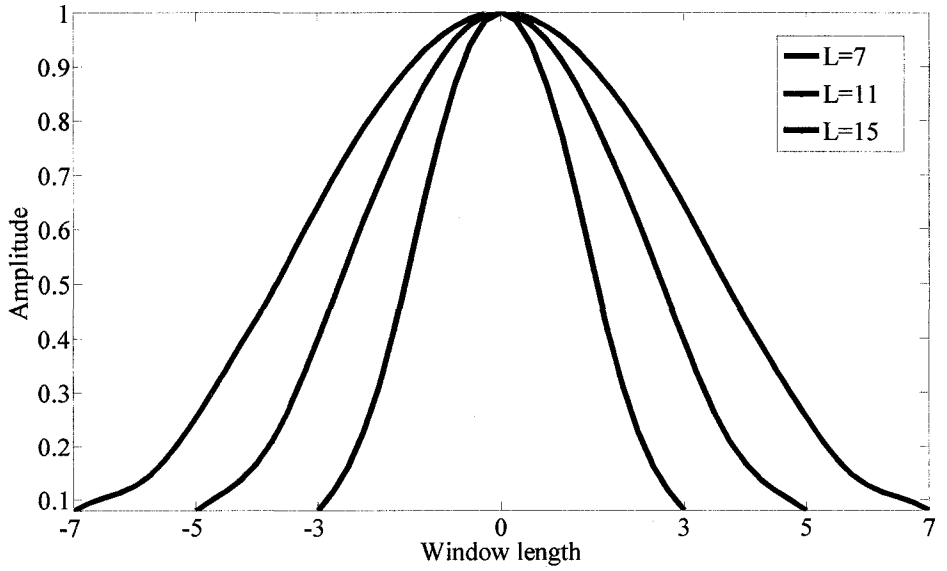

Figure 3.1 1-*D* Hamming window with window length $L = 7$, 11, and 15.

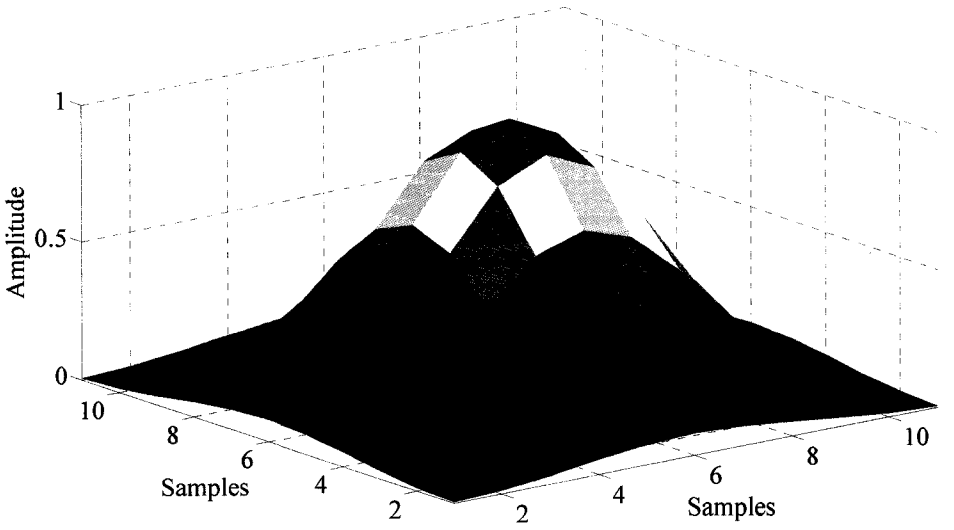

Figure 3.2 2-*D* Hamming window with window length L =11.

(a)

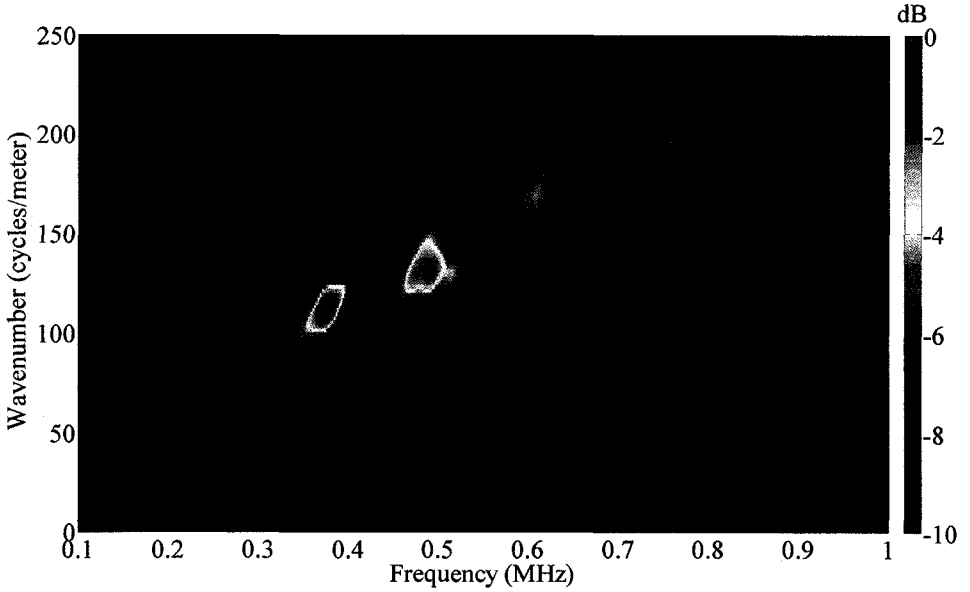
dB
0
-2
-4
-6
-8
-10
250
200
150
100
50
0
Wavenumber (cycles/meter)
0.1
0.2
0.3
0.4
0.5
0.6
0.7
0.8
0.9
1
Frequency (MHz)

(b)

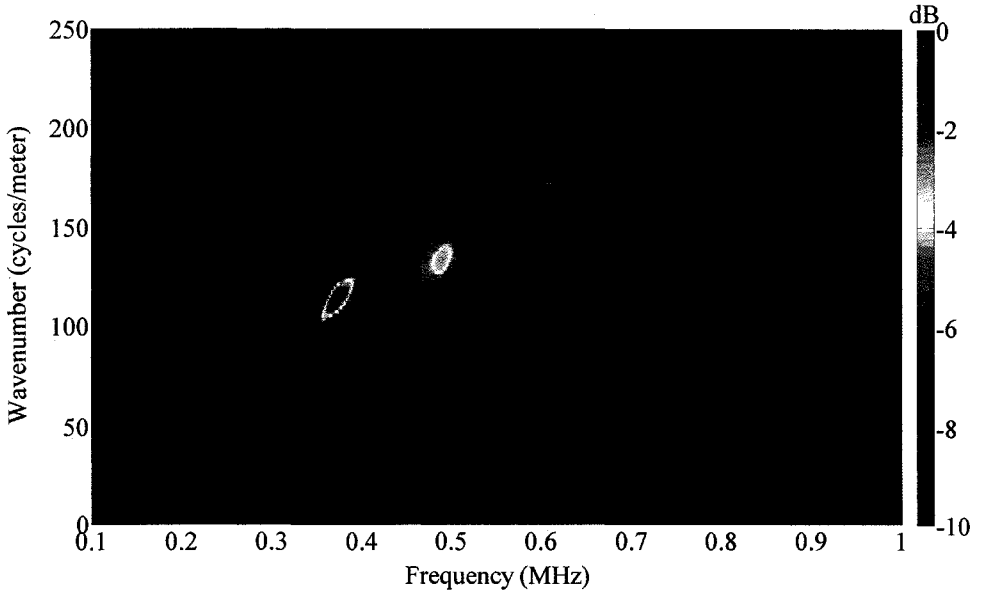
dB
0
-2
-4
-6
-8
-10
250
200
150
100
50
0
Wavenumber (cycles/meter)
0.1
0.2
0.3
0.4
0.5
0.6
0.7
0.8
0.9
1
Frequency (MHz)

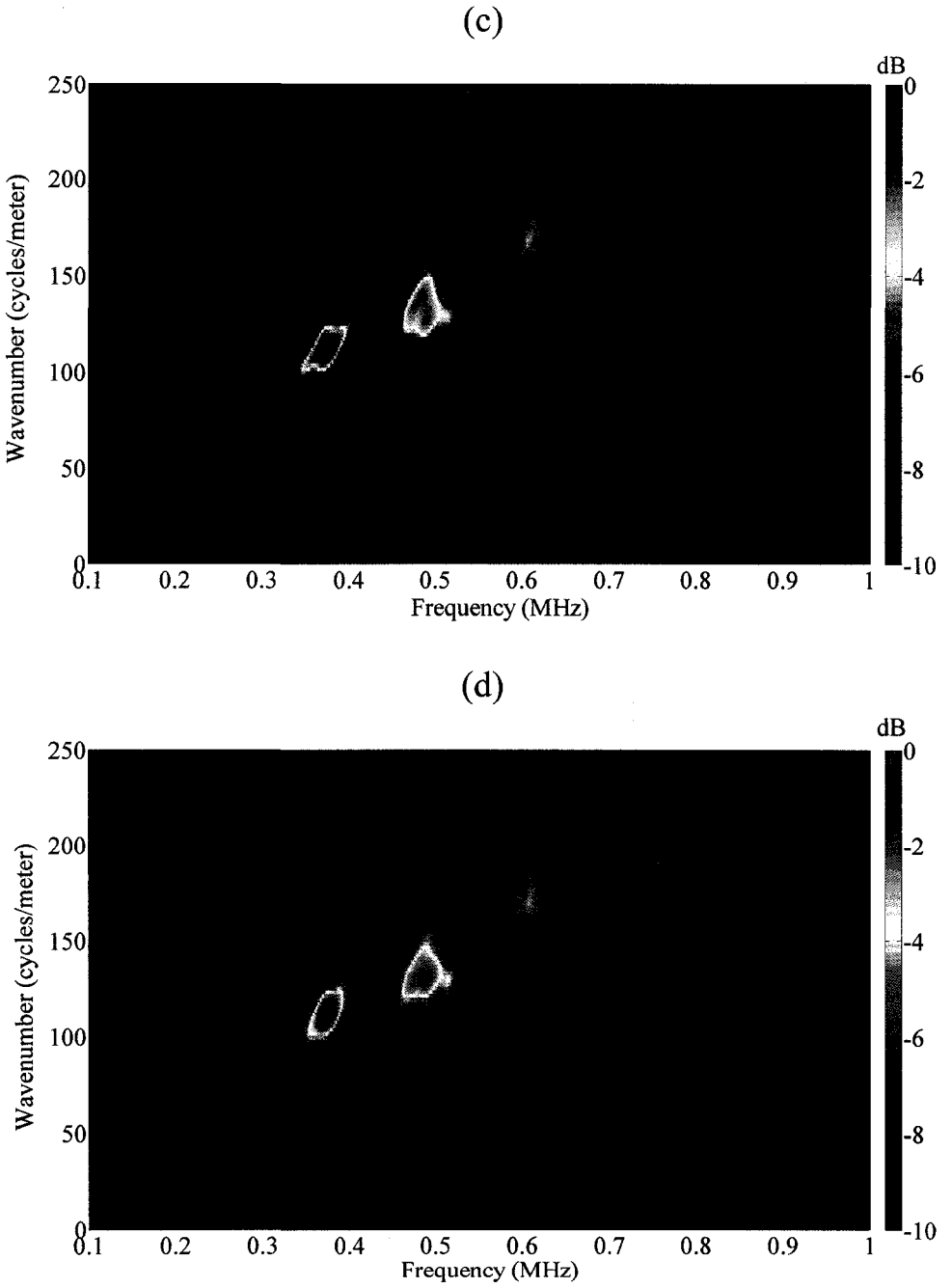

Figure 3.3 Power spectral densities: (a) periodogram; (b) *AR* estimation of p=15; (c) *AR* estimation of p=25; (d) *AR* estimation of p=40.

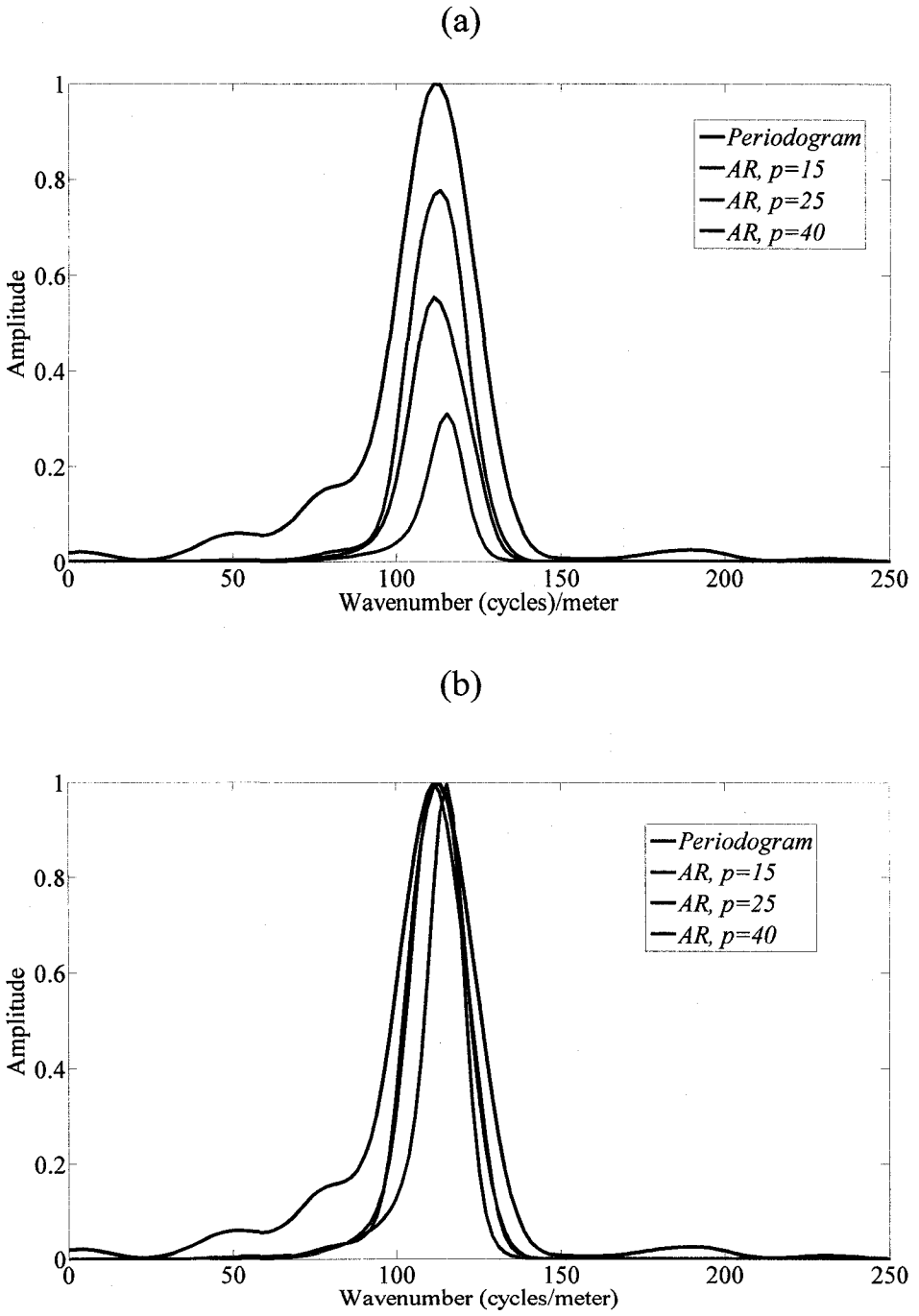

Figure 3.4 Comparison of *k*-spectra at 0.375 MHz from Figure 3.3 (a)-(d): (a) Spectra normalized by the maximum value of the spectrum from periodogram; (b) self-normalized spectra.

Chapter 4

Experimental Studies of Ultrasound Propagation in Phantom and Bovine Tibia[1]

In most works, long bone was usually modeled by a free plate (Moilanen, *et al*, 2006 and 2007; Protopappas, *et al*, 2006) bounded below and above by air or a plate overlying water, which mimics marrow (Lee and Yoon, 2004). Lamb modes such as A0, S0 and S2 have been observed in experimental data (Lefebvre, *et al*, 2002; Nicholson, *et al*, 2002; Protopappas, *et al*, 2006; Tatarinov, *et al*, 2005). Lamb wave theory provides a simplistic model to understand interaction of guided waves with bone tissues. Long bones are effectively irregular cylindrical tubes filled with marrow. Since marrow has much larger acoustic impedance than air, the transmission coefficient of the interface between bone and marrow is larger than that between bone and air. Leakage of energy within the cortex into the underlying marrow might cause strong attenuation and dispersion. Based on this argument, free plate theory will perhaps underestimate the effects of the underlying marrow on the dispersion characteristics (Lefebvre, *et al*, 2002; Ta, *et al*, 2007). Ta, *et al* (2007) first reported to apply cylindrical longitudinal guided waves to describe the ultrasonic wave propagation in bone. In their study, low-order longitudinal guided wave modes were reported in bovine tibia. However, their result was based on a hollow cylindrical tube model and the influence of marrow was ignored.

To illustrate an example, we simulated the dispersion curves for a liquid-filled cylinder and a free plate. We chose the parameters relevant to the bone specimen used in this thesis. The parameters of the bone model are listed in Table 4.1 (Kaye and Laby, 1995; Wu and Cubberley, 1997). The model was elastic. For the cylinder, the ratio of the wall thickness to outer radius was 8.9:16.8. Figure 4.1(a) shows the

[1] *Part of the results has been submitted for publication.*

phase velocity dispersion curves of the first thirteen longitudinal guided wave modes for a range of frequency-thickness product ($f \cdot d$) from 0 to 9 MHz·mm where d refers to the thickness of the cortical layer. All modes except the lowest mode, L(0,1) have cutoff frequencies. At large $f \cdot d$ values, the high-order modes converge to the shear velocity of the cortical layer, while the low-order modes converge to the Raleigh velocity, v_R which is approximately given by Viktorov (1967):

$$v_R \approx v_{s,s} \times \frac{0.87 + 1.12\sigma}{1+\sigma} \tag{4.1}$$

where $\sigma = \frac{v_{s,c}^2 - 2v_{s,s}^2}{2\left(v_{s,c}^2 - v_{s,s}^2\right)}$ is the Poisson's ratio. In this case, the velocity of Rayleigh wave is $v_R \approx 1839$ *m/s*. All works reported so far with relevance to guided wave investigation in long bones fall below 2.5 MHz·mm (Lefebvre, *et al*, 2002; Nicholson, *et al*, 2002; Protopappas, *et al*, 2006; Ta, *et al*, 2006; Tatarinov, *et al*, 2005). In our work, our $f \cdot d$ range of investigation is between 3 and 7 MHz·mm. Figure 4.1(b) shows the phase velocity dispersion curves of the first four symmetric and five anti-symmetric Lamb modes for a free elastic plate. The plate was 8.9 mm thick. At very large $f \cdot d$, the modes are expected to asymptotically approach $v_{s,s}$ or v_R. However, at low and mid $f \cdot d$ ranges, the dispersion curves between the two geometrical models are significantly different. Since long bone is an irregular cylindrical tube filled with marrow, a cylindrical tube model is much closer to approximate long bone.

4.1 Experimental setup and materials

4.1.1 Experimental setup and data acquisition

An axial transmission experiment was set up as shown in Figure 4.2(a). Two angle beam transducers (Panametrics C548, Waltham, MA) with center frequency of 1 MHz were affixed to the wedges (Panametrics ABWM-7T-70°, Waltham, MA).

The angle of the wedge is the shear wave transmitted angle in steel. The transducer-wedge system was positioned collinearly on the phantom and bone surface where the ultrasound gel was used as coupling agent. One system was a transmitter and the other a receiver. The transmitter was energized by a Panametrics 5800 P/R (Panametrics, Waltham, MA) with bandwidth from 50 KHz to 35 MHz. The incident angle of compressional wave was 51°. Figures 4.2(b) and (c) show the transducer system positions on phantom and bone samples. Consistent pressure was applied to the transmitter and receiver during measurement. The initial transmitter-receiver separation or offset was 24 mm measuring from their centers. The receiver was moved away from the transmitter by 1 mm interval and measurement was made at each spacing increment. Due to the wedge, the signals are delayed by a constant 14.6 μs as compared to signals recorded without a wedge. The constant time was obtained by dividing the path ultrasound travels within the wedge (2×19.5 mm) by the compressional velocity (2680 m/s) of the wedge. The signal detected by the receiver was digitized by and displayed on a 200 MHz digital storage oscilloscope (LeCroy 422 WaveSurfer, Chestnut Ridge, NY). To increase signal-to-noise ratio, the digitized waveform was stored in the internal memory and continuously averaged 128 times. The signal was further decimated to 4000 samples with sample interval of 0.05 μs. The recorded signals made up a distance-time (x-t) matrix of amplitudes or an x-t echogram.

4.1.2 Phantom specimen

A commercial nylon tube (NYLATRON GS, Johnston Industrial Plastics Ltd, Edmonton Canada) filled with water was used as a long bone phantom in this study. The solid tube and water mimic cortical bone and marrow respectively. Both ends of the tube were stopped by rubber stoppers. The tube is 66 cm long; the wall thickness is 7.80 mm; the inner diameter is 22.92 mm. Figure 4.3 displays the image of phantom. The region of measurement is 88 mm long.

4.1.3 Bone specimen

A bovine tibia was used in this study. The overlying tissues of the tibia were removed. The tibia was cut by a band saw to keep the mid-shaft portion. Figure 4.4 shows an x-ray computed tomographic image of the specimen reconstructed by a Siemens Sensation 16 slice CT system. Bone thickness was obtained from the image using measuring software in a CT reviewing station. The region of interest shown in Figure 4.4 is a reasonably flat surface for the measurement and is 74 mm long. The average cortical wall thickness within the region is 8.90 mm and the inner diameter is 15.80 mm.

4.2 Discussion of Experimental Results

4.2.1 Phantom data

Sixty-four measurements were obtained along the mid section of the tube at 1 mm spacing interval. The dataset was stored in a 64 × 4000 matrix. The total duration of each measurement was 200 μs but only 100 μs of data was plotted. Figure 4.5(a) shows the *x-t* echogram of all 64 measurements with a 1 mm spacing interval. The amplitudes were not scaled and thus represented the true amplitudes among measurements. Strong bulk waves such as first arrival signals (*FAS*) are evident at near offsets from 24 mm around 26 μs to 40 mm around 30 μs. The signals are transient and decay rapidly with distance after 40 mm offset. To display late arrival signals (*LAS*) and signals at large offset, we normalized the signals individually by its maximum value. Figure 4.5(b) shows the self-normalized echogram. At offset larger than 40 mm, the *LAS* are dominated by the highly dispersive wave trains, which are characteristic of waveguide.

We computed three theoretical arrival time curves: bulk compressional wave, bulk shear wave, and Raleigh wave. Compressional and shear velocities used are provided in Table 4.2. Raleigh wave velocity is given by equation (4.1). The arrival times were calculated by dividing distance traveled by elastic velocity. The traveling

distance was the shortest path from the transmitter to the receiver. A constant of 14.6 μs was also added to the results to account for the traveling time within the two wedges. Figure 4.6 shows the *x-t* echogram of sixteen measurements with a 4 mm spacing interval and the three travel time curves. All three waves are clearly seen at small offset. The theoretical travel times underestimate the signals because absorption mechanism delayed the signals in bone. Bulk compressional wave reflection and multiple reflections are significant after the bulk longitudinal wave. At large offset, the bulk shear and the Raleigh waves are less visible due to the interference by guided waves. To reduce the influence of bulk waves in our guided wave analysis, we muted the first 6 μs from the onset of each record. Figure 4.7(a) shows the cut off the muting window. Figure 4.7(b) shows the time signals after muting.

The 2-D periodogram shown in Figure 4.8 is an estimator of the power spectral density of the data. The figure shows four distinct energy clusters above -4 dB peaking around 210 kHz (P1), 320 kHz (P2), 480 kHz (P3) and 500 kHz (P4) with the first two being the strongest. We refer the four clusters as P1, P2, P3 and P4 for discussion purpose where "P" stands for phantom. Considering the input frequency was 1.0 MHz, the high frequencies were significantly attenuated.

To obtain the phase velocity of wave propagation in phantom, the spectra of the periodogram are mapped from frequency-wavenumber (*f-k*) domain to frequency-phase velocity (*f-c*) domain by using the following expression:

$$D(f,c) = P(f,k=2\pi f/c) \tag{4.2}$$

where $D(f,c)$ is the spectral in frequency-phase velocity domain, c is the phase velocity. To calculate the phase velocity, it is not good to divide the frequency components by wavenumber directly. We apply a method to map the energy from frequency-wavenumber to frequency-phase velocity. It is clear that to compute the dispersion map $D(f,c)$, one requires interpolation because regular samples of c does

not necessarily correspond to regular samples of k. Our experience shows that a simple linear interpolation scheme suffices to estimate $D(f,c)$.

To further interpret the data, we attempted to identify the dominant guided wave modes propagating in the phantom. The theoretical dispersion curves were calculated by DISPERSE and shown in Figure 4.9.

Using $c = 2\pi f/k$, the phase velocities of the clusters were found to be approximately the same. Figure 4.10 portraits the matrix $D(f,c)$ or the dispersion spectra, which better illustrate the phase velocity information. The peaks of P1, P2, P3 and P4 travel at phase velocities of 4.0 km/s, 3.4 km/s, 3.3 km/s and 3.7 km/s respectively. Figure 4.10 also shows the theoretical dispersion curves of longitudinal modes for a water-filled viscoelastic cylindrical phantom model. We found five longitudinal modes associated with the energy clusters. L(0,8) mode almost passes through P1; P2 is bounded between L(0,11) and L(0,12); L(0,16) and L(0,17) modes pass by the edges of P3 and P4 respectively. The particle polarization of the longitudinal modes is in the plane defined by the transducer-receiver pair. As discussed in chapter 2, both the experimental configuration and the transducer-wedge systems emphasize longitudinal guided wave modes. There is no torsional wave. The flexural modes, if there is any, will be extremely weak (Zemanek, 1971; Silk and Bainton, 1979; Rose, 1999)

The energy clusters are well separated in frequency; thus we attempted to isolate the clusters and studied the time signatures of guided wave modes. We bandpassed P1 and P2 in frequency separately with a Tukey window (Harris, 1978):

$$W_{N,r}(k)=\begin{cases} \frac{1}{2}[1+\cos(\frac{2\pi}{r}\frac{(k-1)}{N-1}-\pi)], & k<\frac{r}{2}(N-1)+1 \\ 1, & \frac{r}{2}(N-1)+1\le k\le N-\frac{r}{2}(N-1) \\ \frac{1}{2}[1+\cos(\frac{2\pi}{r}-\frac{2\pi}{r}\frac{(k-1)}{N-1}-\pi)], & N-\frac{r}{2}(N-1)<k \end{cases} \qquad (4.4)$$

where, k=1 to N, N is the window length and r is the ratio of taper to constant section and the value is between 0 and 1. A rectangular window is for r=0, and a Hann window (Oppenheim, *et al*, 1999) is for r=1. The default value for r is 0.5. Figure 4.11 displays some windows with 128 points but of different taper ratio, r. Our experience showed that a Tukey window of 0.25 order was adequate to provide softer taper on both frequency ends and avoid aliasing while passing without attenuation most of the energy of interest. The parameters of the bandpass filters were 150/168/280/300 KHz and 250/275/425/450 KHz for P1 and P2 respectively. We obtained the time signals by 2-D inverse *FFT*.

In order to compare the bandpassed results with the simulation results, we generated simulated signals by DISPERSE. Figure 4.12(a) shows the source signal of the transducer we used. Figure 4.12(b) shows the simulated source signal by DISPERSE. They are quite similar. Figures 4.13(a) and (b) display the time signatures of P1 and P2 respectively. All results were computed for an offset of 53 mm. When comparing with P1, P2 has larger temporal amplitude; the time history of P2 shows higher frequency content and is more complicated due to existence of more than one mode. Figures 4.13(c) and (d) portraits the simulated results for the L(0,8), L(0,11) and L(0,12) modes. The theoretical predictions are very similar to experimental results.

To further confirm the validity of the processing procedures, we generated a numerical data set using the phantom model (Table 4.2) for the three modes: L(0,8), L(0,11) and L(0,12). Sixteen records starting at 40 mm offset and at 1 mm spacing interval were simulated. Compared with real signals, the simulated time signals have different time interval. We applied a 1-D interpolation on the simulated signals so that they have the same sampling rate as that of the original signal. Thus we make sure that both the simulated signals and real signals have same time interval. Moreover, due to the smaller number of records, we applied the *AR* method to obtain the power spectral density (*PSD*). The order of *AR* method was 8. Figure 4.14 shows

the dispersion diagram of the simulated dataset. As expected, P1 and P2 are successfully identified by the dispersion curves of the three modes used.

4.2.2 Bone specimen

Fifty measurements were acquired at 1 mm spacing interval on a bovine tibia. The region of interest was about 74 mm long and the surface was reasonably flat (Fig. 3). Figures 4.15(a) and (b) display the echograms of the original data and self-normalized data respectively. The *FAS*s have strong presence in the data. Figure 4.16 shows the echogram but with 4 mm interval of bovine tibia. Three arrival times of bulk waves are superimposed. At offset larger than 40 mm, the guided waves are seen as highly dispersive *LAS*. Using 2680 m/s and 4000 m/s (Kaye and Laby, 1995) as the longitudinal wave velocities of the wedge and bone, the critical angle is 42° by Snell's law. Since the incident angle of the primary beam is 51°, most of the transmitted energy is critically refracted and travels close to the bone surface. We muted the first 4 μs from the onset of each record for guided wave analysis. Figures 4.17(a) and (b) display the cut off of the muting window and the signal after muting respectively.

Figure 4.18 shows the *PSD* where four distinct energy clusters can be easily identified. The signals were significantly attenuated within the cortical layer by the absorption process. The first two clusters are more energetic than the latter two, which have energy below -4 dB. The clusters travel approximately at the same phase velocity. Fig. 9(b) displays the dispersion spectra. The clusters peak at 380 KHz (B1), 490 KHz (B2), 610 KHz (B3), and 760 KHz (B4) with the corresponding phase velocities of 3.4 km/s, 3.7 km/s, 3.6 km/s and 3.9 km/s. We refer the clusters as B1, B2, B3, and B4 where "B" stands for bone. The frequency bands of the clusters are well separated and their bandwidths are approximately 60 KHz (350 – 410 KHz), 80 KHz (450 – 530 KHz), 40 KHz (590 – 630 KHz), and 40 KHz (740 – 780 KHz) for B1, B2, B3, and B4 based on half maximum of the peak intensity relative to -10 dB. To further interpret the data, we attempted to identify the dominant guided wave

modes propagating in the bone sample. We calculated theoretical guided wave dispersion curves using a viscoelastic cylindrical tube filled with liquid. Table 4.1 lists the parameters of the bone model.

Theoretical dispersion curves of bone are displayed in Figure 4.19. It can be seen that the dispersion curves change a lot when the attenuation of cortical bone and marrow is considered. Figure 4.19(a) portraits the dispersion curves based on an elastic bone model. There are thirteen longitudinal guided wave modes are shown. Figure 4.19(b) displays the dispersion curves with the anelastic bone model, which has only eleven longitudinal guided wave modes are shown in the same frequency-thickness range. Comparing with these two theoretical results, the attenuation affects the higher order mode in high frequency range. Theoretical computation shows that there are four high-order modes passing through the clusters. Figure 4.20 shows the dispersion mapping result. The four packets are identified respectively as L(0,7) and L(0,8), L(0,9), and L(0,11).

To obtain the time characteristics of the two strongest modes, i.e., L(0,7) and L(0,8), we bandpassed the clusters in frequency with a Tukey window of 0.25 order separately. The parameters of the bandpass filters were 280/300/460/480 KHz and 400/425/575/600 KHz for L(0,7) and L(0,8) respectively. Then we performed a 2-D inverse *FFT* on the bandpassed spectra. Figures 4.21(a) and (b) show the time signatures of B1 and B2 respectively at 53 mm offset. All results were computed for an offset of 53 mm. The amplitude of B1 is stronger than that of the B2. Figures 4.21(c) and (d) show the corresponding simulated results for L(0,7) and L(0,8) modes respectively. We didn't expect a perfect match between two data sets because the bone model used for simulation was only an approximate to the real bovine tibia. The perfect cylindrical tube model was homogeneous along the long axis and had constant wall thickness while the bovine tibia was inhomogeneous with irregular cortical thickness. However, both experimental and simulated results have similar characteristic features and good agreement.

Table 4.1 Parameters of the bone model used to generate dispersion curves.

Parameters	Cortical bone	Marrow
Thickness (mm)	8.9	7.9 (inner radius)
Longitudinal wave velocity (m/s)*	4000	1480
Shear wave velocity (m/s)*	1970	n/a
Attenuation of compressional wave (dB/MHz/cm)*	5	0.8
Attenuation of shear wave (dB/MHz/cm)*	11	n/a

*Parameters obtained from Kaye and Laby (1995) and Wu and Cubberley (1997).

Table 4.2 Parameters of the phantom model used to generate dispersion curves.

Parameters	Phantom model	
	solid	water
Thickness (mm)	7.8	11.46 (inner radius)
Compressional wave velocity (m/s)*	2900	1500
Shear wave velocity (m/s)*	1200	n/a
Attenuation of compressional wave (dB/MHz/cm)*	0.21	0.8
Attenuation of shear wave (dB/MHz/cm)*	0.79	n/a

*Parameters obtained from Kaye and Laby (1995)

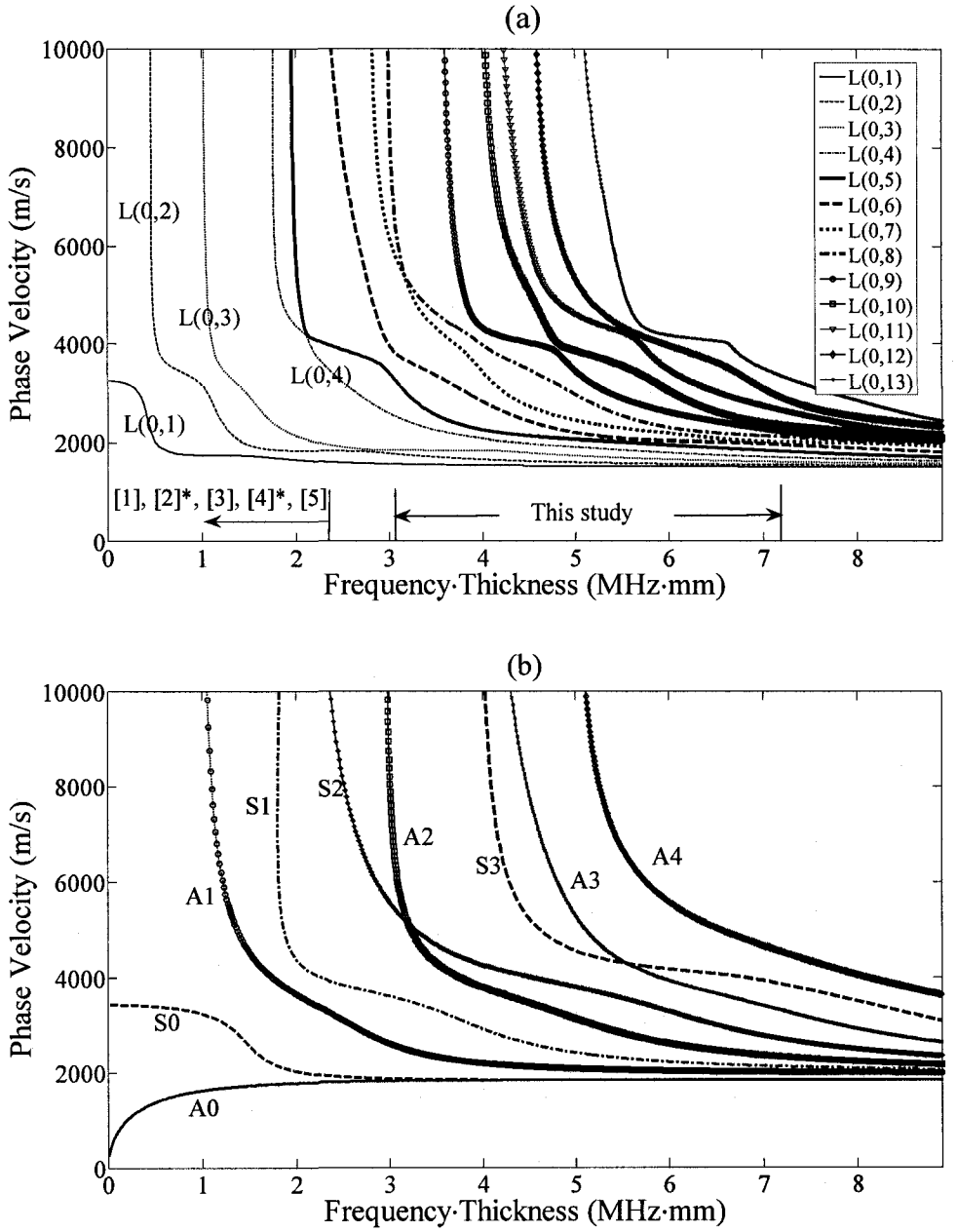

Figure 4.1 Theoretical dispersion curves of guided waves: (a) cylindrical longitudinal modes; (b) Lamb modes. The cylindrical tube model was an elastic bone model with parameters given in Table 4.1. The plate model was an 8.9 mm thick plate with the same velocities and density as those of the bone model. The asterisk (*) in (a) denotes previous works using cylindrical tube model; otherwise, plate model was used ([1]-[5] indicates Nicholson, *et al*, 2002, Lefebvre, *et al*, 2002, Protopappas, et al, 2006, Lee and Yoon, 2004, Ta, *et al*, 2006, respectively).

(a)

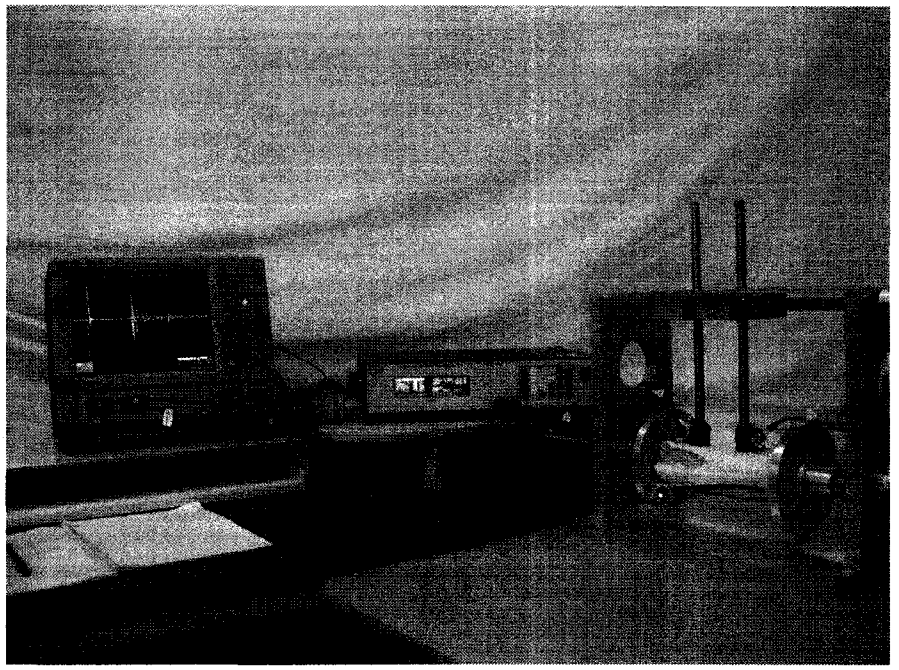

(b)

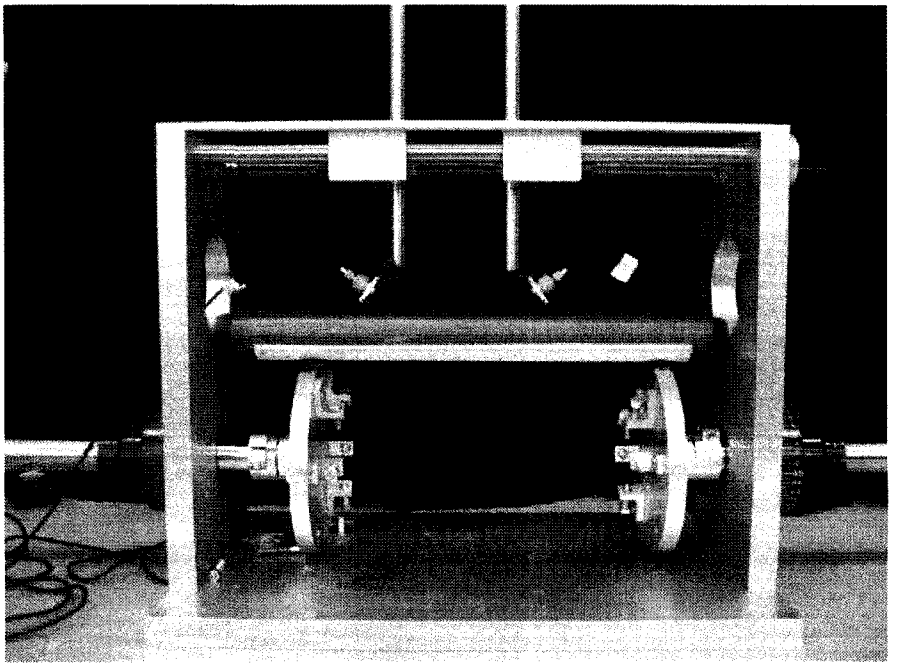

(c)

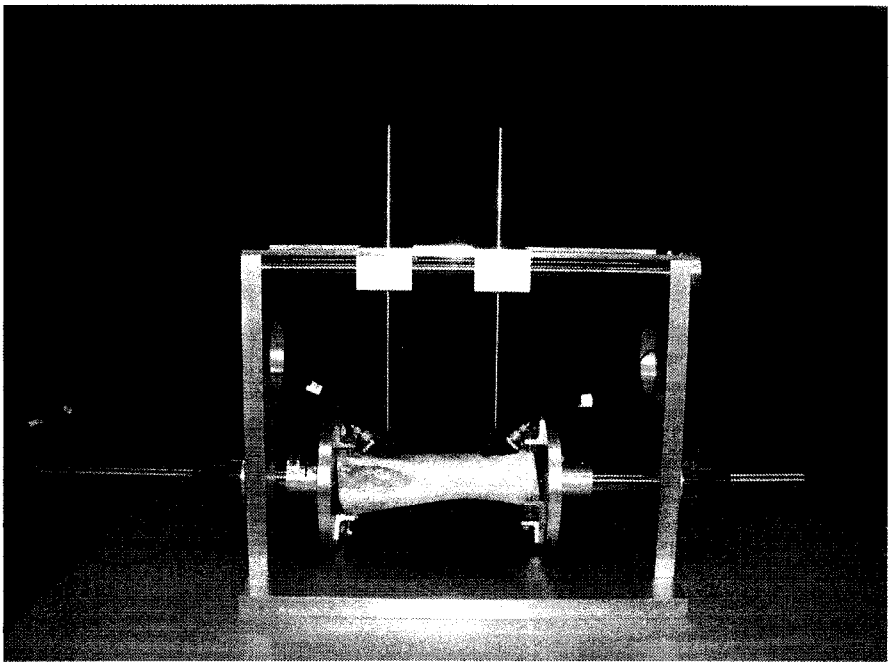

Figure 4.2 Experimental setup: (a) overview of experimental setup; (b) setup for phantom; (c) setup for bovine tibia.

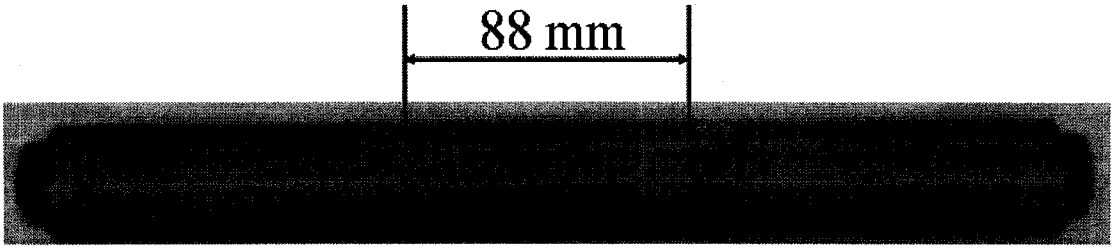

Figure 4.3 A nylon tube; the vertical bars indicate the region of investigation.

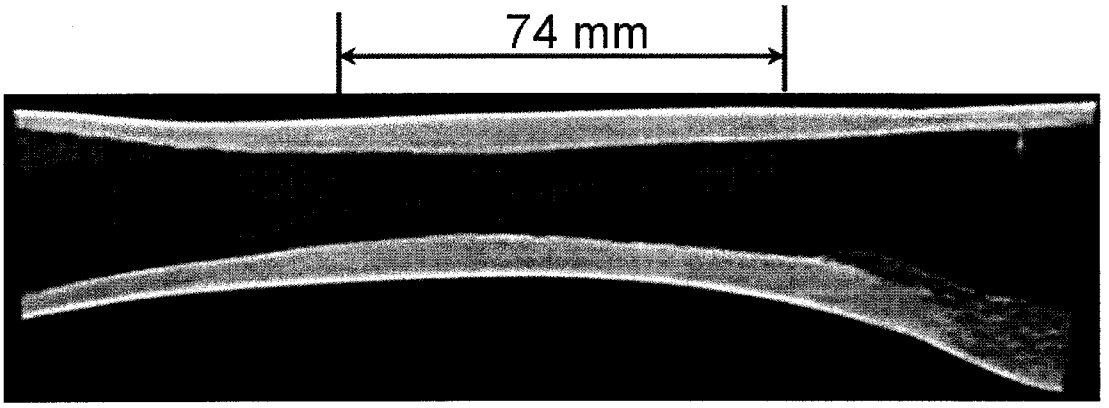

Figure 4.4 An x-ray computed tomographic image of the bovine tibia. The vertical bars indicate the region of investigation.

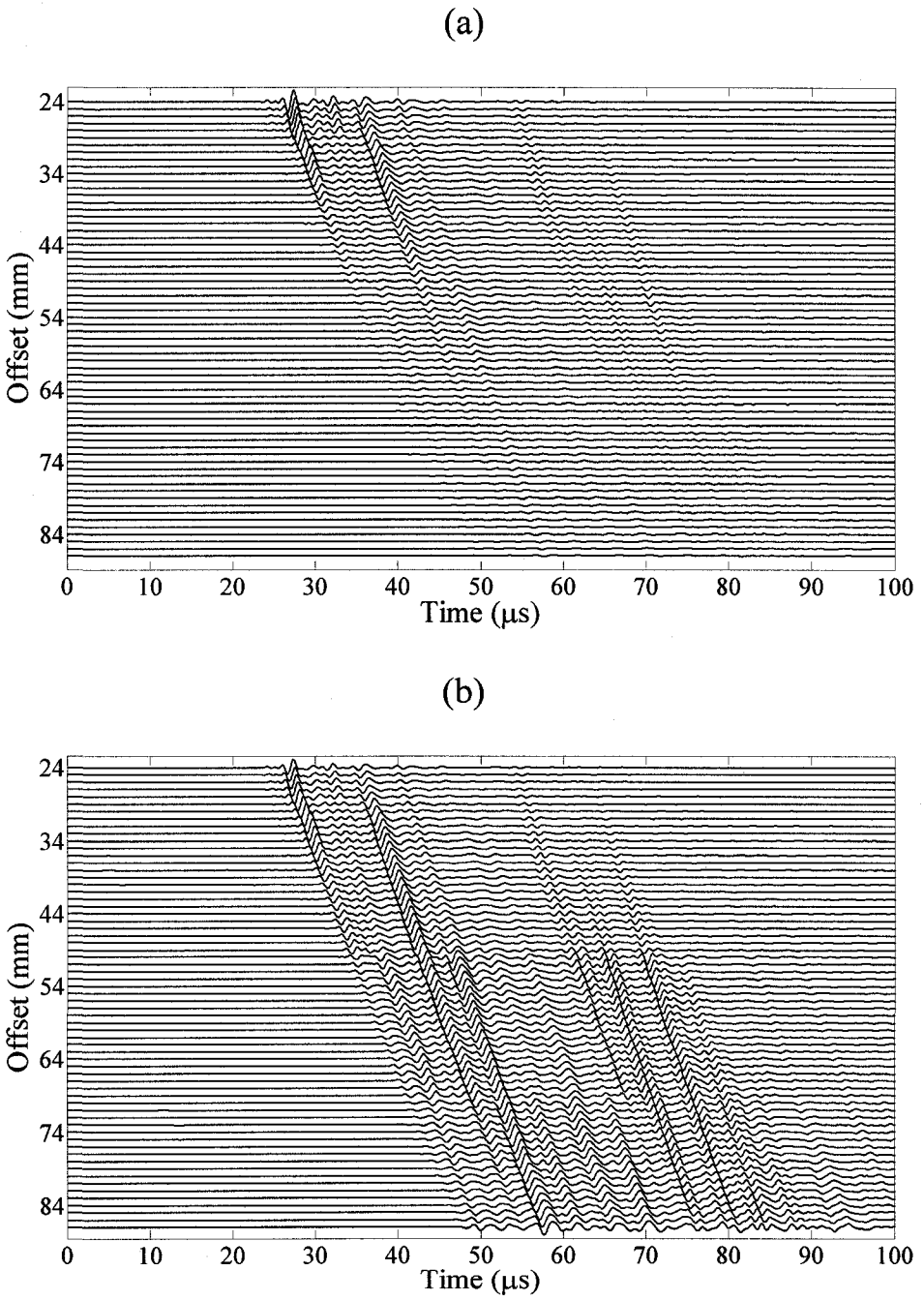

Figure 4.5 Echogram of the phantom data: (a) original data without normalized; (b) self normalized data.

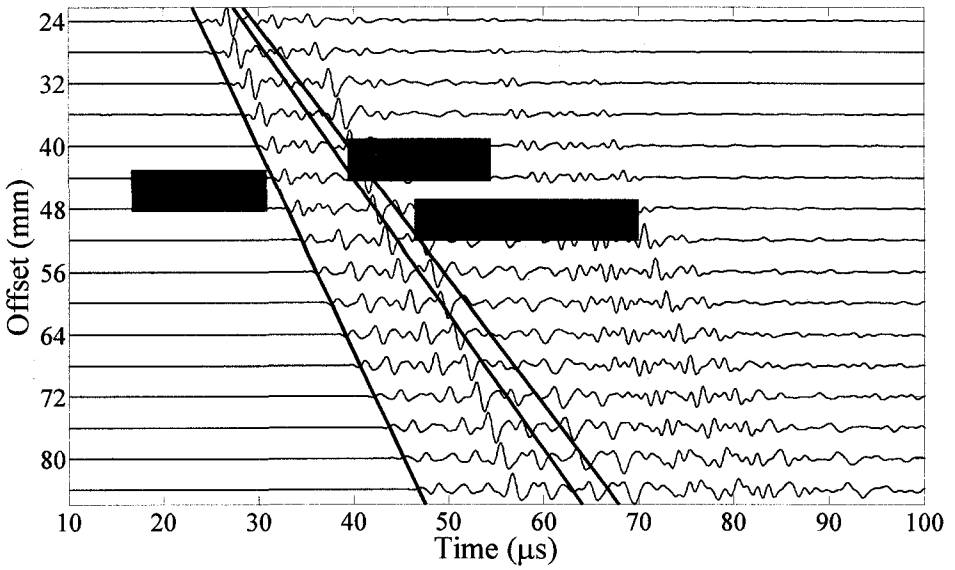

Figure 4.6 Self-normalized echograms of phantom dataset with 4 mm interval shown in Figure 4.5(b). The theoretical arrival time of the bulk compressional wave, bulk shear wave and Rayleigh wave are superimposed.

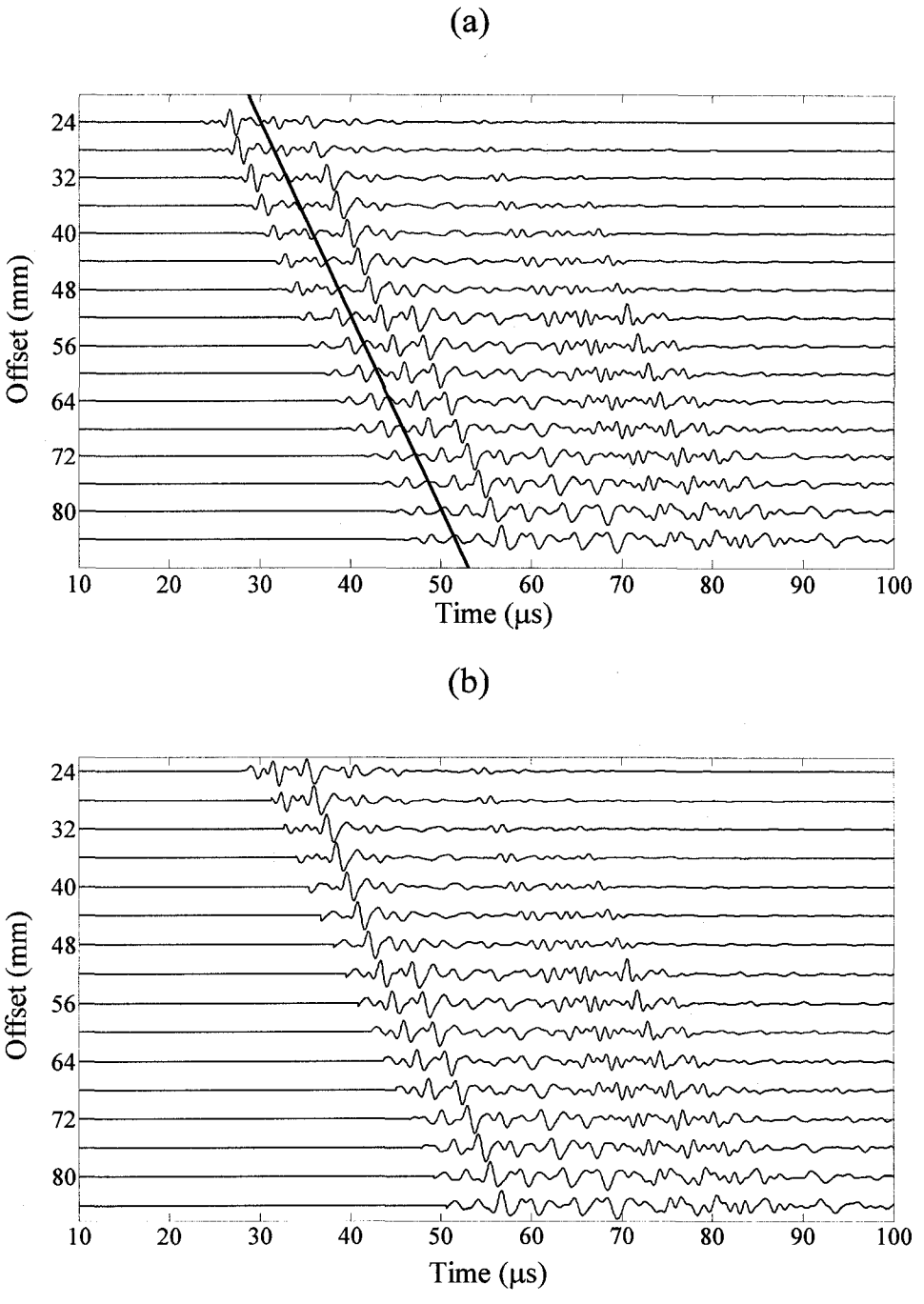

Figure 4.7 Echogram of the phantom data: (a) before muting. The red line indicates the cut off of the muting window; (b) after muting.

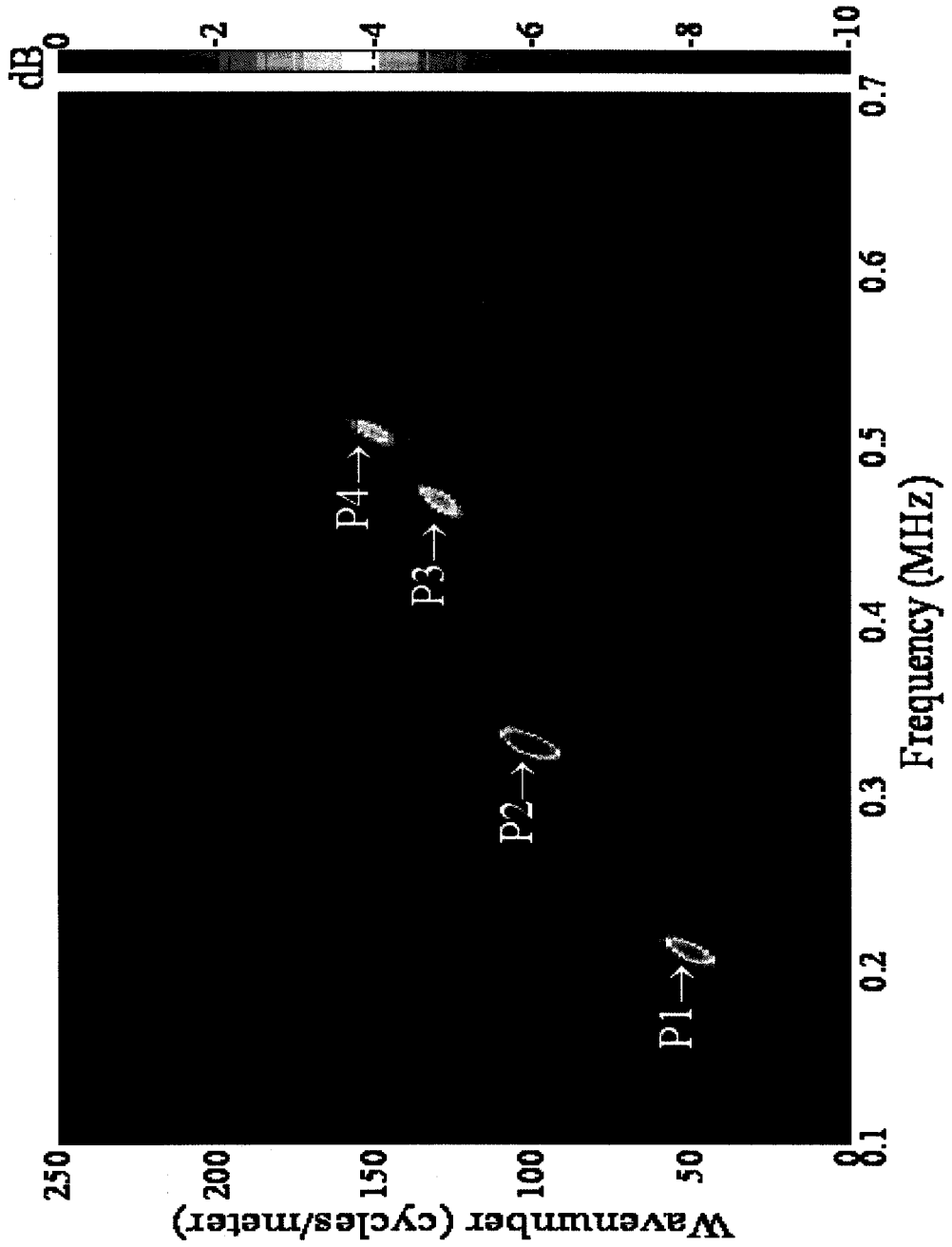

Figure 4.8 The 2-D periodogram of the phantom data.

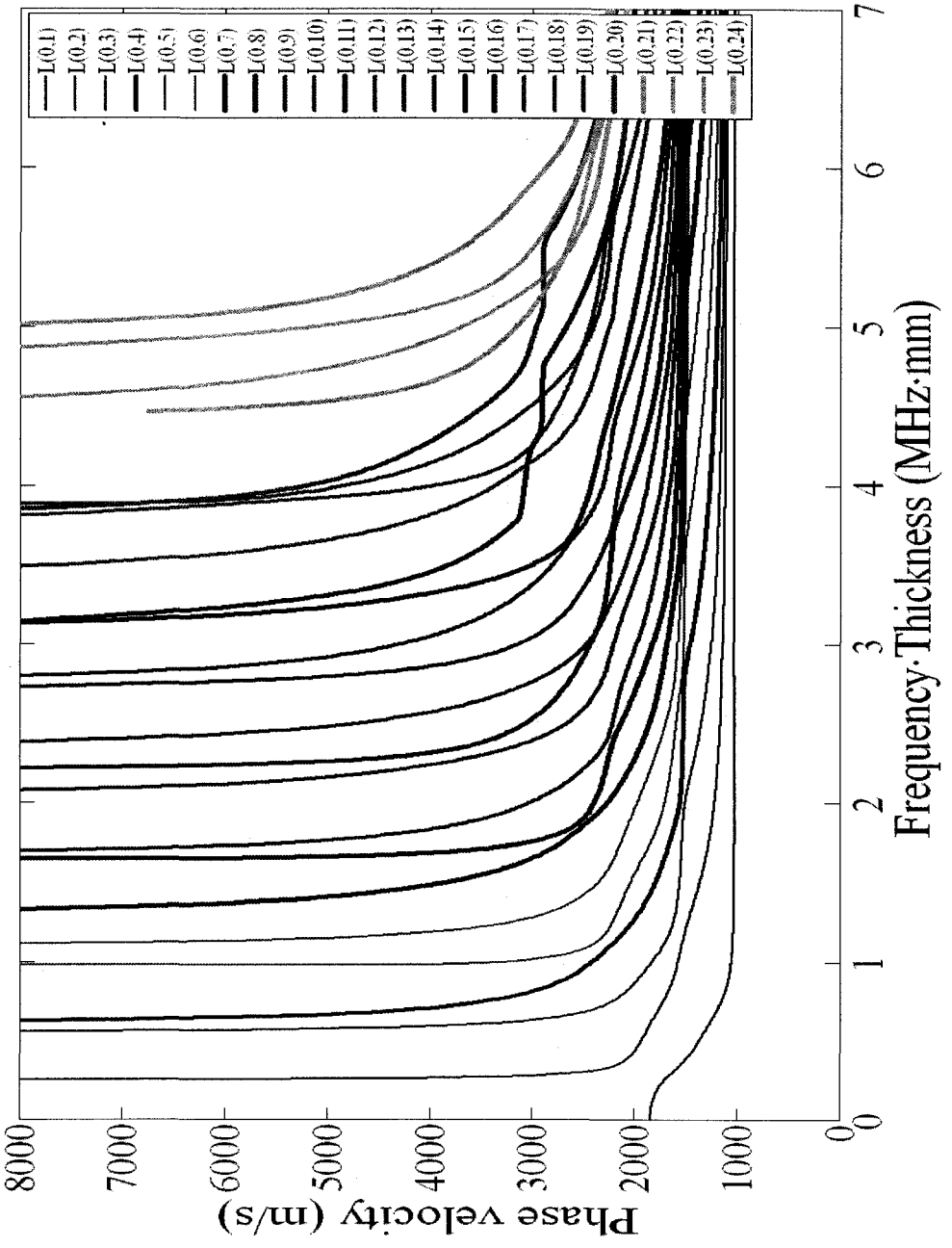

Figure 4.9 Theoretical dispersion curves of longitudinal guided wave modes of a nylon tube. The parameter is given by the phantom model in Table 4.2.

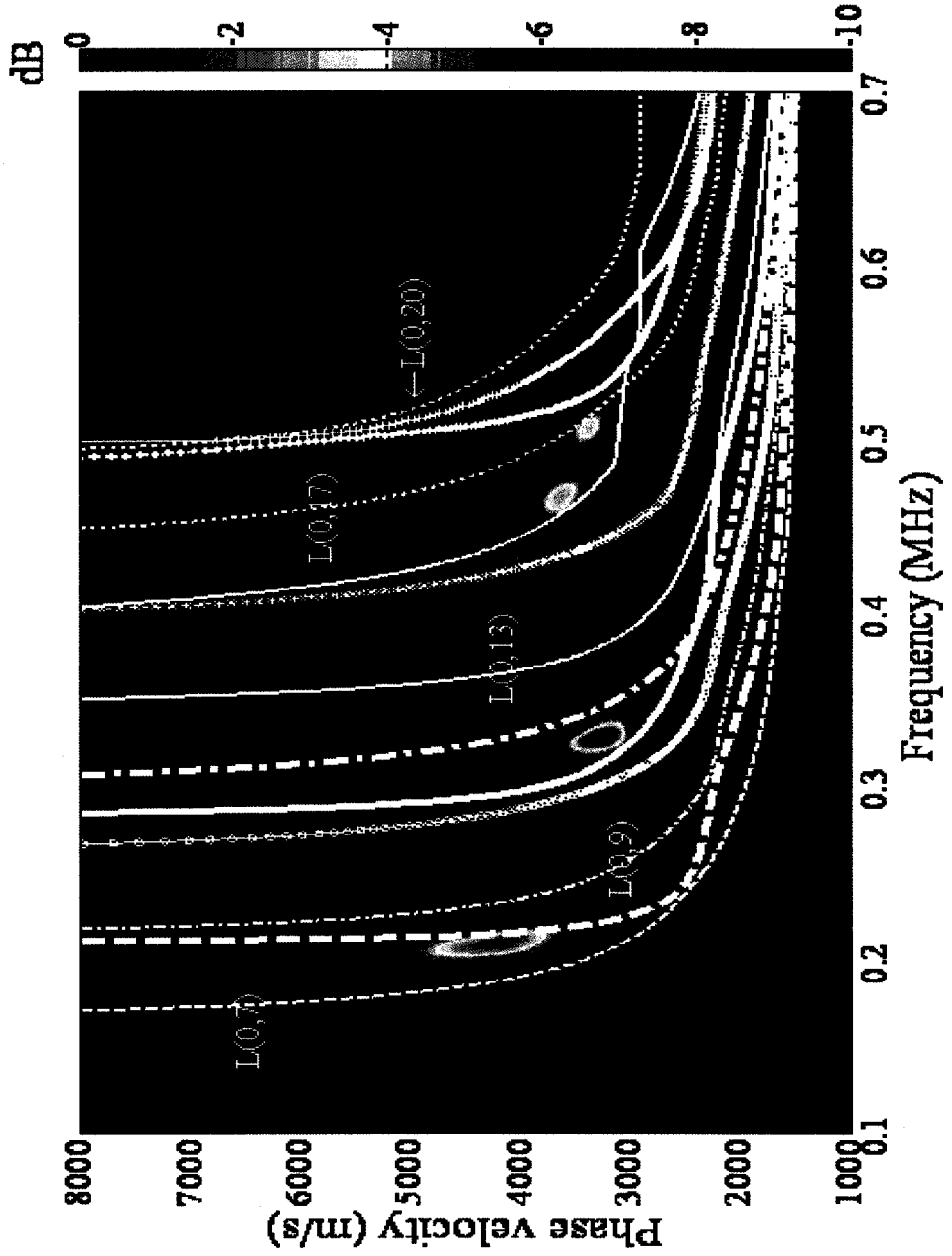

Figure 4.10 The dispersion diagram of phantom superimposed by the theoretical dispersion curves.

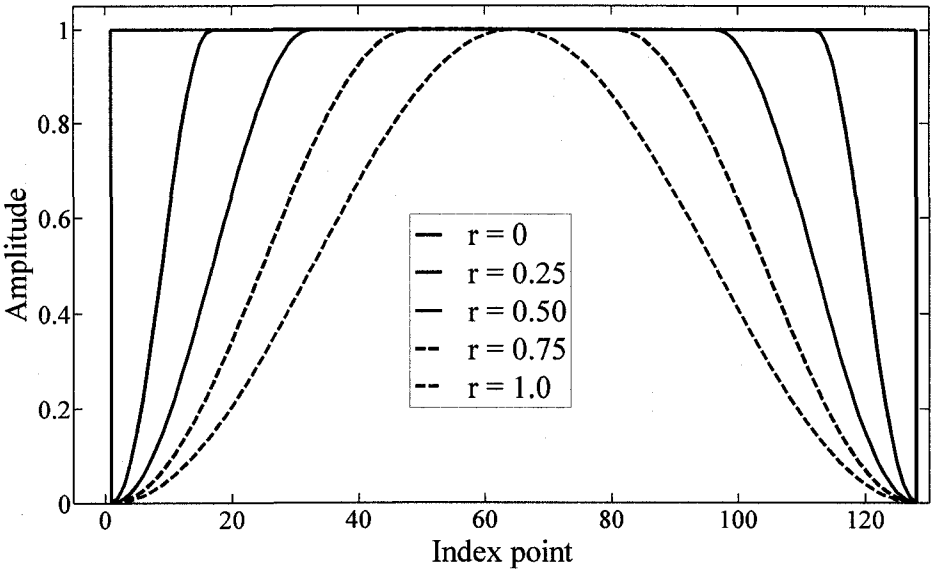

Figure 4.11 128-points Tukey tapers with different *r*-values.

(a)

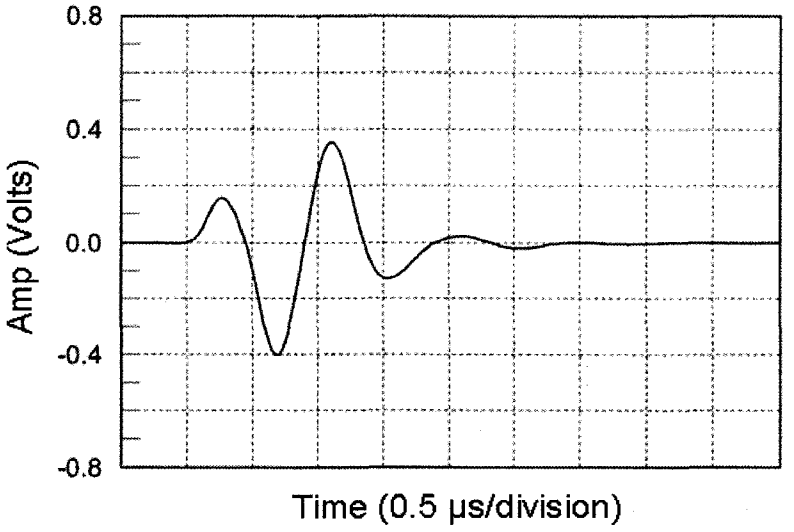

(b)

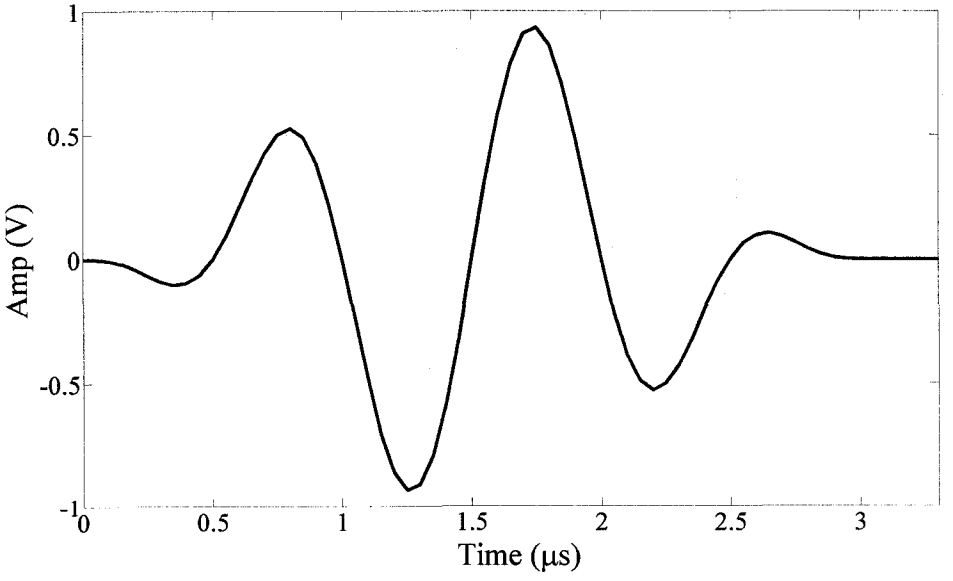

Figure 4.12 Source signals: (a) real signal (Panametrics C548) and (b) simulated wavelet by Disperse.

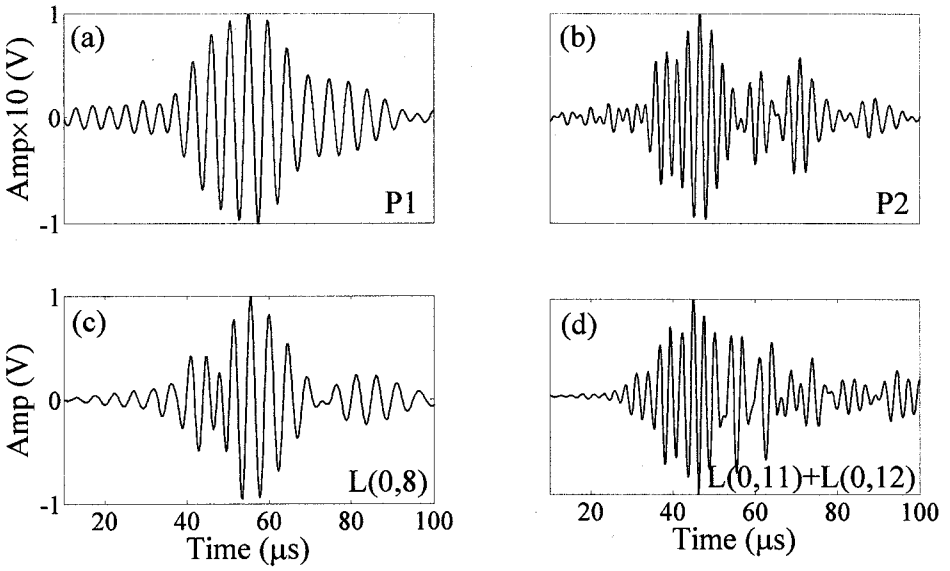

Figure 4.13 The time signatures of different guided wave modes measured at 53 mm offset: (a-b) experimental data after bandpass filtering; (c-d) simulation. The parameters used for simulation are given by the phantom model in Table 1. The real amplitudes can be obtained by multiplying the displayed amplitudes by the respective scaling factors: (a) 0.029, (b) 0.053, (c) 0.4, and (d) 0.72. P1 and P2 refer to the two strongest clusters in Figure 4.10.

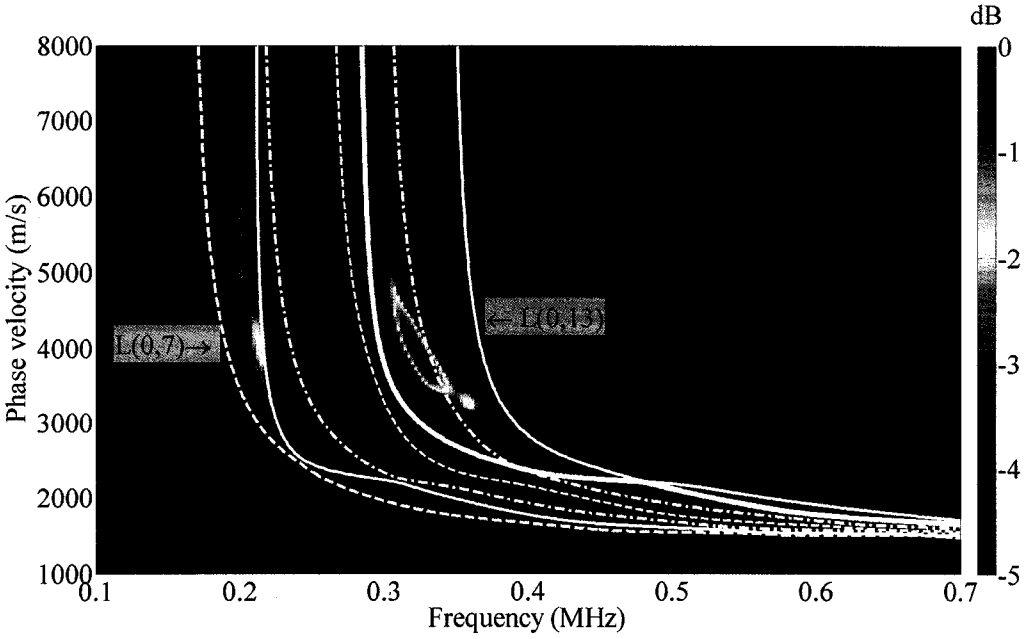

Figure 4.14 Simulated data: dispersion diagram superimposed by the theoretical dispersion curves. The parameters of the phantom model used are given in Table 4.2.

(a)

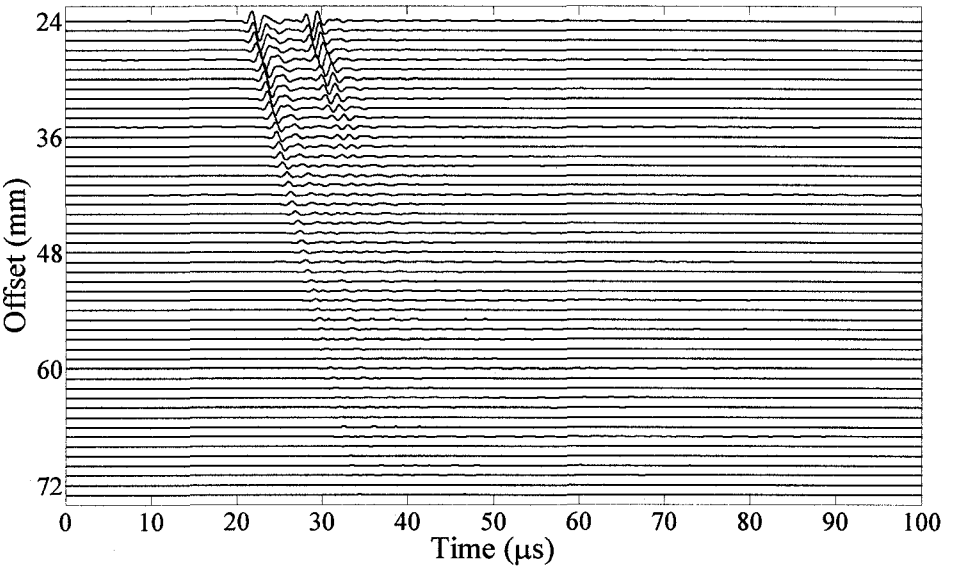

(b)

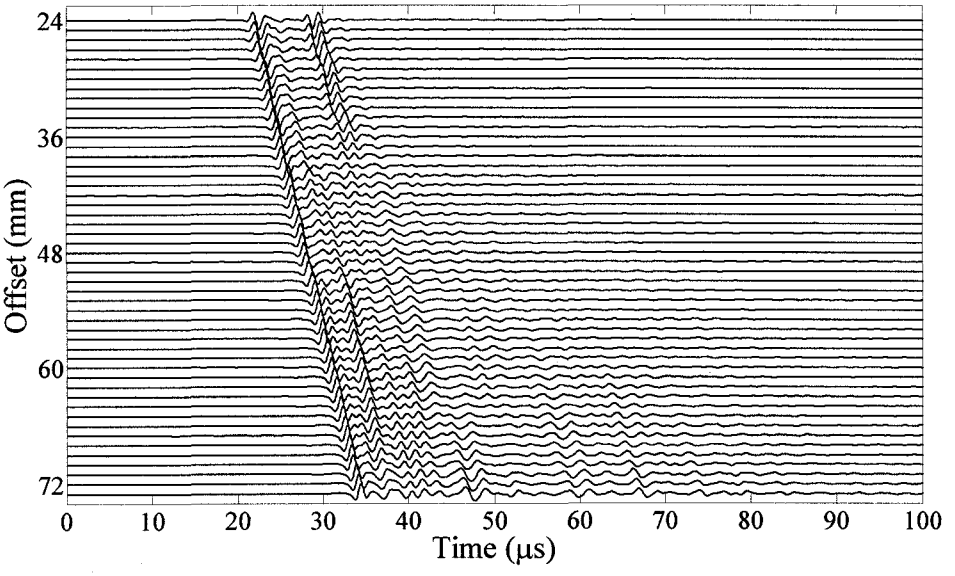

Figure 4.15 Echogram of the bovine tibia data: (a) original data without normalized; (b) self normalized data.

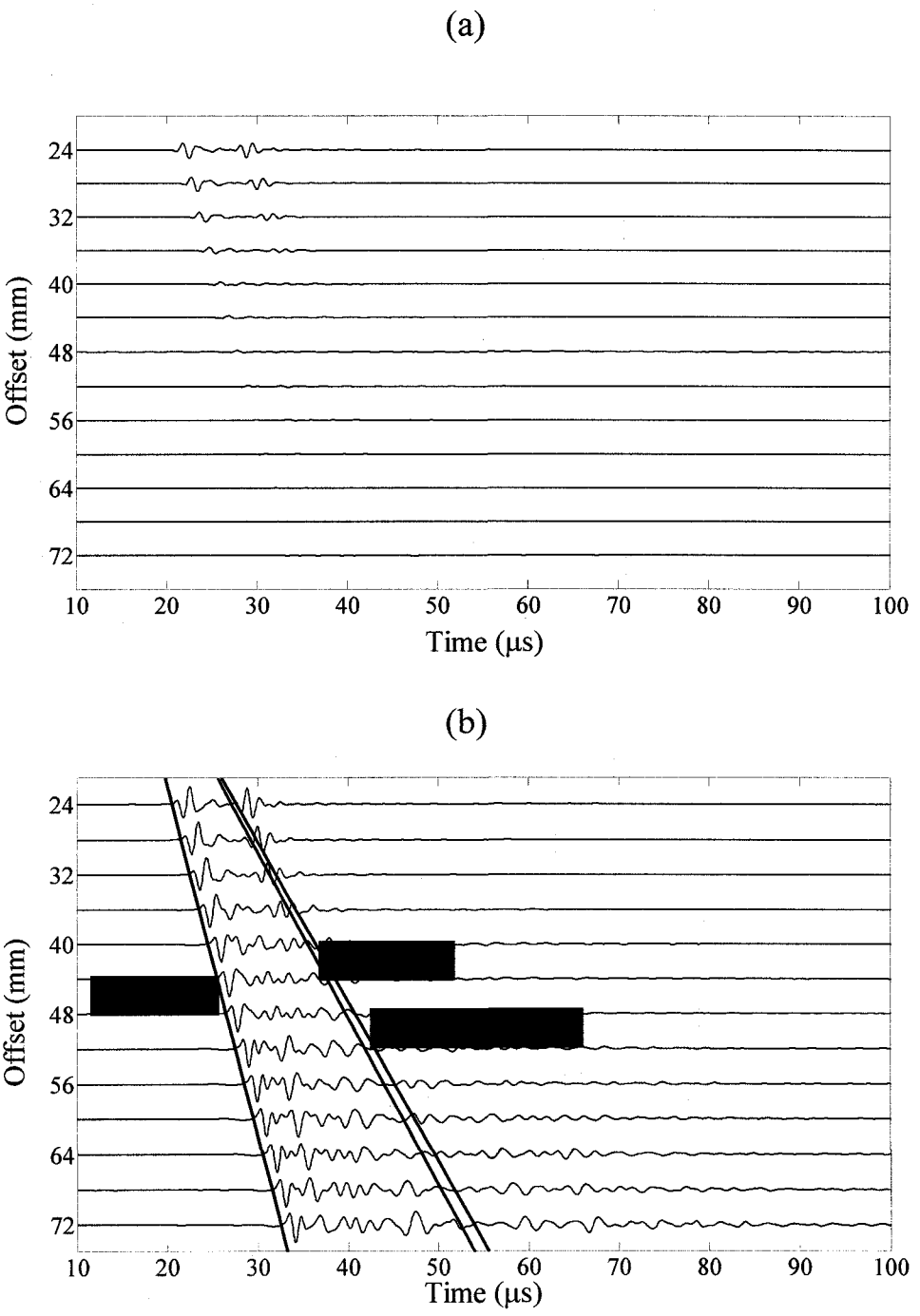

Figure 4.16 Echogram of measurements of bovine tibia with a spacing interval of 4 mm: (a) real signals; (b) self-normalized signals. The theoretical arrival time of the bulk compressional wave, bulk shear wave and Rayleigh wave are superimposed.

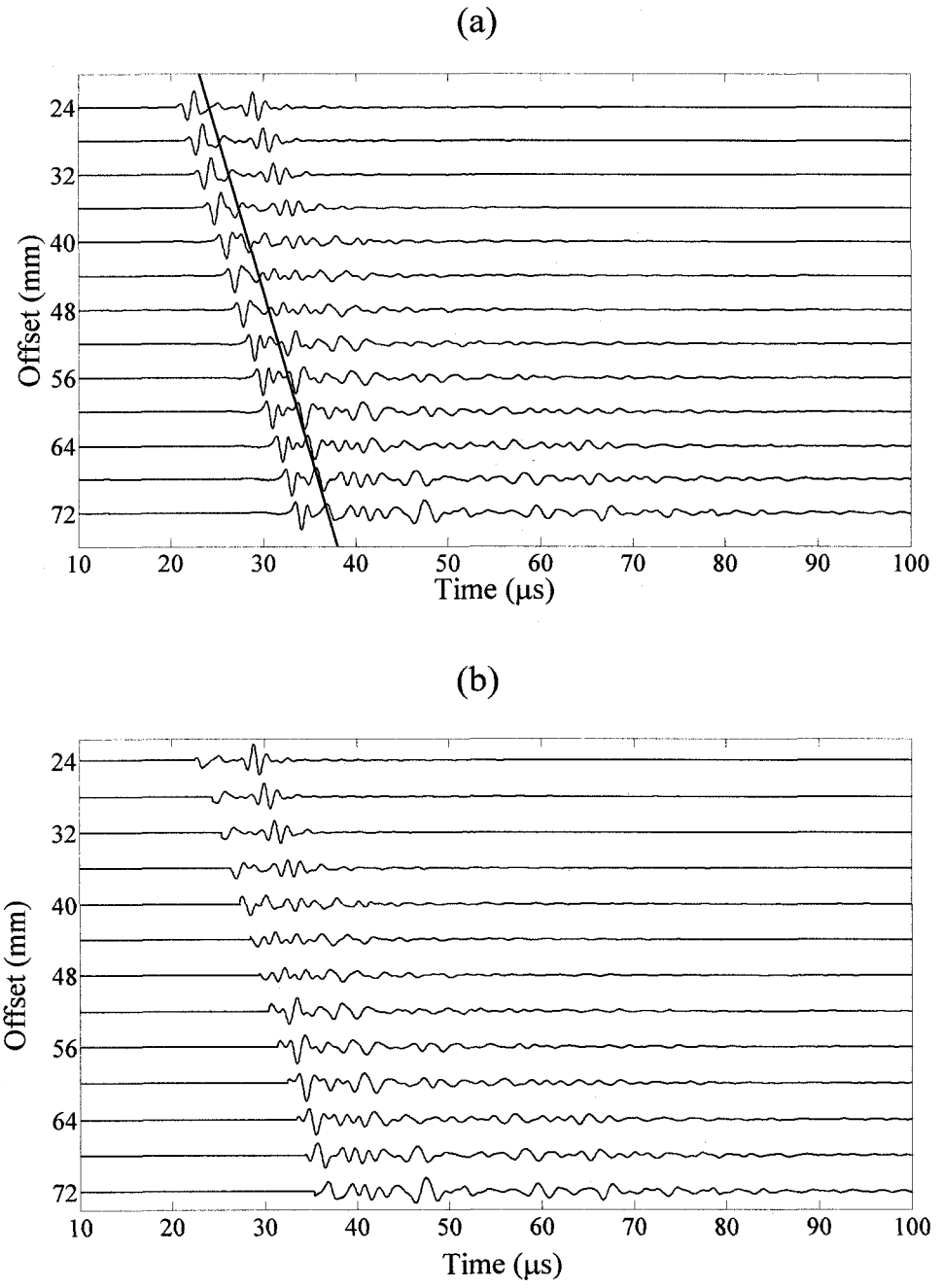

Figure 4.17 Echogram of the bovine tibia data: (a) before muting. The red line indicates the cut off of the muting window; (b) after muting.

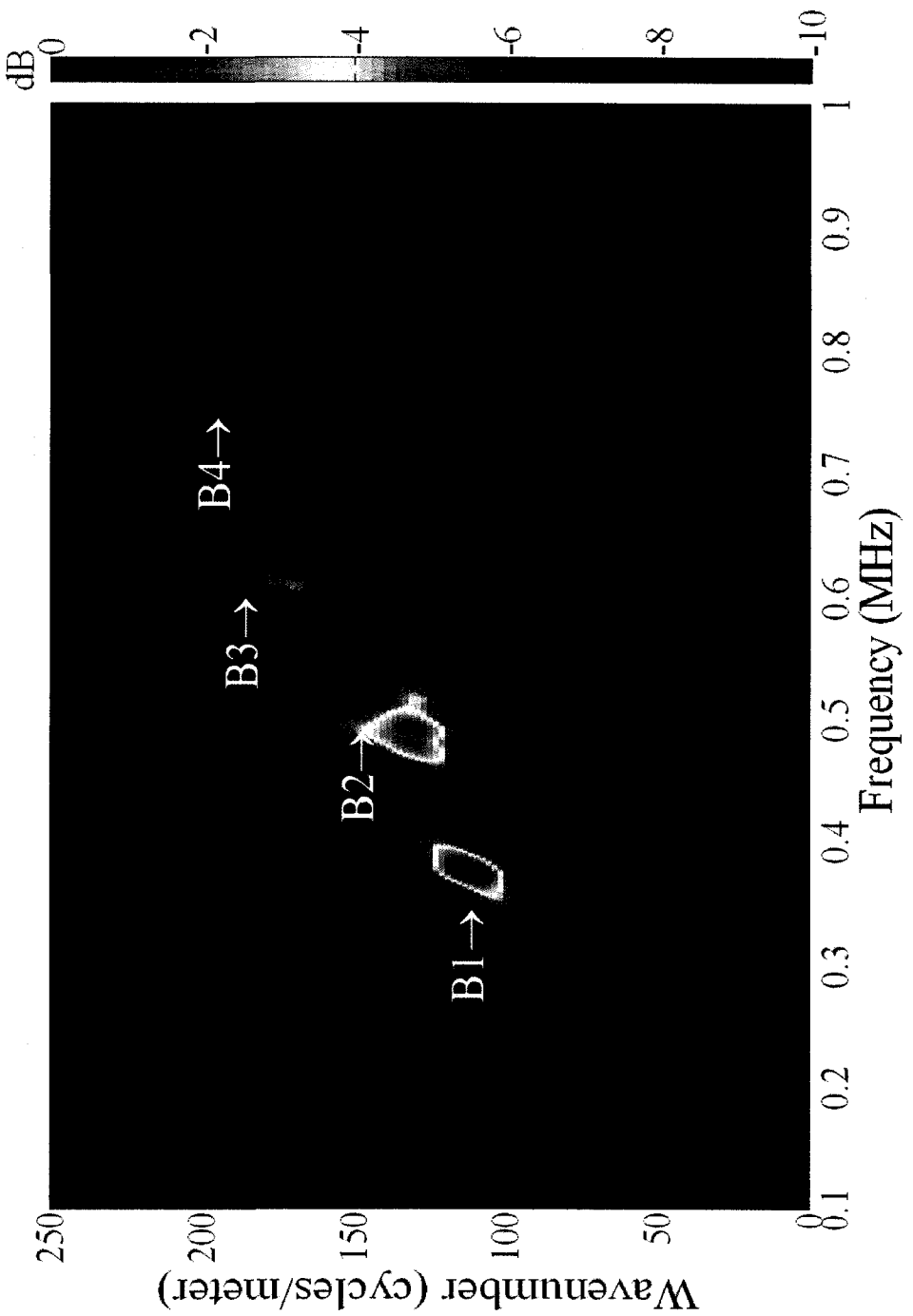

Figure 4.18 The 2-D periodogram of bovine tibia.

(a)

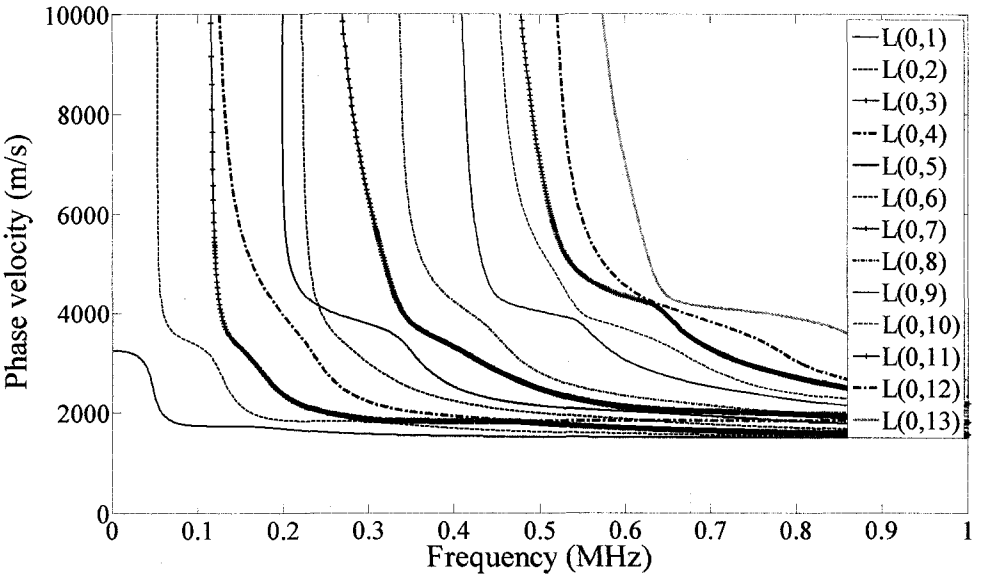

(b)

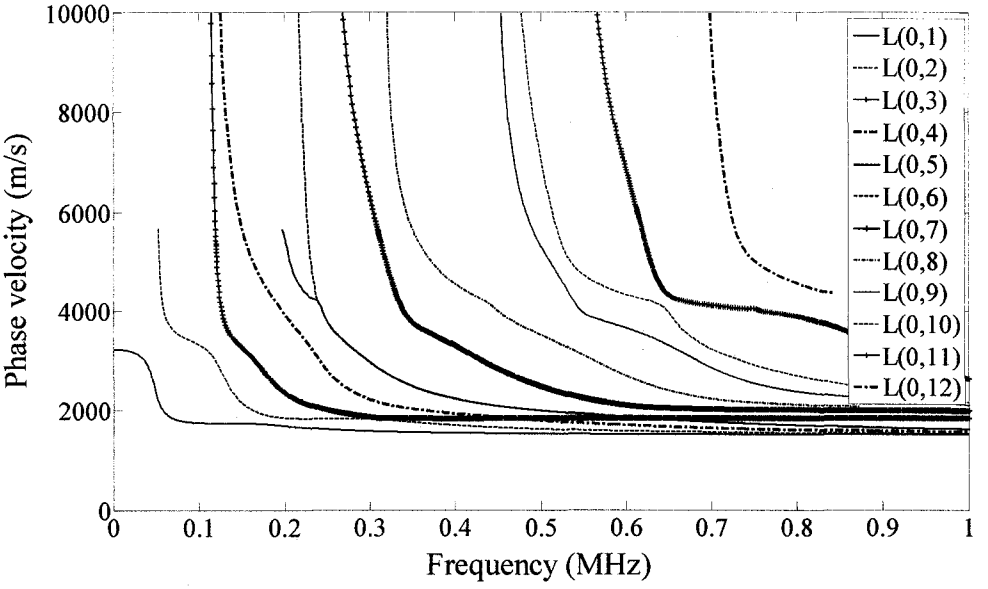

Figure 4.19 Theoretical dispersion curves of longitudinal guided waves mode in bovine tibia. The parameters used are given in Table 4.1: (a) without attenuation; (b) with attenuation.

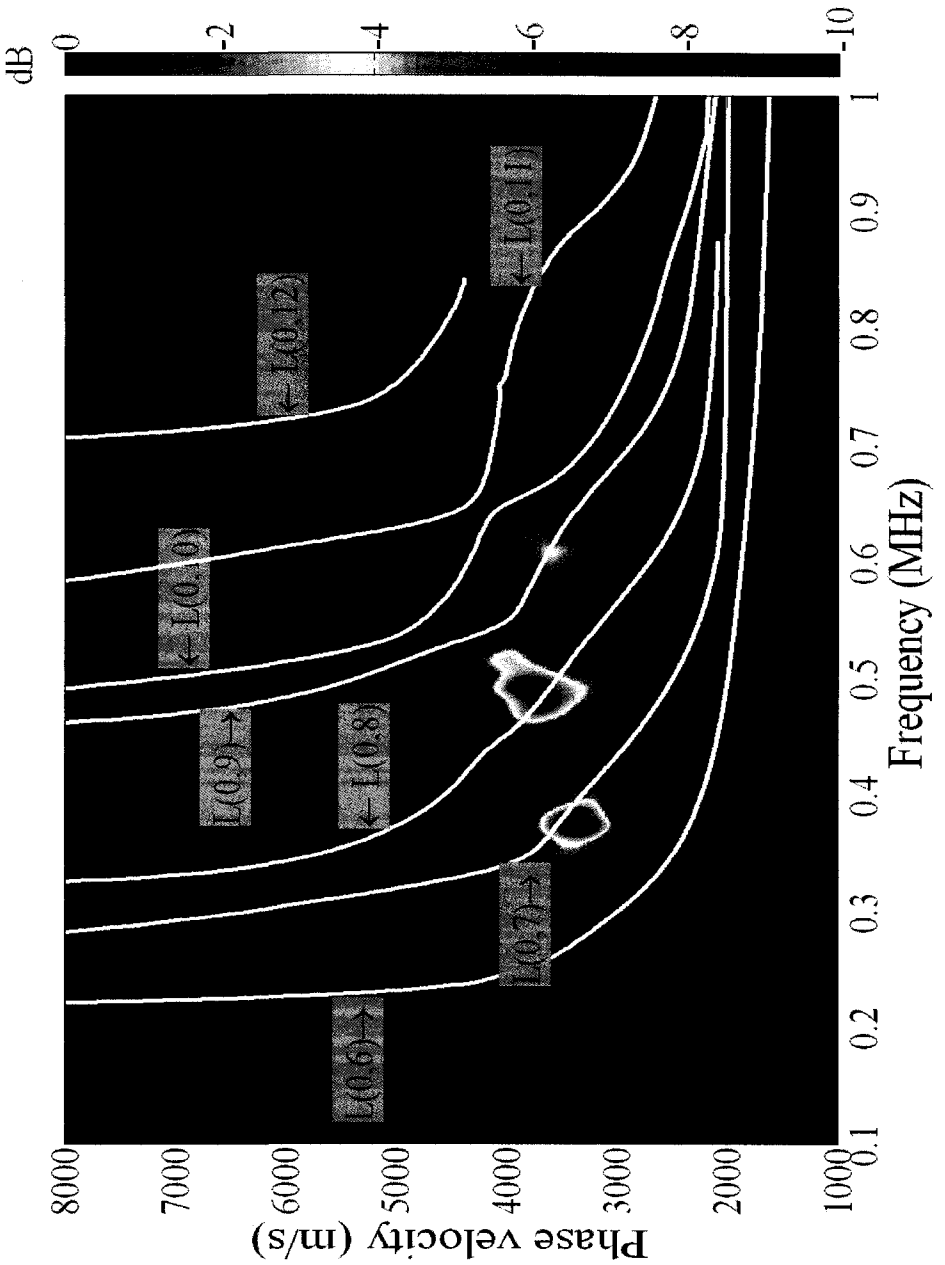

Figure 4.20 The dispersion diagram of bovine tibia superimposed by the theoretical dispersion curves. The parameters of the bone model used are given in Table 4.1.

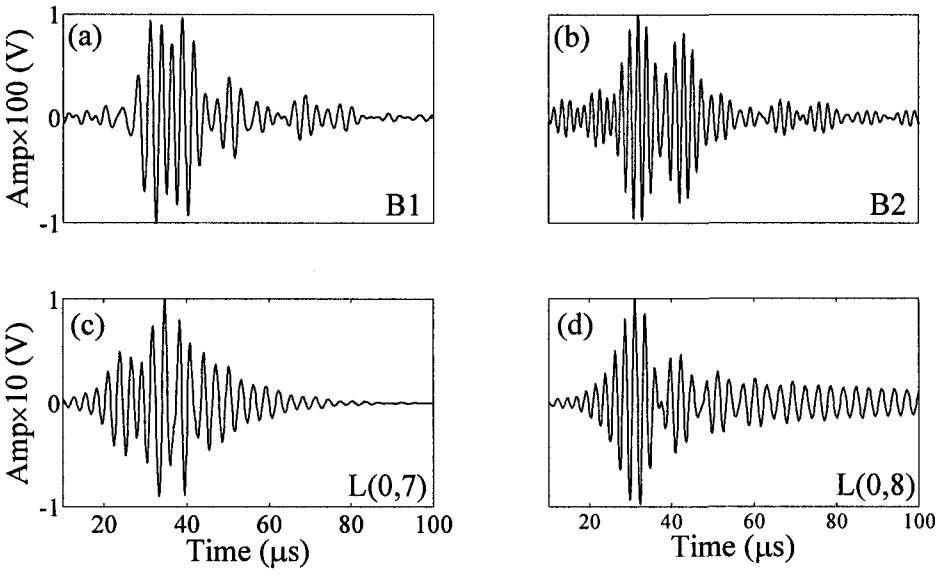

Figure 4.21 The time signatures of different guided wave modes measured at 53 mm offset: (a-b) experimental data after bandpass filtering; (c-d) simulation. The parameters used for simulation are given by the bone model in Table 1. The real amplitudes can be obtained by multiplying the displayed amplitudes by the respective scaling factors: (a) 0.01, (b) 0.0048, (c) 0.14, and (d) 0.08. B1 and B2 refer to the two strongest clusters in Fig. 4.19.

Chapter 5

Conclusions and Some Comments on Future Direction

This thesis aims to demonstrate the ultrasonic guided wave propagation in bone by applying a fluid-filled cylinder model. We acquired ultrasound data for cylindrical phantom and bovine tibia using an axial transmission technique. We computed the spectral 2-D periodogram and dispersion diagrams. Both data sets displayed well-separated and strong energy clusters in frequency. Based on a liquid-filled cylindrical tube model, we calculated guided wave dispersion curves to aid the interpretation and identification of guided waves. In both cases, at least two strong energy clusters were identified to be high-order longitudinal guided wave modes. We isolated each cluster and studied the time history of the signals. The time responses of the clusters were well described by dispersive wave trains, which are characteristic of guided wave propagation. Theoretical time modal responses were calculated and were in agreement with the experimental results.

In conclusion, it has been demonstrated the strong presence of high order longitudinal guided wave energies in axial transmission of ultrasound through bovine tibia. Methodology based on guided wave properties has potential to hold promise to assess the cortical properties relevant to osteoporosis.

Research of guided waves in bones is still in its infancy. As shown in some of the data, both bulk and guided waves coexist. Both types of waves carry very useful and independent information. Since we were interested in guided wave analysis, we attempted to remove the influence of bulk waves by muting the few microseconds of the data. We have placed a rectangular window in the echograms to mute the first arriving bulk waves. However, this is not an appropriate way to separate bulk waves and guided waves. There is still some coherent bulk wave energy coming around the

same time as guided waves. The future study of ultrasound wave propagation in bone relies heavily on signal processing techniques to separate different wave types and extract meaning ultrasonic parameters.

Bibliography

Achenbach, J.D., *Wave propagation in elastic solids*. American Elsevier Publishing Company, INC., New York, 1975.

Aki, K. and Richards, P. G., *Quantitative seismology theory and methods*. W. H. FREEMAN AND COMPANY, San Francisco, 1980.

Anton, H., *Elementary Linear Algebra* 3rd edition. John Wiley & Sons Inc., New York, 1981.

Ashman, R. B., Corin, J. D. and Turner, C. H., *Elastic properties of cancellous bone: Measurement by an ultrasonic technique*. J. Biomech., vol 20, pp. 979-986, 1987.

Ashman, R. B. and Rho, J. Y., *Elastic modulus of trabecular bone material*. J. Biomech., vol. 21, pp. 177-181, 1988.

Behari, J. and Singh, S., *Ultrasound propagation in 'in vivo' bone*. Ultrasonics, vol. 19, pp. 87-90, 1981.

Bone Anatomy Review. Harvard Medical School Radiology Core Clerkship Review Module. available at http://brighamrad.harvard.edu/education/. Accessed: July, 2007.

Bonnick, S. L. and Lewis, L. A., *Bone densitometry for technologists*. New Jersey: Humana Press, 2002.

Bossy, E., Talmant, M. and Laugier, P., *Effect of bone cortical thickness on velocity measurements using ultrasonic axial transmission: A 2D simulation study*. J. Acoust. Soc. Am., vol. 112, no. 1, pp. 297-307, 2002.

Brown, J. P. and Josse, R. G., *2002 clinical practice guidelines for the diagnosis and management of osteoporosis in Canada*. CMAJ, vol. 167, no. 10, pp. s1-s34, Nov. 2002.

Camus, E., Talmant, M., Berger, G. and Laugier, P., *Analysis of the axial transmission technique for the assessment of skeletal status*. J. Acoust. Soc. Am., vol. 108, no. 6, pp. 3058-3065, 2000.

Chaffaï, S., Padilla, F., Berger, G., and Laugier. P., *In vitro measurement of the frequency-dependent attenuation in cancellous bone between 0.2 and 2 MHz*. J. Acoust. Soc. Am., vol. 108, no. 3, pp. 1281-1289, 2000.

Churchill, R. V. and Brown, J. W., *Fourier series and boundary value problems.* Mcgraw-Hill Book Company, New York, 1978.

Cooper, R. M. and Naghdi, P. M., Propagation of nonaxially symmetric waves in elastic cylindrical shells. J. Acoust. Soc. Am., vol. 29, no. 12, pp. 1365-1373, 1957.

Cooper, D. M. L., Thomas, C. D. L., Clement, J. G. and Hallgrimsson, B., *Three dimensional micro-CT imaging of BMU-Related resorption spaces in human cortical bone.* Anatomical Record Part A, 288A:806-816, 2006.

Dodd, S. P., Cunningham, J. L., Miles, A. W., Gheduzzi, S. and Humphrey, V. F., *Ultrasonic propagation in cortical bone mimics.* Phys. Med. Biol., vol. 51, pp. 4635-4647, 2006.

Droin, P., Berger, G. and Laugier, P., *Velocity dispersion of acoustic waves in cancellous bone.* IEEE Trans. Ultrason., Ferroelect., Freq. Contr., vol. 45, pp. 581-592, May 1998.

Elvira-Segura, L., *Acoustic wave dispersion in a cylindrical elastic tube filled with a viscous liquid.* Ultrasonics, vol. 37, pp. 537-547, 2000.

Fellah, Z. E. A. and Chapelon, J. Y., *Ultrasonic wave propagation in human cancellous bone: application of Biot theory.* J. Acoust. Soc. Am., vol. 116, no. 1, pp. 61-73, 2004.

Glüer, C. C., Quantitative ultrasound-It is time to focus research efforts. Bone, vol. 40, pp. 9-13, 2007.

Graff, K.F., *Wave motion in elastic solids.* Ohio State University Press, Columbus, OH, 1975.

Griffiths, D. J., *Introduction to electrodynamics, 3rd.* Prentice-Hall, Inc, Upper Saddle River, New Jersey, 1999.

Hsu, K. and Esmersoy, C., Parametric estimation of phase and group slownesses from sonic logging waveforms. Geophysics, vol. 57, no. 8, pp. 978-985, 1992.

International Osteoporosis Foundation. available at http://www.iofbonehealth.org/. Accessed: July, 2007.

Jenkins, G. M. and Watts, D. G., *Spectral analysis and its applications.* Holden-Day, San Francisco, 1968.

Ji, Q., *A physical model for broadband ultrasonic studies of cancellous bone*, Ph.D. thesis. University of Alberta, April. 1998.

Kay, S. M. and Marple, S. L. Jr., *Spectrum analysis- A modern perspective*. Proc., Inst. Electr. Electron. Eng., vol. 69, pp. 1380-1419, 1981.

Kaye, G. W. C. and Laby, T. H., *Table of physical and chemical constants. 16th ed.*, Longman, Essex, 1995.

Kumar, R., *Dispersion of axially symmetric waves in empty and fluid-filled cylindrical shells*. Acustica, vol. 27, pp. 317-329, 1972.
Kumar, R., *Flexural vibrations of fluid-filled circular cylindrical shells*. Acustica, vol. 24, pp. 137-146, 1971.

Kundu, T., *Ultrasonic nondestructive evaluation*. Boca Raton, CRC Press, 2004.

Kurkjian, A. L., *Numerical computation of individual far-field arrivals excited by an acoustic source in a borehole*. Geophysics, vol. 50, no. 5, pp. 852-866, 1985.

Lang, S. W., Kurkjian, A. L., McClellan, J. H., Morris, C. F. and Parks, T. W., *Estimating slowness dispersion from arrays of sonic logging waveforms*. Geophysics, vol. 52, no. 4, pp. 530-544, 1987.

Langton, C.M., Palmer, S.B., and Porter, R.W., *The measurement of broadband ultrasonic attenuation in cancellous bone*. Eng. Med., vol. 13, no. 2, pp.89-91, 1984.

Laster, S., Foreman, J. and Linville, F., *Theoretical investigation of modal seismograms for a layer over a half-space*. Geophysics, vol. 30, pp. 571-596, 1965.

Laugier, P., *Quantitative ultrasound of bone: looking ahead*. Joint Bone Spine, vol. 73, pp. 125-128, 2006.

Lee, K. I., and Yoon, S. W., *Feasibility of bone assessment with leaky lamb wave in bone phantoms and a bovine tibia*. J. Acoust. Soc. Am., vol. 115, no. 6, pp. 3210-3217, 2004.

Lefebvre, F., Deblock, Y., Campistron, P., Ahite, D. and Fabre, J. J., *Development of a new ultrasonic technique for bone and biomaterials in vitro characterization*. J. Biomed. Mater. Res. (Appl. Biomater.), vol. 63, pp. 441-446, 2002.

Lim, J. S., *Two-dimensional signal and image processing*. Prentice Hall, New Jersey, 1990.

Lorrain, P. and Corson, D., *Electromagnetic fields and waves*. W. H. FREEMAN AND COMPANY, San Francisco, 1970.

Lowe, M. J. S., *Matrix techniques for modeling ultrasonic waves in multilayered media*. IEEE Trans. Ultrason., Ferroelect., Freq. Contr., vol. 42, no.4, pp. 525-542, 1995.

Lowet, G. and Van der Perre, G. V., *Ultrasound velocity measurement in long bones: Measurement method and simulation of ultrasound wave propagation*. J. Biomech., vol. 29, no. 10, pp. 1255-1262, 1996.

McClellan, J. H., *Two-dimensional spectrum analysis in sonic logging*. Proc. Internat. Conf. on Acoustic, Speech and Signal Proc. Tokyo, pp. 3105-3111, 1986.

McLachlan, N. W., *Bessel Functions for Engineers*. Clarendon Press, Oxford, 1934.

Moilanen, P., Kilappa, V., Nicholson, P. H. F., Timonen, J. and Cheng, S., *Thickness sensitivity of ultrasound velocity in long bone phantoms*. Ultrasound in Med. &Biol., vol. 30, no. 11, 1517-1521, 2004.

Moilanen, P., Nicholson, P. H. F., Kilappa, V., Cheng, S. and Timonen, J., *Assessment of the cortical bone thickness using ultrasonic guided waves: modeling and in vitro study*. Ultrasound in Med. & Biol., vol. 33, no. 5, pp. 254-262, 2007.

Moilanen, P., Nicholson, P. H. F., Kilappa, V., Cheng, S. and Timonen, J., *Measuring guided wave in long bone- Modeling and experiments in free and immersed plates*. Ultrasound in Med. & Biol., vol. 32, no. 5, pp. 709- 719, 2006.

Moon, P. and Spencer, D. E., *Field Theory Handbook*. Springer-Verlag, Berlin, 1961.

Naidu, P. S., *Modern spectrum analysis of time series*. CRC Press, New York, 1995.

Nayfeh, A. H. and Chimenti, D. E., *Ultrasonic leaky waves in the presence of a thin layer*. J. Appl. Phys., vol. 52, no. 8, pp. 4985-4994, 1981.

Nicholson, P. H. F., Lowet, G., Langton, C. M., Dequeke, J. R. and Van der Perre, G. V., *A comparison of time-domain and frequency-domain approaches to ultrasonic velocity measurement in trabecular bone*. Phys. Med. Biol., vol. 41, pp. 2421–2435, 1996.

Nicholson, P. H. F., Moilanen, P., Kärkkäinen, T. K., Timonen, J. and Cheng, S., *Guided ultrasonic waves in long bones: modeling, experiment and in vivo application*. Physiol. Meas., vol. 23, pp. 755-768, 2002.

Njeh, C. F., Hans, D., Fuerst, T., Glüer, C. C., and Genant, H. K., *Quantitative ultrasound: Assessment of osteoporosis and bone status*. London: Martin Dunitz, 1999.

Oppenheim, A. V., Schafer, R. W. and Buck, J. R., *Discrete-time signal processing*. Prentice Hall, Upper Saddle River, New Jersey, 1999.

Osteoporosis Canada: available at http://www.osteoporosis.ca/english/. Accessed: July, 2007.

Osteoporosis Prevention, Diagnosis, and Therapy. NIH Consensus Statement. vol. 3, no.1, pp. 1-36, March, 2000.

Pavlakovic, B. and Lowe, M., *Disperse user's manual, version 2.0.11*. Imperial College, London, June, 2001.

Peterson, E. W., *Acoustic wave propagation along a fluid-filled cylinder*. J. Appl. Phys., vol. 45, no. 8, pp. 3340-3350, 1974.

Priestley, M. B., *Spectral analysis and time series*. Academic Press, New York, 1981.

Protopappas, V. C., Fotiadis, D. I., and Malizos, K. N., *Guided ultrasound wave propagation in intact and healing long bones*. Ultrasound in Med. & Biol., vol. 32, no.5, pp. 693-708, 2006.

Randall, C. J. and Stanke, C. J., *Mathematical model for internal ultrasonic inspection of cylindrically layered structures*. J. Acoust. Soc. Am., vol. 83, no. 4, pp. 1295-1305, 1988.

Rho, J. Y., *An ultrasonic method for measuring the elastic properties of human tibial cortical and cancellous bone*. Ultrasonics, vol. 34, no. 8, pp. 777-783, 1996.

Rose, J. L., *Ultrasonic waves in solid media*. Cambridge, Cambridge University Press, 1999.

Saulgozis, J., Pontaga, I., Lowet, G. and Van der Perre, G. V., *The effect of fracture and fracture fixation on ultrasonic velocity and attenuation*. Physiol. Meas. vol. 17, pp. 201-211, 1996.

Sievänen, H., Kannus, P., Nieminen, V., Heinonen, A., Oja, P. and Vuori, I., *Estimation of various mechanical characteristics of human bones during dual energy x-ray absorptiometry: methodology and precision*, Bone, vol. 18, no. 1, pp.17-27, Supplement Jan. 1996.

Siffert, R. S. and Kaufman, J. J., *Ultrasonic bone assessment: "The time has come"*. Bone, vol. 40, pp. 5-8, 2007.

Silk, M. G. and Bainton, K. F., *The propagation in metal tubing of ultrasonic wave modes equivalent to Lamb wave*. Ultrasonics, vol. 17, no. 1, pp. 11-19, 1979.

Sinha, B. K., Plona, T. J., Kostek, S. and Chang, S. K., *Axisymmetric wave propagation in fluid-filled cylindrical shells. I: Theory*. J. Acoust. Soc. Am., vol. 92. no. 2. pp. 1132-1143, 1992.

Speller, R. D., Royle, G. J. and Horrocks, J. A., *Instrumentation and techniques in bone density measurement*. J. Phys. E: Sci. Instrum., vol. 22, pp. 202-214, 1989.

Stearns, S. D. and Hush, D. R., *Digital signal analysis*. Prentice Hall, Englewood Cliffs, New Jersey, 1990.

Strelitzki, R., Evans, J. A., *On the measurement of the velocity of ultrasound in the os calcis using short pulses*. Eur. J. Ultrasound, vol. 4, pp. 205-213, 1996.

Ta, D., Huang, K., Wang, W., Wang, Y. and Le, L. H., *Identification and analysis of multimode guided wave in tibia cortical bone*. Ultrasonics, vol. 44, pp. e279-e284, 2006.

Tatarinov, A., Sarvazya, N. and Sarvazyan, A., *Use of multiple acoustic wave modes for assessment of long bones: Model study*. Ultrasonics, vol. 43, pp. 672-680, 2005.

Thesiman, H. and Pfander, F., *Uber diedurchlassigkeit des knochens fur ultraschall*. Strahlentherapie, vol. 80, pp. 607-610, 1949.

Tortora, G. J. and Grabowski, S. R., *Principles of anatomy and physiology*. Harper Collins Colleger Publishers, New York, 1992.

Tsang, L. and Rader, D., *Numerical evaluation of the transient acoustic waveform due to a point source in a fluid-filled borehole*. Geophysics, vol. 44, no. 10, pp. 1706-1720, 1979.

Viktorov, I. A., *Rayleigh and Lamb Waves-Physical theory and applications*. New York, Plenum Press, 1967.

Udías, A., *Principles of seismology*. Cambridge University Press, Cambridge, United Kingdom, 1999.

Wear, K. A., *A stratified model to predict dispersion in trabecular bone*, IEEE Trans. Ultrason., Ferroelect., Freq. Contr., vol. 48, no. 4, pp. 1079-1083, 2001.

Wear, K. A., *Measurements of phase velocity and group velocity in human calcaneus*, Ultrasound Med. Biol., vol. 26, no. 4, pp. 641-646, 2001.

Wear, K. A., *Ultrasound attenuation in human calcaneus from 0.2 to 1.7 MHz*, IEEE Trans. Ultrason., Ferroelect., Freq. Contr., vol. 48, no. 2, pp. 602-608, 2001.

Wu, J. and Cubberley, F., *Measurement of velocity and attenuation of shear waves in bovine compact bone using ultrasonic spectroscopy*. Ultrasound in Med. & Biol., vol. 23, no. 1, pp. 129-134, 1997.

Yoon, H. S. and Katz, L., *Ultrasonic wave propagation in human cortical bone-II: measurement of elastic properties and microhardness*. J. Biomech., vol. 9, pp. 459-462, 1976.

Yu, L., *Numerical simulation of ultrasonic wave propagation in a stratified cancellous bone model*, M.Sc. thesis. University of Alberta, Feb. 2005.

Zemanek, J., *An experimental and theoretical investigation of elastic wave propagation in cylinder*. J. Acoust. Soc. Am., vol. 51, no. 1, pp. 265-283, 1972.

Zheng, R., Le, L. H., Sacchi, M. D., Ta, D., and Lou, E., *Spectral ratio method to estimate broadband ultrasound attenuation of cortical bones in vitro using multiple reflections*. Phys. Med. Biol., vol. 52, pp. 5855-5869, 2007.

Appendix A

Some Fundamentals Relevant to Ultrasound Wave Propagation

A.1 Stress and strain

Stress is defined as the force exerted on a surface element. When a stress is applied to a body, it will deform. When the force is perpendicular to the surface element, it is a normal stress. When the force is parallel or tangential to the surface element, it is a shear stress. Forces applied to solid will cause its deformation. Strain is defined as the relative change in volume, length or shape of a body. Correspondingly, there are normal strain and shearing strain. Strain can be expressed by a displacement function $\vec{f}$ of a particle

$$\vec{f} = u(x,y,z,t)\hat{\mathbf{i}} + v(x,y,z,t)\hat{\mathbf{j}} + w(x,y,z,t)\hat{\mathbf{k}} \tag{A.1}$$

where t is the time and $u(x,y,z,t)$, $v(x,y,z,t)$ and $w(x,y,z,t)$ are the displacement components in the direction of x-, y- and z-axis respectively with the corresponding unit vectors being $\hat{\mathbf{i}}$, $\hat{\mathbf{j}}$ and $\hat{\mathbf{k}}$ respectively. In terms of the displacement components, the normal strains are defined as

$$\begin{aligned} \varepsilon_{xx} &= \frac{\partial u}{\partial x} \quad , \\ \varepsilon_{yy} &= \frac{\partial v}{\partial y} \quad , \\ \varepsilon_{zz} &= \frac{\partial w}{\partial z} \quad , \end{aligned} \tag{A.2}$$

and the shear strains are

$$\begin{aligned}
\varepsilon_{xy} &= \varepsilon_{yx} = \frac{\partial v}{\partial x} + \frac{\partial u}{\partial y} \quad , \\
\varepsilon_{yz} &= \varepsilon_{zy} = \frac{\partial w}{\partial y} + \frac{\partial v}{\partial z} \quad , \\
\varepsilon_{zx} &= \varepsilon_{xz} = \frac{\partial u}{\partial z} + \frac{\partial w}{\partial x} \quad .
\end{aligned} \tag{A.3}$$

Let T_{ij} $(i, j = x, y, z)$ be the stress vector acting on a surface of a cubic volume element (Figure A.1). The subscript i denotes the normal to the surface on which the force acts and j denotes the components of the force. Using Hooke's law for an isotropic solid, the stress is linearly proportional to the strain as follow

$$\begin{aligned}
T_{xx} &= \lambda\left(\varepsilon_{xx} + \varepsilon_{yy} + \varepsilon_{zz}\right) + 2\mu\varepsilon_{xx} \quad , \\
T_{yy} &= \lambda\left(\varepsilon_{xx} + \varepsilon_{yy} + \varepsilon_{zz}\right) + 2\mu\varepsilon_{yy} \quad , \\
T_{zz} &= \lambda\left(\varepsilon_{xx} + \varepsilon_{yy} + \varepsilon_{zz}\right) + 2\mu\varepsilon_{zz} \quad , \\
T_{yz} &= T_{zy} = \mu\varepsilon_{yz} \quad , \\
T_{zx} &= T_{xz} = \mu\varepsilon_{zx} \quad , \\
T_{xy} &= T_{yx} = \mu\varepsilon_{xy} \quad .
\end{aligned} \tag{A.4}$$

where λ and μ are known as the *Lamé's constants*. The constant μ is also known as the shear modulus.

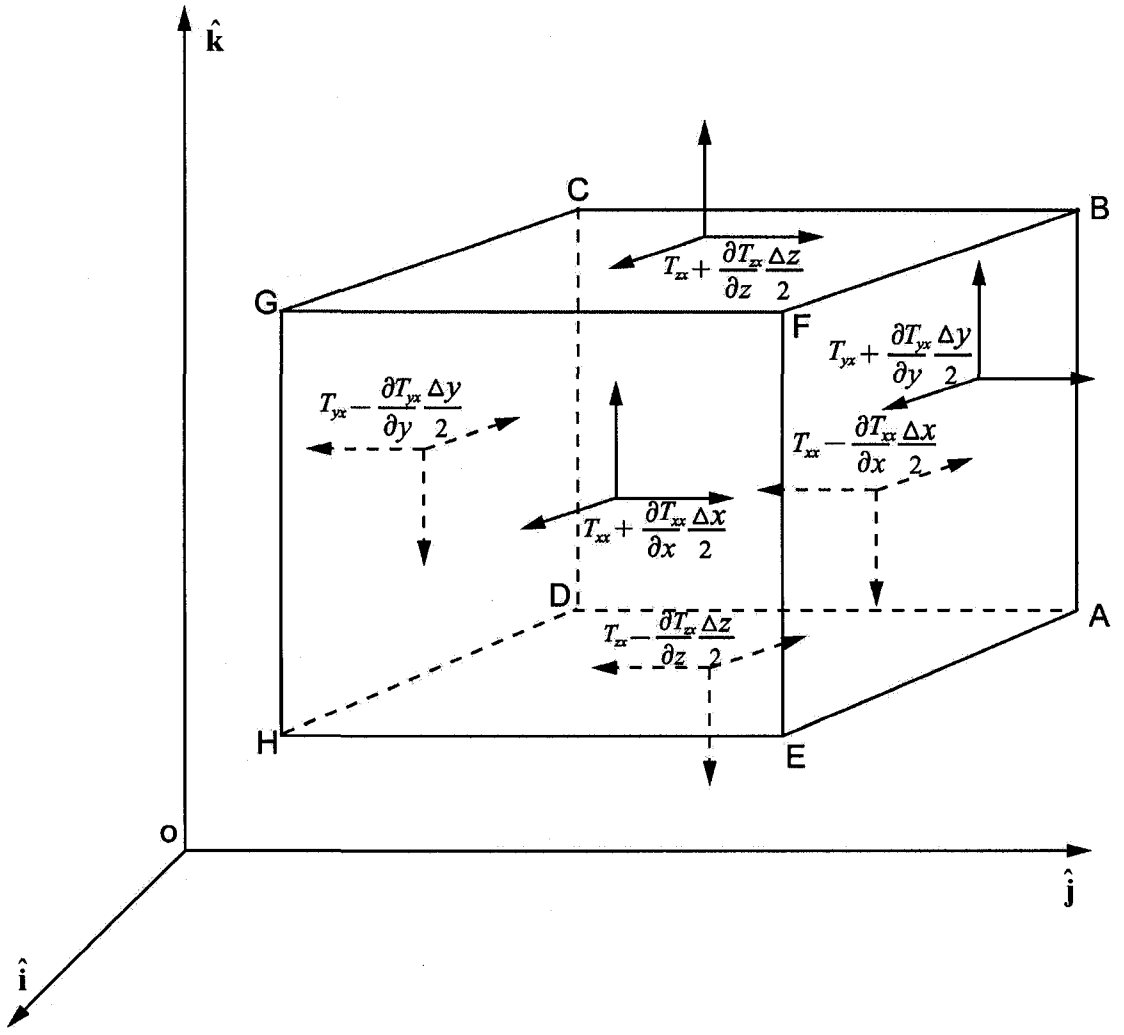

Figure A.1 Stress components acting on the surface of a cubic volume element.

A.2 Equations of motion

Consider an infinitesimal cubic volume centering a particle M at location (x, y, z) (Figure A.1). Along the $\hat{\mathbf{i}}$ direction, the normal stresses acting on the two surfaces contribute to the net normal stress acting on the particle:

$$\left[T_{xx}\left(x+\Delta x\right)-T_{xx}\right]\Delta y\Delta z \quad . \tag{A.5}$$

By Taylor expansion,

$$T_{xx}(x+\Delta x) = T_{xx} + \frac{\partial T_{xx}}{\partial x}\Delta x + O(\Delta x^2) \quad . \tag{A.6}$$

Ignoring the higher order terms, equation (A.5) can be written as

$$\left[T_{xx}(x+\Delta x) - T_{xx}\right]\Delta y\Delta z = \frac{\partial T_{xx}}{\partial x}\Delta x\Delta y\Delta z \quad . \tag{A.7}$$

Similarly, for the shear stresses, we have

$$\left[T_{yx}(y+\Delta y) - T_{yx}\right]\Delta x\Delta z = \frac{\partial T_{yx}}{\partial y}\Delta x\Delta y\Delta z \tag{A.8}$$

and

$$\left[T_{zx}(y+\Delta y) - T_{zx}\right]\Delta x\Delta z = \frac{\partial T_{zx}}{\partial z}\Delta x\Delta y\Delta z \quad . \tag{A.9}$$

Therefore, the total stress acting on the particle M along the $\hat{\mathbf{i}}$ direction is

$$\left(\frac{\partial T_{xx}}{\partial x} + \frac{\partial T_{yx}}{\partial y} + \frac{\partial T_{zx}}{\partial z}\right)\Delta x\Delta y\Delta z \quad . \tag{A.10}$$

According to the Newton's second law of motion, the net force equals the mass times the acceleration, i.e.,

$$\rho\frac{\partial^2 u}{\partial t^2} = \frac{\partial T_{xx}}{\partial x} + \frac{\partial T_{yx}}{\partial y} + \frac{\partial T_{zx}}{\partial z} \tag{A.11}$$

where ρ is the density of the medium. Similarly, the equations of motion along $\hat{\mathbf{j}}$ and $\hat{\mathbf{k}}$ directions are respectively

$$\rho\frac{\partial^2 v}{\partial t^2} = \frac{\partial T_{xy}}{\partial x} + \frac{\partial T_{yy}}{\partial y} + \frac{\partial T_{yz}}{\partial z} \tag{A.12}$$

and

$$\rho\frac{\partial^2 w}{\partial t^2} = \frac{\partial T_{xz}}{\partial x} + \frac{\partial T_{yz}}{\partial y} + \frac{\partial T_{zz}}{\partial z} \quad . \tag{A.13}$$

Substituting (A.2) - (A.4) into (A.11), we have

$$\rho\frac{\partial^2 u}{\partial t^2}=\lambda\frac{\partial}{\partial x}\left(\frac{\partial u}{\partial x}+\frac{\partial v}{\partial y}+\frac{\partial w}{\partial z}\right)+2\mu\frac{\partial^2 u}{\partial x^2}+\mu\left(\frac{\partial^2 v}{\partial x\partial y}+\frac{\partial^2 u}{\partial y^2}\right)+\mu\left(\frac{\partial^2 u}{\partial z^2}+\frac{\partial^2 w}{\partial x\partial z}\right)$$
$$=\lambda\frac{\partial}{\partial x}(\frac{\partial u}{\partial x}+\frac{\partial v}{\partial y}+\frac{\partial w}{\partial z})+\mu\frac{\partial}{\partial x}(\frac{\partial u}{\partial x}+\frac{\partial v}{\partial y}+\frac{\partial w}{\partial z})+\mu(\frac{\partial^2 u}{\partial x^2}+\frac{\partial^2 u}{\partial y^2}+\frac{\partial^2 u}{\partial z^2}) \quad (A.14)$$
$$=(\lambda+\mu)\frac{\partial\theta}{\partial x}+\mu\nabla^2 u$$

where θ is the divergence

$$\theta=\nabla\cdot\vec{f}=\varepsilon_{xx}+\varepsilon_{yy}+\varepsilon_{zz}=\frac{\partial u}{\partial x}+\frac{\partial v}{\partial y}+\frac{\partial w}{\partial z} \quad (A.15)$$

and ∇^2 is the Laplacian operator

$$\nabla^2=\frac{\partial^2}{\partial x^2}+\frac{\partial^2}{\partial y^2}+\frac{\partial^2}{\partial z^2} \quad . \quad (A.16)$$

Similarly for the displacement components along the $\hat{\mathbf{j}}$ and $\hat{\mathbf{k}}$ directions,

$$\rho\frac{\partial^2 v}{\partial t^2}=(\lambda+\mu)\frac{\partial\theta}{\partial y}+\mu\nabla^2 v \quad (A.17)$$

and

$$\rho\frac{\partial^2 w}{\partial t^2}=(\lambda+\mu)\frac{\partial\theta}{\partial z}+\mu\nabla^2 w \quad . \quad (A.18)$$

In vectorial notion, equation (A.14), (A.17) and (A.18) can be summarized as

$$\rho\frac{\partial^2\vec{f}}{\partial t^2}=(\lambda+\mu)\nabla\left(\nabla\cdot\vec{f}\right)+\mu\nabla^2\vec{f} \quad . \quad (A.19)$$

Equation (A.19) is known as the wave equation.

A.3 Wave motion and particle polarization

Helmholtz's theorem (Griffiths, 1999) states that a continuous vector field $\vec{f}$ can be considered as a superposition of two vectors $\vec{f}_1$ and $\vec{f}_2$

$$\vec{f}=\vec{f}_1+\vec{f}_2 \quad (A.20)$$

subject to the conditions

$$\nabla \times \vec{f}_1 = 0 \text{ and } \nabla \cdot \vec{f}_2 = 0 \tag{A.21}$$

where $\vec{f}_1$ is curl-free and $\vec{f}_2$ is divergence-free.

A.3.1 Longitudinal wave

Consider a curl-free displacement field $\vec{f} = \vec{f}_1$ where $\nabla \times \vec{f}_1 = 0$. We have

$$\nabla \times \left(\nabla \times \vec{f}_1 \right) = \nabla \left(\nabla \cdot \vec{f}_1 \right) - \nabla \cdot \nabla \vec{f}_1 = 0 \quad . \tag{A.22}$$

Hence

$$\nabla \left(\nabla \cdot \vec{f}_1 \right) = \nabla \cdot \nabla \vec{f}_1 = \nabla^2 \vec{f}_1 \quad . \tag{A.23}$$

Substituting (A.23) into (A.19) yields

$$\rho \frac{\partial^2 \vec{f}_1}{\partial t^2} = (\lambda + 2\mu) \nabla^2 \vec{f}_1 \tag{A.24}$$

or

$$\frac{\partial^2 \vec{f}_1}{\partial t^2} = {c_L}^2 \nabla^2 \vec{f}_1 \tag{A.25}$$

where $c_L = \sqrt{\frac{\lambda + 2\mu}{\rho}}$ is the longitudinal wave velocity. The displacement $\vec{f}_1$ describes an *irrotational*, *compressional*, *longitudinal* or *P*-wave motion.

A.3.2 Shear wave

Consider a divergence-free displacement field $\vec{f} = \vec{f}_2$. Since

$$\nabla \cdot \vec{f} = \nabla \cdot \vec{f}_2 = 0 \quad , \tag{A.26}$$

equation (A.19) becomes

$$\rho \frac{\partial^2 \vec{f}_2}{\partial t^2} = \mu \nabla^2 \vec{f}_2 \tag{A.27}$$

or

$$\frac{\partial^2 \vec{f}_2}{\partial t^2} = {c_T}^2 \nabla^2 \vec{f}_2 \tag{A.28}$$

where $c_S = \sqrt{\frac{\mu}{\rho}}$ is the shear wave velocity. The displacement $\vec{f}_2$ describes a *rotational, transverse* or *S*- (shear) wave motion.

Following Udías (1999), there are two polarizations of *S*-waves. Consider an incident ray on the *x*-*z* plane (Figure A.2). The displacement of $\vec{f}_2$ motion perpendicular to the ray direction will be in the *x*-*z* plane and along the *y*-direction. The polarization in the *x*-*z* plane is known as *SV*-wave. It is a function of the *x* and *z* and can be determined by a potential ψ

$$u = -\frac{\partial \psi}{\partial z} \tag{A.29}$$

and

$$w = \frac{\partial \psi}{\partial x} \quad . \tag{A.30}$$

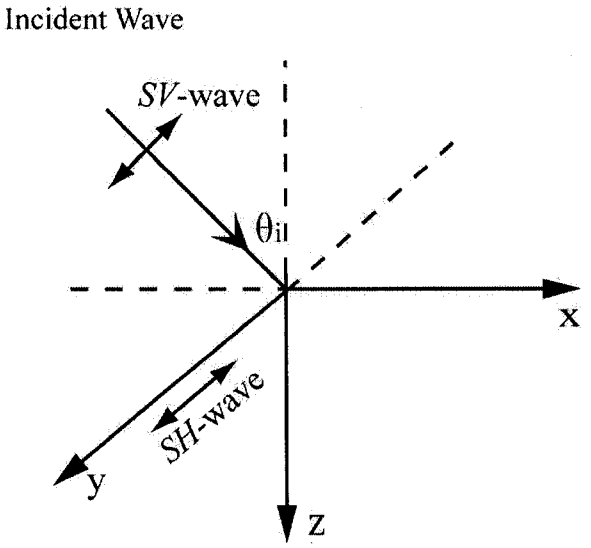

Figure A.2 Geometry and polarization of *S*-wave.

The polarization along the *y*-direction is known as *SH*-wave and can be determined by a potential Λ, which is a function of *x* and *z*

$$v = -\frac{\partial \Lambda}{\partial x} \quad . \tag{A.31}$$

Thus, the *S-wave* polarization can be written vectorially as

$$\vec{f}_2 = \nabla\times(0,\psi,0)+\nabla\times(0,0,\Lambda) \quad . \tag{A.32}$$

A.4 Reflection and transmission of P-SV waves across a solid-solid interface

When ultrasound encounters a solid-solid interface, the energy will be converted and split. Both *P*- and *S*-waves will be reflected and transmitted. In this section, we will derive the amplitude reflection and transmission coefficients for the incident *P*- and *S*-waves.

Consider two solid half-spaces in welded contact. The half-spaces are characterized by the densities, ρ_i, longitudinal wave velocities, c_{Li}, and shear wave velocities, c_{Si}, where i = 1 is the upper half-space and i = 2 is the lower half-space. As denoted by Figure A.3, there are 16 reflection/transmission coefficients corresponding to upgoing incident *P*- and *SV*-waves and downgoing incident *P*- and *SV*-waves. For notation, we denote the downgoing incident *P*-wave to upgoing reflected *P*-wave reflection coefficient as $\overset{\searrow}{P}_1\overset{\nearrow}{P}_1$ and $\overset{\searrow}{P}_1\overset{\nearrow}{S}_1$ is the downgoing incident *P*-wave to upgoing reflected *SV*-wave reflection coefficient. The corresponding transmission coefficients for the downgoing incident *P*-wave are $\overset{\searrow}{P}_1\overset{\searrow}{P}_2$ for the transmitted *P*-wave and $\overset{\searrow}{P}_1\overset{\searrow}{S}_2$ for the transmitted *SV*-wave respectively. For the other cases, the notations are self-explanatory.

Based on Figure A.3, we have the following displacement amplitudes for the four cases (Aki and Richard, 1980, pp.145-149).

Case 1: Downgoing incident *P*-wave (Figure A.3a)

Downgoing incident *P*-wave:

$$A_0\left(\sin\theta_{L1}, 0, \cos\theta_{L1}\right)\exp\left[i\omega\left(px+\frac{\cos\theta_{L1}}{c_{L1}}z-t\right)\right] \quad ,$$

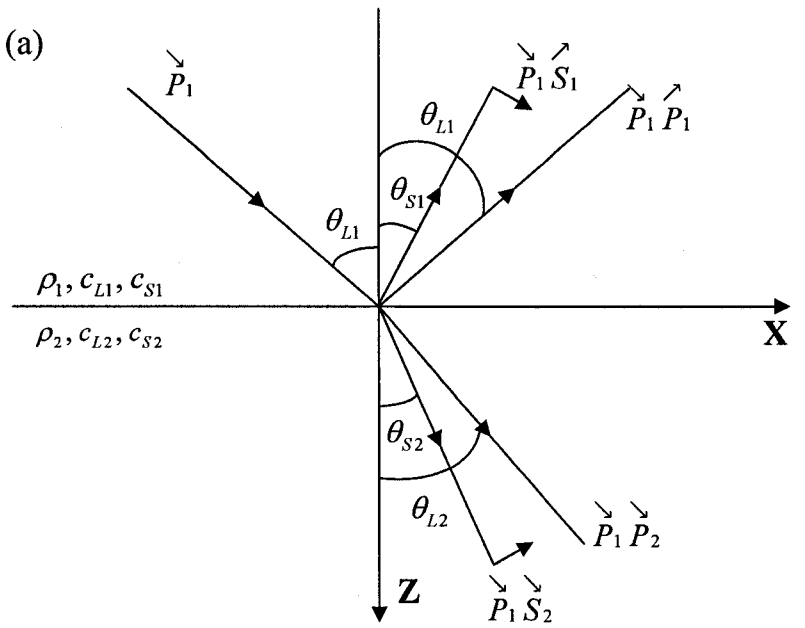
(a)
$\vec{P}_1$
$\vec{P}_1\vec{S}_1$
$\vec{P}_1\vec{P}_1$
θ_{L1}
θ_{S1}
θ_{L1}
ρ_1, c_{L1}, c_{S1}
ρ_2, c_{L2}, c_{S2}
X
θ_{S2}
θ_{L2}
$\vec{P}_1\vec{P}_2$
Z
$\vec{P}_1\vec{S}_2$

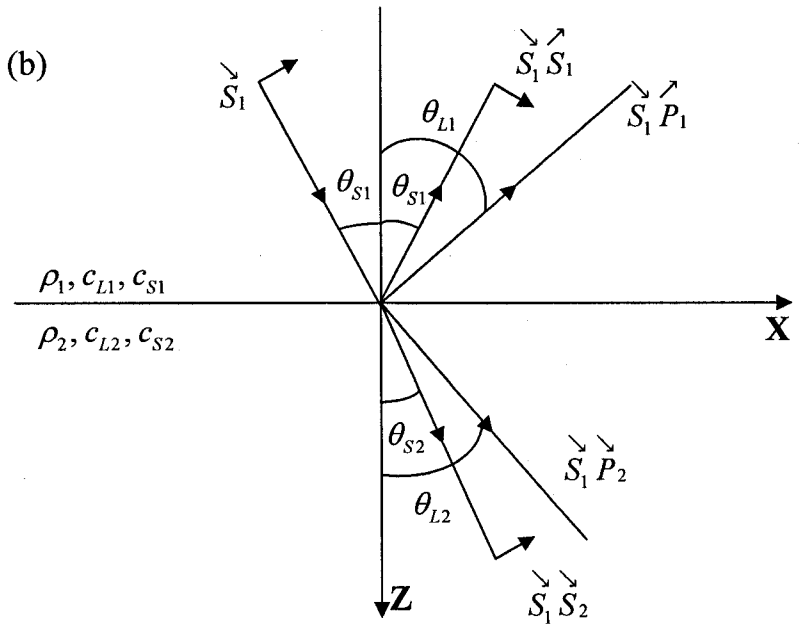
(b)
$\vec{S}_1$
$\vec{S}_1\vec{S}_1$
$\vec{S}_1\vec{P}_1$
θ_{L1}
θ_{S1}
θ_{S1}
ρ_1, c_{L1}, c_{S1}
ρ_2, c_{L2}, c_{S2}
X
θ_{S2}
$\vec{S}_1\vec{P}_2$
θ_{L2}
Z
$\vec{S}_1\vec{S}_2$

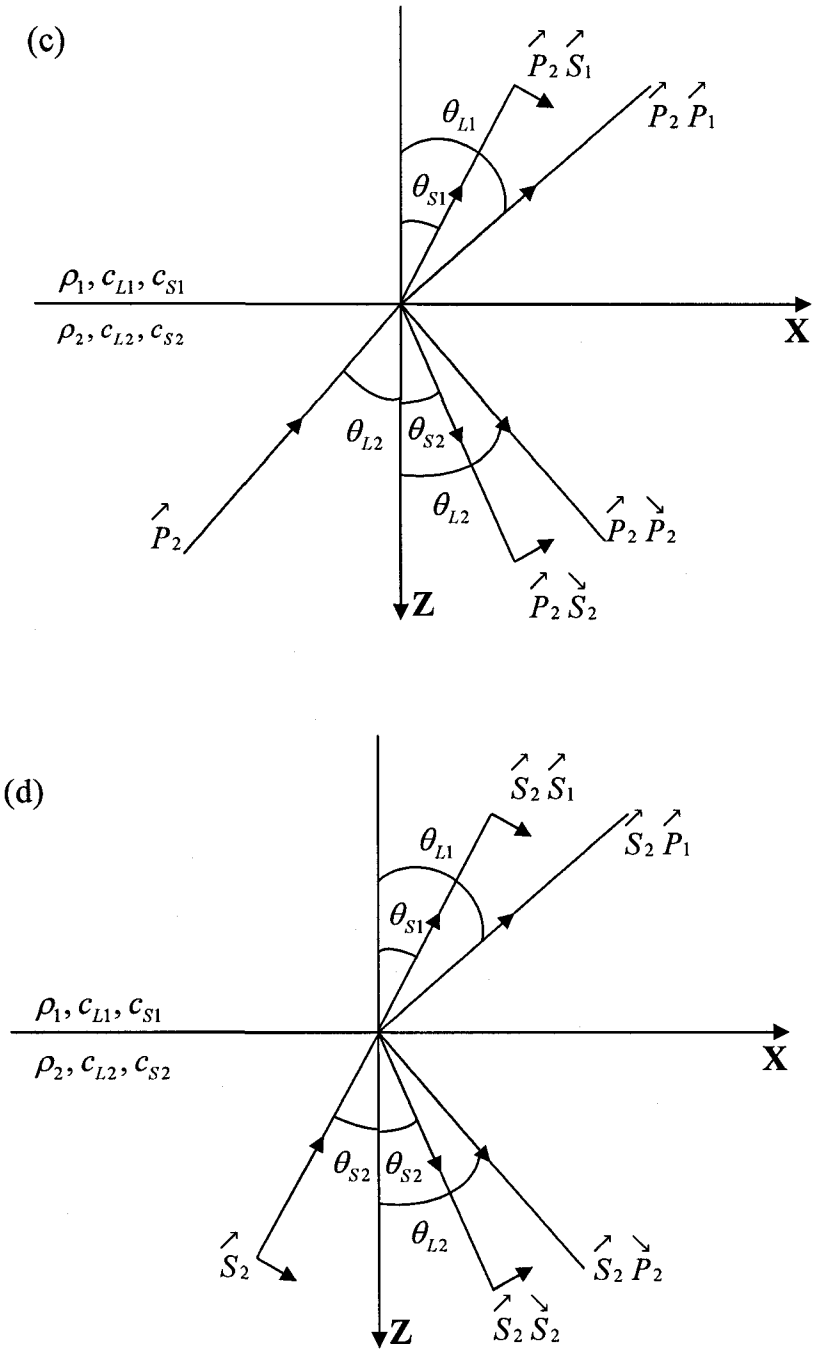

Figure A.3 Interaction of *P-SV* waves at the boundary of two solid-solid half-spaces: (a) Downgoing incident *P*-wave; (b) Downgoing incident *SV*-wave; (c) Upgoing incident *P*-wave; (d) Upgoing incident *SV*-wave.

Upgoing reflected *P*-wave:

$$A_0\left(\sin\theta_{L1}, 0, -\cos\theta_{L1}\right)\overset{\searrow}{P}_1\overset{\nearrow}{P}_1 \exp\left[i\omega\left(px - \frac{\cos\theta_{L1}}{c_{L1}}z - t\right)\right] \quad ,$$

Upgoing reflected *SV*-wave:

$$A_0\left(\cos\theta_{S1}, 0, \sin\theta_{S1}\right)\overset{\searrow}{P}_1\overset{\nearrow}{S}_1 \exp\left[i\omega\left(px - \frac{\cos\theta_{S1}}{c_{S1}}z - t\right)\right] \quad ,$$

Downgoing transmitted *P*-wave:

$$A_0\left(\sin\theta_{L2}, 0, \cos\theta_{L2}\right)\overset{\searrow}{P}_1\overset{\searrow}{P}_2 \exp\left[i\omega\left(px + \frac{\cos\theta_{L2}}{c_{L2}}z - t\right)\right] \quad ,$$

Downgoing transmitted *SV*-wave:

$$A_0\left(\cos\theta_{S2}, 0, -\sin\theta_{S2}\right)\overset{\searrow}{P}_1\overset{\searrow}{S}_2 \exp\left[i\omega\left(px + \frac{\cos\theta_{S2}}{c_{S2}}z - t\right)\right]$$

where A_0 is the incident amplitude and we have used the Snell's law

$$p = \frac{\sin\theta_{L1}}{c_{L1}} = \frac{\sin\theta_{S1}}{c_{S1}} = \frac{\sin\theta_{L2}}{c_{L2}} = \frac{\sin\theta_{S2}}{c_{S2}} \quad . \tag{A.33}$$

To determine the reflection/transmission coefficients: $\overset{\searrow}{P}_1\overset{\nearrow}{P}_1$, $\overset{\searrow}{P}_1\overset{\nearrow}{S}_1$, $\overset{\searrow}{P}_1\overset{\searrow}{P}_2$ and $\overset{\searrow}{P}_1\overset{\searrow}{S}_2$, we apply the boundary conditions.

(a) The displacements u and w are continuous at $z = 0$. Thus we have

$$\sin\theta_{L1} + \sin\theta_{L1}\overset{\searrow}{P}_1\overset{\nearrow}{P}_1 + \cos\theta_{S1}\overset{\searrow}{P}_1\overset{\nearrow}{S}_1 = \sin\theta_{L2}\overset{\searrow}{P}_1\overset{\searrow}{P}_2 + \cos\theta_{S2}\overset{\searrow}{P}_1\overset{\searrow}{S}_2 \quad , \tag{A.34}$$

and

$$\cos\theta_{L1} - \cos\theta_{L1}\overset{\searrow}{P}_1\overset{\nearrow}{P}_1 + \sin\theta_{S1}\overset{\searrow}{P}_1\overset{\nearrow}{S}_1 = \cos\theta_{L2}\overset{\searrow}{P}_1\overset{\searrow}{P}_2 - \sin\theta_{S2}\overset{\searrow}{P}_1\overset{\searrow}{S}_2 \quad . \tag{A.35}$$

(b) The stresses T_{zx} and T_{zz} are continuous at $z = 0$.

Since

$$T_{zx} = \mu\left(\frac{\partial u}{\partial z} + \frac{\partial w}{\partial x}\right) \tag{A.36}$$

and

$$T_{zz} = \lambda\left(\frac{\partial u}{\partial x} + \frac{\partial w}{\partial z}\right) + 2\mu\frac{\partial w}{\partial z} \quad , \tag{A.37}$$

we have

$$2\mu_1 p\cos\theta_{L1} - 2\mu_1 p\cos\theta_{L1}\overset{\searrow}{P}_1\overset{\nearrow}{P}_1 - \rho_1 c_{S1}\left(1-2c_{S1}^2p^2\right)\overset{\searrow}{P}_1\overset{\nearrow}{S}_1 = 2\mu_2 p\cos\theta_{L2}\overset{\searrow}{P}_1\overset{\searrow}{P}_2 + \rho_2 c_{S2}\left(1-2c_{S2}^2p^2\right)\overset{\searrow}{P}_1\overset{\searrow}{S}_2 \quad , \tag{A.38}$$

and

$$\rho_1 c_{L1}\left(1-2c_{S1}^2p^2\right) + \rho_1 c_{L1}\left(1-2c_{S1}^2p^2\right)\overset{\searrow}{P}_1\overset{\nearrow}{P}_1 - 2\rho_1 c_{S1}^2 p\cos\theta_{S1}\overset{\searrow}{P}_1\overset{\nearrow}{S}_1 = \rho_2 c_{L2}\left(1-2c_{S2}^2p^2\right)\overset{\searrow}{P}_1\overset{\searrow}{P}_2 - 2\rho_2 c_{S2}^2 p\cos\theta_{S2}\overset{\searrow}{P}_1\overset{\searrow}{S}_2 \quad . \tag{A.39}$$

The equations (A.34), (A.35), (A.38) and (A.39) can be expressed in matrix form:

$$\begin{bmatrix} -\sin\theta_{L1} & -\cos\theta_{S1} & \sin\theta_{L2} & \cos\theta_{S2} \\ \cos\theta_{L1} & -\sin\theta_{S1} & \cos\theta_{L2} & -\sin\theta_{S2} \\ 2\mu_1 p\cos\theta_{L1} & \rho_1 c_{S1}\left(1-2c_{S1}^2p^2\right) & 2\mu_2 p\cos\theta_{L2} & \rho_2 c_{S2}\left(1-2c_{S2}^2p^2\right) \\ -\rho_1 c_{L1}\left(1-2c_{S1}^2p^2\right) & 2\mu_1 p\cos\theta_{S1} & \rho_2 c_{L2}\left(1-2c_{S2}^2p^2\right) & -2\mu_2 p\cos\theta_{S2} \end{bmatrix} \cdot \begin{bmatrix} \overset{\searrow}{P}_1\overset{\nearrow}{P}_1 \\ \overset{\searrow}{P}_1\overset{\nearrow}{S}_1 \\ \overset{\searrow}{P}_1\overset{\searrow}{P}_2 \\ \overset{\searrow}{P}_1\overset{\searrow}{S}_2 \end{bmatrix}$$

$$= \begin{bmatrix} \sin\theta_{L1} \\ \cos\theta_{L1} \\ 2\mu_1 p\cos\theta_{L1} \\ \rho_1 c_{L1}\left(1-2c_{S1}^2p^2\right) \end{bmatrix} \tag{A.40}$$

or

$$\mathbf{M}\begin{bmatrix} \overset{\searrow}{P_1}\overset{\nearrow}{P_1} \\ \overset{\searrow}{P_1}\overset{\nearrow}{S_1} \\ \overset{\searrow}{P_1}\overset{\searrow}{P_2} \\ \overset{\searrow}{P_1}\overset{\searrow}{S_2} \end{bmatrix} = \begin{bmatrix} \sin\theta_{L1} \\ \cos\theta_{L1} \\ 2\mu_1 p\cos\theta_{L1} \\ \rho_1 c_{L1}\left(1-2c_{S1}^2 p^2\right) \end{bmatrix} \tag{A.41}$$

where

$$\mathbf{M} = \begin{bmatrix} -\sin\theta_{L1} & -\cos\theta_{S1} & \sin\theta_{L2} & \cos\theta_{S2} \\ \cos\theta_{L1} & -\sin\theta_{S1} & \cos\theta_{L2} & -\sin\theta_{S2} \\ 2\mu_1 p\cos\theta_{L1} & \rho_1 c_{S1}\left(1-2c_{S1}^2 p^2\right) & 2\mu_2 p\cos\theta_{L2} & \rho_2 c_{S2}\left(1-2c_{S2}^2 p^2\right) \\ -\rho_1 c_{L1}\left(1-2c_{S1}^2 p^2\right) & 2\mu_1 p\cos\theta_{S1} & \rho_2 c_{L2}\left(1-2c_{S2}^2 p^2\right) & -2\mu_2 p\cos\theta_{S2} \end{bmatrix}. \tag{A.42}$$

Case 2: Downgoing incident *SV*-wave (Figure A.3b)

Downgoing incident *SV*-wave:

$$A_0\left(\cos\theta_{S1}, 0, -\sin\theta_{S1}\right)\exp\left[i\omega\left(px + \frac{\cos\theta_{S1}}{c_{S1}}z - t\right)\right] \quad ,$$

Upgoing reflected *P*-wave:

$$A_0\left(\sin\theta_{L1}, 0, -\cos\theta_{L1}\right)\overset{\searrow}{S_1}\overset{\nearrow}{P_1}\exp\left[i\omega\left(px - \frac{\cos\theta_{L1}}{c_{L1}}z - t\right)\right] \quad ,$$

Upgoing reflected *SV*-wave:

$$A_0\left(\cos\theta_{S1}, 0, \sin\theta_{S1}\right)\overset{\searrow}{S_1}\overset{\nearrow}{S_1}\exp\left[i\omega\left(px - \frac{\cos\theta_{S1}}{c_{S1}}z - t\right)\right] \quad ,$$

Downgoing transmitted *P*-wave:

$$A_0\left(\sin\theta_{L2}, 0, \cos\theta_{L2}\right)\overset{\searrow}{S_1}\overset{\searrow}{P_2}\exp\left[i\omega\left(px + \frac{\cos\theta_{L2}}{c_{L2}}z - t\right)\right] \quad ,$$

Downgoing transmitted *SV*-wave:

$$A_0\left(\cos\theta_{S2}, 0, -\sin\theta_{S2}\right)\overset{\searrow}{S_1}\overset{\searrow}{S_2}\exp\left[i\omega\left(px + \frac{\cos\theta_{S2}}{c_{S2}}z - t\right)\right] \quad .$$

Using the same boundary conditions and following similarly the same steps as described above, we have

$$\mathbf{M}\begin{bmatrix} \overset{\searrow}{S_1}\overset{\nearrow}{P_1} \\ \overset{\searrow}{S_1}\overset{\nearrow}{S_1} \\ \overset{\searrow}{S_1}\overset{\searrow}{P_2} \\ \overset{\searrow}{S_1}\overset{\searrow}{S_2} \end{bmatrix} = \begin{bmatrix} \cos\theta_{S1} \\ -\sin\theta_{S1} \\ \rho_1 c_{S1}\left(1-2c_{S1}^2 p^2\right) \\ -2\mu_1 p\cos\theta_{S1} \end{bmatrix} . \qquad \text{(A.43)}$$

Case 3: Upgoing incident *P*-wave (Figure A.3c)

Upgoing incident *P*-wave:

$$A_0\left(\sin\theta_{L2}, 0, -\cos\theta_{L2}\right)\exp\left[i\omega\left(px-\frac{\cos\theta_{L2}}{c_{L2}}z-t\right)\right] ,$$

Upgoing transmitted *P*-wave:

$$A_0\left(\sin\theta_{L1}, 0, -\cos\theta_{L1}\right)\overset{\nearrow}{P_2}\overset{\nearrow}{P_1}\exp\left[i\omega\left(px-\frac{\cos\theta_{L1}}{c_{L1}}z-t\right)\right] ,$$

Upgoing transmitted *SV*-wave:

$$A_0\left(\cos\theta_{S1}, 0, \sin\theta_{S1}\right)\overset{\nearrow}{P_2}\overset{\nearrow}{S_1}\exp\left[i\omega\left(px-\frac{\cos\theta_{S1}}{c_{S1}}z-t\right)\right] ,$$

Downgoing reflected *P*-wave:

$$A_0\left(\sin\theta_{L2}, 0, \cos\theta_{L2}\right)\overset{\nearrow}{P_2}\overset{\searrow}{P_2}\exp\left[i\omega\left(px+\frac{\cos\theta_{L2}}{c_{L2}}z-t\right)\right] ,$$

Downgoing reflected *SV*-wave:

$$A_0\left(\cos\theta_{S2}, 0, -\sin\theta_{S2}\right)\overset{\nearrow}{P_2}\overset{\searrow}{S_2}\exp\left[i\omega\left(px+\frac{\cos\theta_{S2}}{c_{S2}}z-t\right)\right] .$$

Using the same boundary conditions and following similarly the same steps as described above, we have

$$\mathbf{M}\begin{bmatrix} \nearrow\ \nearrow \\ P_2\ P_1 \\ \nearrow\ \nearrow \\ P_2\ S_1 \\ \nearrow\ \searrow \\ P_2\ P_2 \\ \nearrow\ \searrow \\ P_2\ S_2 \end{bmatrix} = \begin{bmatrix} -\sin\theta_{S2} \\ \cos\theta_{S2} \\ 2\mu_2 p\cos\theta_{S2} \\ -\rho_2 c_{L2}\left(1-2c_{S2}^2 p^2\right) \end{bmatrix} . \qquad \text{(A.44)}$$

Case 4: Upgoing incident *SV*-wave (Figure A.3d)

Upgoing incident *SV*-wave:

$$A_0\left(\cos\theta_{S2}, 0, \sin\theta_{S2}\right)\exp\left[i\omega\left(px-\frac{\cos\theta_{S2}}{c_{S2}}z-t\right)\right] ,$$

Upgoing transmitted *P*-wave:

$$A_0\left(\sin\theta_{L1}, 0, -\cos\theta_{L1}\right)\overset{\nearrow}{S}_2\,\overset{\nearrow}{P}_1\exp\left[i\omega\left(px-\frac{\cos\theta_{L1}}{c_{L1}}z-t\right)\right] ,$$

Upgoing transmitted *SV*-wave:

$$A_0\left(\cos\theta_{S1}, 0, \sin\theta_{S1}\right)\overset{\nearrow}{S}_2\,\overset{\nearrow}{S}_1\exp\left[i\omega\left(px-\frac{\cos\theta_{S1}}{c_{S1}}z-t\right)\right] ,$$

Downgoing reflected *P*-wave:

$$A_0\left(\sin\theta_{L2}, 0, \cos\theta_{L2}\right)\overset{\nearrow}{S}_2\,\overset{\searrow}{P}_2\exp\left[i\omega\left(px+\frac{\cos\theta_{L2}}{c_{L2}}z-t\right)\right] ,$$

Downgoing reflected *SV*-wave:

$$A_0\left(\cos\theta_{S2}, 0, -\sin\theta_{S2}\right)\overset{\nearrow}{S}_2\,\overset{\searrow}{S}_2\exp\left[i\omega\left(px+\frac{\cos\theta_{S2}}{c_{S2}}z-t\right)\right]$$

Using the same boundary conditions and following similarly the same steps as described above, we have

$$\mathbf{M}\begin{bmatrix} \nearrow\ \nearrow \\ S_2\ P_1 \\ \nearrow\ \nearrow \\ S_2\ S_1 \\ \nearrow\ \searrow \\ S_2\ P_2 \\ \nearrow\ \searrow \\ S_2\ S_2 \end{bmatrix} = \begin{bmatrix} -\cos\theta_{S2} \\ -\sin\theta_{S2} \\ \rho_2 c_{S2}\left(1-2c_{S2}^2 p^2\right) \\ 2\mu_2 p\cos\theta_{S2} \end{bmatrix} . \tag{A.45}$$

To summarize equations (A.41), (A.43), (A.45) and (A.46), the four equations can be written as a matrix system

$$\mathbf{M}\cdot\begin{bmatrix} \searrow\ \nearrow & \searrow\ \nearrow & \nearrow\ \nearrow & \nearrow\ \nearrow \\ P_1\ P_1 & S_1\ P_1 & P_2\ P_1 & S_2\ P_1 \\ \searrow\ \nearrow & \searrow\ \nearrow & \nearrow\ \nearrow & \nearrow\ \nearrow \\ P_1\ S_1 & S_1\ S_1 & P_2\ S_1 & S_2\ S_1 \\ \searrow\ \searrow & \searrow\ \searrow & \nearrow\ \searrow & \nearrow\ \searrow \\ P_1\ P_2 & S_1\ P_2 & P_2\ P_2 & S_2\ P_2 \\ \searrow\ \searrow & \searrow\ \searrow & \nearrow\ \searrow & \nearrow\ \searrow \\ P_1\ S_2 & S_1\ S_2 & P_2\ S_2 & S_2\ S_2 \end{bmatrix} = \mathbf{N} \tag{A.46}$$

where

$$\mathbf{N} = \begin{bmatrix} \sin\theta_{L1} & \cos\theta_{S1} & -\sin\theta_{L2} & -\cos\theta_{S2} \\ \cos\theta_{L1} & -\sin\theta_{S1} & \cos\theta_{L2} & -\sin\theta_{S2} \\ 2\mu_1 p\cos\theta_{L1} & \rho_1 c_{S1}\left(1-2c_{S1}^2 p^2\right) & 2\mu_2 p\cos\theta_{S2} & \rho_2 c_{S2}\left(1-2c_{S2}^2 p^2\right) \\ \rho_1 c_{L1}\left(1-2c_{S1}^2 p^2\right) & -2\mu_1 p\cos\theta_{S1} & -\rho_2 c_{L2}\left(1-2c_{S2}^2 p^2\right) & 2\mu_2 p\cos\theta_{S2} \end{bmatrix} . \tag{A.47}$$

Therefore, the reflection/transmission coefficients are given by

$$\mathbf{M}^{-1}\mathbf{N} = \begin{bmatrix} \searrow\ \nearrow & \searrow\ \nearrow & \nearrow\ \nearrow & \nearrow\ \nearrow \\ P_1\ P_1 & S_1\ P_1 & P_2\ P_1 & S_2\ P_1 \\ \searrow\ \nearrow & \searrow\ \nearrow & \nearrow\ \nearrow & \nearrow\ \nearrow \\ P_1\ S_1 & S_1\ S_1 & P_2\ S_1 & S_2\ S_1 \\ \searrow\ \searrow & \searrow\ \searrow & \nearrow\ \searrow & \nearrow\ \searrow \\ P_1\ P_2 & S_1\ P_2 & P_2\ P_2 & S_2\ P_2 \\ \searrow\ \searrow & \searrow\ \searrow & \nearrow\ \searrow & \nearrow\ \searrow \\ P_1\ S_2 & S_1\ S_2 & P_2\ S_2 & S_2\ S_2 \end{bmatrix} . \tag{A.48}$$

Appendix B

The Cylindrical Coordinates

B.1 The Laplacian

The Laplacian of a vector $\vec{A}=(A_r, A_\theta, A_z)$ is defined by (Lorrain and Corson, 1970, pp.32)

$$\nabla^2\vec{A}=\nabla\left(\nabla\cdot\vec{A}\right)-\nabla\times\nabla\times\vec{A} \quad . \tag{B.1}$$

In cylindrical coordinates, (B.1) can be written vectorially as (Wolfram Mathworld, 2007, Pavlakovic and Love, 2001)

$$\begin{aligned}\nabla^2\vec{A}&=\left(\nabla^2A_r-\frac{2}{r^2}\frac{\partial A_\theta}{\partial\theta}-\frac{A_r}{r^2}\right)\hat{\mathbf{r}}+\left(\nabla^2A_\theta+\frac{2}{r^2}\frac{\partial A_r}{\partial\theta}-\frac{A_\theta}{r^2}\right)\hat{\boldsymbol{\theta}}+\left(\nabla^2A_z\right)\hat{\mathbf{z}}\\&=\left(\frac{\partial^2A_r}{\partial r^2}+\frac{1}{r^2}\frac{\partial^2A_r}{\partial\theta^2}+\frac{\partial^2A_r}{\partial z^2}+\frac{1}{r}\frac{\partial A_r}{\partial r}-\frac{2}{r^2}\frac{\partial A_\theta}{\partial\theta}-\frac{A_r}{r^2}\right)\hat{\mathbf{r}}+\\&\qquad\left(\frac{\partial^2A_\theta}{\partial r^2}+\frac{1}{r^2}\frac{\partial^2A_\theta}{\partial\theta^2}+\frac{\partial^2A_\theta}{\partial z^2}+\frac{1}{r}\frac{\partial A_\theta}{\partial r}+\frac{2}{r^2}\frac{\partial A_r}{\partial\theta}-\frac{A_\theta}{r^2}\right)\hat{\boldsymbol{\theta}}+\\&\qquad\left(\frac{\partial^2A_z}{\partial r^2}+\frac{1}{r^2}\frac{\partial^2A_z}{\partial\theta^2}+\frac{\partial^2A_z}{\partial z^2}+\frac{1}{r}\frac{\partial A_z}{\partial r}\right)\hat{\mathbf{z}}\end{aligned} \tag{B.2}$$

where $(\hat{\mathbf{r}},\hat{\boldsymbol{\theta}},\hat{\mathbf{z}})$ are the unit vectors in the cylindrical coordinate system and the Laplacian operator is $\nabla^2=\frac{\partial^2}{\partial r^2}+\frac{1}{r^2}\frac{\partial^2}{\partial\theta^2}+\frac{\partial^2}{\partial z^2}+\frac{1}{r}\frac{\partial}{\partial r}$.

B.2 Stress and strain components

The strain components in cylindrical coordinates are (Achenbach, 1975, pp.74)

$$\varepsilon_{rr} = \frac{\partial u_r}{\partial r} \quad , \tag{B.3}$$

$$\varepsilon_{\theta\theta} = \frac{1}{r}\frac{\partial u_\theta}{\partial \theta} + \frac{u_r}{r} \quad , \tag{B.4}$$

$$\varepsilon_{zz} = \frac{\partial u_z}{\partial z} \quad , \tag{B.5}$$

$$\varepsilon_{rz} = \varepsilon_{zr} = \frac{1}{2}\left(\frac{\partial u_r}{\partial z} + \frac{\partial u_z}{\partial r}\right) \quad , \tag{B.6}$$

$$\varepsilon_{r\theta} = \varepsilon_{\theta r} = \frac{1}{2}\left(\frac{\partial u_\theta}{\partial r} - \frac{u_\theta}{r} + \frac{1}{r}\frac{\partial u_r}{\partial \theta}\right) \quad , \tag{B.7}$$

and

$$\varepsilon_{\theta z} = \varepsilon_{z\theta} = \frac{1}{2}\left(\frac{\partial u_\theta}{\partial z} + \frac{1}{r}\frac{\partial u_z}{\partial \theta}\right) \quad . \tag{B.8}$$

The corresponding stresses are (Achenbach, 1975, pp.74-75; Kundu, 2003, pp.312-313)

$$\begin{aligned} T_{rr} &= \lambda\left(\varepsilon_{rr} + \varepsilon_{\theta\theta} + \varepsilon_{zz}\right) + 2\mu\varepsilon_{rr} \\ &= \lambda\left(\frac{\partial u_r}{\partial r} + \frac{u_r}{r} + \frac{1}{r}\frac{\partial u_\theta}{\partial \theta} + \frac{\partial u_z}{\partial z}\right) + 2\mu\frac{\partial u_r}{\partial r} \quad , \end{aligned} \tag{B.9}$$

$$\begin{aligned} T_{\theta\theta} &= \lambda\left(\varepsilon_{rr} + \varepsilon_{\theta\theta} + \varepsilon_{zz}\right) + 2\mu\varepsilon_{\theta\theta} \\ &= \lambda\left(\frac{\partial u_r}{\partial r} + \frac{u_r}{r} + \frac{1}{r}\frac{\partial u_\theta}{\partial \theta} + \frac{\partial u_z}{\partial z}\right) + 2\mu\left(\frac{u_r}{r} + \frac{1}{r}\frac{\partial u_\theta}{\partial \theta}\right) \quad , \end{aligned} \tag{B.10}$$

$$T_{zz} = \lambda\left(\varepsilon_{rr} + \varepsilon_{\theta\theta} + \varepsilon_{zz}\right) + 2\mu\varepsilon_{zz}$$
$$= \lambda\left(\frac{\partial u_r}{\partial r} + \frac{u_r}{r} + \frac{1}{r}\frac{\partial u_\theta}{\partial \theta} + \frac{\partial u_z}{\partial z}\right) + 2\mu\frac{\partial u_z}{\partial z} \quad , \tag{B.11}$$

$$T_{r\theta} = T_{\theta r} = 2\mu\varepsilon_{r\theta} = \mu\left(\frac{\partial u_\theta}{\partial r} - \frac{u_\theta}{r} + \frac{1}{r}\frac{\partial u_r}{\partial \theta}\right) \quad , \tag{B.12}$$

$$T_{\theta z} = T_{z\theta} = 2\mu\varepsilon_{\theta z} = \mu\left(\frac{1}{r}\frac{\partial u_z}{\partial \theta} + \frac{\partial u_\theta}{\partial z}\right) \quad , \tag{B.13}$$

and

$$T_{rz} = T_{zr} = 2\mu\varepsilon_{rz} = \mu\left(\frac{\partial u_r}{\partial z} + \frac{\partial u_z}{\partial r}\right) \quad . \tag{B.14}$$

Appendix C

Bessel functions and the derivatives

C.1 Bessel functions

Bessel's equation has many practical applications in areas such as elasticity, fluid dynamics and electromagnetic field. Bessel's equation is usually written as (Churchill and Brown, 1978, pp.174)

$$x^2 \frac{d^2y}{dx^2} + x\frac{dy}{dx} + \left(x^2 - n^2\right)y = 0 \tag{C.1}$$

or

$$\frac{d^2y}{dx^2} + \frac{1}{x}\frac{dy}{dx} + \left(1 - \frac{n^2}{x^2}\right)y = 0 \tag{C.2}$$

or

$$B_{n,x}(y) = 0 \tag{C.3}$$

where $B_{n,x}$ is the Bessel operator

$$B_{n,x} = \frac{d^2}{dx^2} + \frac{1}{x}\frac{d}{dx} + \left(1 - \frac{n^2}{x^2}\right) \quad . \tag{C.4}$$

The general solutions to the Bessel's equation (C.1) are known as Bessel functions of order n and have the general form when x is real

$$y(x) = C_1 J_n(x) + C_2 Y_n(x) \tag{C.5}$$

where J_n and Y_n are the Bessel function of the first and second kind of order n respectively.

Consider a differential equation

$$x^2\frac{d^2y}{dx^2}+x\frac{dy}{dx}-\left(x^2+n^2\right)y=0 \quad . \tag{C.6}$$

With the substitution $ix=t$ where x is real and $i^2=-1$ to (C.6), we obtain

$$t^2\frac{d^2y}{dt^2}+t\frac{dy}{dt}+\left(t^2-n^2\right)y=0 \quad , \tag{C.7}$$

which is the same as (C.1). Hence the general solutions of (C.7) are

$$y(x)=C_1J_n(t)+C_2Y_n(t) \tag{C.8}$$

or

$$y(x)=C_1J_n(ix)+C_2Y_n(ix) \tag{C.9}$$

where the argument of the Bessel function is imaginary. Conventionally, the general solutions of (C.6) can be written in the real form as

$$y(x)=C_1I_n(x)+C_2K_n(x) \tag{C.10}$$

where I_n and K_n are the modified Bessel function of the first and second kind of order n of a real argument x respectively.

With the substitution $x=ar$, (C.2) can be transformed into

$$\frac{d^2y}{dr^2}+\frac{1}{r}\frac{dy}{dr}-\left(\frac{n^2}{r^2}-a^2\right)y=0 \tag{C.11}$$

or

$$B_{n,ar}(y)=0 \tag{C.12}$$

where

$$B_{n,ar}=\frac{d^2}{dr^2}+\frac{1}{r}\frac{d}{dr}-\left(\frac{n^2}{r^2}-a^2\right) . \tag{C.13}$$

C.2 Derivatives of Bessel functions

The first and second derivatives of the first kind Bessel function of order n are given by (Moon and Spencer, 1961, pp.191)

$$\begin{aligned}\frac{dJ_n(x)}{dx}&=\frac{1}{x}\left[nJ_n(x)-xJ_{n+1}(x)\right]\\&=-\frac{1}{x}\left[nJ_n(x)-xJ_{n-1}(x)\right]\end{aligned} \tag{C.14}$$

and

$$\frac{d^2J_n(x)}{dx^2}=\left[\frac{n(n-1)}{x^2}-1\right]J_n(x)+\frac{1}{x}J_{n+1}(x) \tag{C.15}$$

respectively. For Bessel function of the second kind, equations (C.14) and (C.15) still apply with $J_n(x)$ replaced by $Y_n(x)$.

C.3 Derivatives of modified Bessel functions

The first and second derivatives of the first kind of the modified Bessel function is (McLachlan, 1934, pp.163)

$$\begin{aligned}\frac{dI_n(x)}{dx}&=\frac{1}{x}\left[nI_n(x)+xI_{n+1}(x)\right]\\&=\frac{1}{x}\left[xI_{n-1}(x)-nI_n(x)\right]\end{aligned} \tag{C.16}$$

and

$$\frac{d^2 I_n(x)}{dx^2} = \left[\frac{n(n-1)}{x^2} - 1\right] I_n(x) - \frac{1}{x} I_{n+1}(x) \tag{C.17}$$

respectively. For the second kind of the modified Bessel function, the first and second derivatives are (McLachlan, 1934, pp.165)

$$\begin{aligned} \frac{dK_n(x)}{dx} &= \frac{1}{x}\left[n K_n(x) - x K_{n+1}(x)\right] \\ &= -\frac{1}{x}\left[x K_{n-1}(x) + n K_n(x)\right] \end{aligned} \tag{C.18}$$

and

$$\frac{d^2 K_n(x)}{dx^2} = \left[\frac{n(n-1)}{x^2} - 1\right] K_n(x) + \frac{1}{x} K_{n+1}(x) \tag{C.19}$$

respectively.

Appendix D

On the Coefficient Matrix D

D.1 The element D_{ij}

The elements D_{ij} $(i, j = 1\ldots7)$ of the 7×7 matrix **D** referred by Equation (2.102) in Section 2.2 of the text are

$$D_{11} = \frac{\mu_c}{b^2}\left[\left(k^2 - q_c^2\right)b^2 + 2n(n-1)\right]Z_n(\hat{p}_c b) + \frac{2\gamma_1\mu_c\hat{p}_c}{b}Z_{n+1}(\hat{p}_c b) \quad , \tag{D.1}$$

$$D_{12} = \frac{\mu}{b^2}\left[\left(k^2 - q_c^2\right)b^2 + 2n(n-1)\right]W_n(\hat{p}_c b) + 2\frac{\mu_c\hat{p}_c}{b}W_{n+1}(\hat{p}_c b) \quad , \tag{D.2}$$

$$D_{13} = \frac{2\mu_c n(n-1)}{b^2}Z_n(\hat{q}_c b) - \frac{2\gamma_2\mu_c n\hat{q}_c}{b}Z_{n+1}(\hat{q}_c b) \quad , \tag{D.3}$$

$$D_{14} = \frac{2\mu_c n(n-1)}{b^2}W_n(\hat{q}_c b) - \frac{2\mu_c n\hat{q}_c}{b}W_{n+1}(\hat{q}_c b) \quad , \tag{D.4}$$

$$D_{15} = 2\mu_c k\hat{q}_c Z_n(\hat{q}_c b) - \frac{2\mu_c(n+1)k}{b}Z_{n+1}(\hat{q}_c b) \quad , \tag{D.5}$$

$$D_{16} = 2\gamma_2\mu_c k\hat{q}_c W_n(\hat{q}_c b) - \frac{2\mu_c(n+1)k}{b}W_{n+1}(\hat{q}_c b) \quad , \tag{D.6}$$

$$D_{17} = 0 \quad , \tag{D.7}$$

$$D_{21} = \frac{2\mu_c n(n-1)}{b^2}Z_n(\hat{p}_c b) - \frac{2\gamma_1\mu_c n\hat{p}_c}{b}Z_{n+1}(\hat{p}_c b) \quad , \tag{D.8}$$

$$D_{22} = \frac{2\mu_c n(n-1)}{b^2}W_n(\hat{p}_c b) - \frac{2\mu_c n\hat{p}_c}{b}W_{n+1}(\hat{p}_c b) \quad , \tag{D.9}$$

$$D_{23} = \frac{\mu_c}{b^2}\left[2n(n-1) - q_c^2 b^2\right]Z_n(\hat{q}_c b) + \frac{2\mu_c\gamma_2\hat{q}_c}{b}Z_{n+1}(\hat{q}_c b) \quad , \tag{D.10}$$

$$D_{24} = \frac{\mu_c}{b^2}\left[2n(n-1) - q_c^2 b^2\right] W_n(\hat{q}_c b) + \frac{2\mu_c \hat{q}_c}{b} W_{n+1}(\hat{q}_c b) \quad , \tag{D.11}$$

$$D_{25} = -k\hat{q}_c \mu_c Z_n(\hat{q}_c b) + \frac{2\mu_c k(n+1)}{b} Z_{n+1}(\hat{q}_c b) \quad , \tag{D.12}$$

$$D_{26} = -\gamma_2 k\hat{q}_c \mu_c W_n(\hat{q}_c b) + \frac{2\mu_c k(n+1)}{b} W_{n+1}(\hat{q}_c b) \quad , \tag{D.13}$$

$$D_{27} = 0 \quad , \tag{D.14}$$

$$D_{31} = \frac{2\mu_c nk}{b} Z_n(\hat{p}_c b) - 2\gamma_1 \mu_c k\hat{p}_c Z_{n+1}(\hat{p}_c b) \quad , \tag{D.15}$$

$$D_{32} = \frac{2\mu_c nk}{b} W_n(\hat{p}_c b) - 2\mu_c k\hat{p}_c W_{n+1}(\hat{p}_c b) \quad , \tag{D.16}$$

$$D_{33} = \frac{\mu_c nk}{b} Z_n(\hat{q}_c b) \quad , \tag{D.17}$$

$$D_{34} = \frac{\mu_c nk}{b} W_n(\hat{q}_c b) \quad , \tag{D.18}$$

$$D_{35} = \frac{\mu_c n\hat{q}_c}{b} Z_n(\hat{q}_c b) + \mu_c\left(k^2 - q_c^2\right) Z_{n+1}(\hat{q}_c b) \quad , \tag{D.19}$$

$$D_{36} = \frac{\gamma_1 \mu_c n\hat{q}_c}{b} W_n(\hat{q}_c b) + \mu_c\left(k^2 - q_c^2\right) W_{n+1}(\hat{q}_c b) \tag{D.20}$$

$$D_{37} = 0 \quad , \tag{D.21}$$

$$D_{41} = \frac{\mu_c}{a^2}\left[\left(k^2 - q_c^2\right)a^2 + 2n(n-1)\right] Z_n(\hat{p}_c a) + \frac{2\gamma_1 \mu_c \hat{p}_c}{a} Z_{n+1}(\hat{p}_c a) \quad , \tag{D.22}$$

$$D_{42} = \frac{\mu_c}{a^2}\left[\left(k^2 - q_c^2\right)a^2 + 2n(n-1)\right] W_n(\hat{p}_c a) + \frac{2\mu_c \hat{p}_c}{a} W_{n+1}(\hat{p}_c a) \quad , \tag{D.23}$$

$$D_{43} = \frac{2\mu_c n(n-1)}{a^2} Z_n(\hat{q}_c a) - \frac{2\gamma_2 \mu_c n\hat{q}_c}{a} Z_{n+1}(\hat{q}_c a) \quad , \tag{D.24}$$

$$D_{44} = \frac{2\mu_c n(n-1)}{a^2} W_n(\hat{q}_c a) - \frac{2\mu_c n\hat{q}_c}{a} W_{n+1}(\hat{q}_c a) \quad , \tag{D.25}$$

$$D_{45} = 2\mu_c k\hat{q}_c Z_n(\hat{q}_c a) - \frac{2\mu_c k(n+1)}{a} Z_{n+1}(\hat{q}_c a) \quad , \tag{D.26}$$

$$D_{46} = 2\gamma_2 \mu_c k \hat{q}_c W_n(\hat{q}_c a) - \frac{2\mu_c k(n+1)}{a} W_{n+1}(\hat{q}_c a) \quad , \tag{D.27}$$

$$D_{47} = \lambda_f \left(p_f^2 + k^2\right) Z_n(\hat{p}_f r) \quad , \tag{D.28}$$

$$D_{51} = \frac{2\mu_c n(n-1)}{a^2} Z_n(\hat{p}_c a) - \frac{2\gamma_1 \mu_c n \hat{p}_c}{a} Z_{n+1}(\hat{p}_c a) \quad , \tag{D.29}$$

$$D_{52} = \frac{2\mu_c n(n-1)}{a^2} W_n(\hat{p}_c a) - \frac{2\mu_c n \hat{p}_c}{a} W_{n+1}(\hat{p}_c a) \quad , \tag{D.30}$$

$$D_{53} = \frac{\mu_c}{a^2}\left[2n(n-1) - q_c^2 a^2\right] Z_n(\hat{q}_c a) + \frac{2\gamma_2 \mu_c \hat{q}_c}{a} Z_{n+1}(\hat{q}_c a) \quad , \tag{D.31}$$

$$D_{54} = \frac{\mu_c}{a^2}\left[2n(n-1) - q_c^2 a^2\right] W_n(\hat{q}_c a) + \frac{2\mu_c \hat{q}_c}{a} W_{n+1}(\hat{q}_c a) \quad , \tag{D.32}$$

$$D_{55} = -\mu_c k \hat{q}_c Z_n(\hat{q}_c a) + \frac{2\mu_c k(n+1)}{a} Z_{n+1}(\hat{q}_c a) \quad , \tag{D.33}$$

$$D_{56} = -\gamma_2 \mu_c k \hat{q}_c W_n(\hat{q}_c a) + \frac{2\mu_c k(n+1)}{a} W_{n+1}(\hat{q}_c a) \quad , \tag{D.34}$$

$$D_{57} = 0 \quad , \tag{D.35}$$

$$D_{61} = \frac{2\mu_c nk}{a} Z_n(\hat{p}_c a) - 2\gamma_1 \mu_c k \hat{p}_c Z_{n+1}(\hat{p}_c a) \quad , \tag{D.36}$$

$$D_{62} = \frac{2\mu_c nk}{a} W_n(\hat{p}_c a) - 2\mu_c k \hat{p}_c W_{n+1}(\hat{p}_c a) \quad , \tag{D.37}$$

$$D_{63} = \frac{\mu_c nk}{a} Z_n(\hat{q}_c a) \quad , \tag{D.38}$$

$$D_{64} = \frac{\mu_c nk}{a} W_n(\hat{q}_c a) \quad , \tag{D.39}$$

$$D_{65} = \frac{\mu_c n \hat{q}_c}{a} Z_n(\hat{q}_c a) + \mu_c\left(k^2 - q_c^2\right) Z_{n+1}(\hat{q}_c a) \quad , \tag{D.40}$$

$$D_{66} = \frac{\gamma_2 \mu_c n \hat{q}_c}{a} W_n(\hat{q}_c a) - \mu_c\left(k^2 - q_c^2\right) W_{n+1}(\hat{q}_c a) \quad , \tag{D.41}$$

$$D_{67} = 0 \quad , \tag{D.42}$$

$$D_{71} = \frac{n}{a} Z_n(\hat{p}_c a) - \gamma_1 \hat{p}_c Z_{n+1}(\hat{p}_c a) \quad , \tag{D.43}$$

$$D_{72} = \frac{n}{a} W_n(\hat{p}_c a) - \hat{p}_c W_{n+1}(\hat{p}_c a) \quad , \tag{D.44}$$

$$D_{73} = \frac{nk}{a} Z_n(\hat{q}_c a) \quad , \tag{D.45}$$

$$D_{74} = \frac{n}{a} W_n(\hat{q}_c a) \quad , \tag{D.46}$$

$$D_{75} = k Z_n(\hat{q}_c a) \quad , \tag{D.47}$$

$$D_{76} = k W_n(\hat{q}_c a) \quad , \tag{D.48}$$

$$D_{77} = \hat{p}_f Z_{n+1}(\hat{p}_f a) - \frac{n}{a} Z_n(\hat{p}_f a) \tag{D.49}$$

where the parameters are described in Section 2.2 of the text.

The parameters γ_1 and γ_2 are introduced for different choice of Bessel functions. The first parameter, γ_1, relates to terms that involve $\hat{p}$ and the γ_2 relates to those that involve $\hat{q}$. These parameters equal to -1 when the modified Bessel functions I_n and K_n are used and equal to 1 otherwise. The following is an example.

Considering the first and second kind of Bessel function as the solution to (2.61)-(2.63), then

$$f = A_1 J_n(\hat{p}r) + B_1 Y_n(\hat{p}r) \quad , \tag{D.50}$$

$$h_z = A_2 J_n(\hat{q}r) + B_2 Y_n(\hat{q}r) \quad , \tag{D.51}$$

and

$$h_1 = A_3 J_{n+1}(\hat{q}r) + B_3 Y_{n+1}(\hat{q}r) \quad . \tag{D.52}$$

Substituting (D.50)-(D.52) to (2.95), we obtain

$$\lambda_c\left(p_c^2+k^2\right)\left[A_1J_n\left(\hat{p}_cr\right)+B_1Y_n\left(\hat{p}_cr\right)\right]-$$
$$2\mu_c\left\{\left[A_1J_n''\left(\hat{p}_cr\right)+B_1Y_n''\left(\hat{p}_cr\right)\right]+\frac{n}{r}\left[A_2J_n'\left(\hat{q}_cr\right)+B_2Y_n'\left(\hat{q}_cr\right)\right]-\right. \tag{D.53}$$
$$\left.\frac{n}{r^2}\left[A_2J_n\left(\hat{q}_cr\right)+B_2Y_n\left(\hat{q}_cr\right)\right]+k\left[A_3J_{n+1}'\left(\hat{q}_cr\right)+B_3Y_{n+1}'\left(\hat{q}_cr\right)\right]\right\}\Big|_{r=b}=0 \quad .$$

Using equations (C.14) and (C.15), the coefficient D_{ij} of A_1, B_1, A_2, B_2, A_3 and B_3 are

$$D_{11}=\frac{\mu_c}{b^2}\left[\left(k^2-q_c^2\right)b^2+2n\left(n-1\right)\right]J_n\left(\hat{p}_cb\right)+\frac{2\mu_c\hat{p}_c}{b}J_{n+1}\left(\hat{p}_cb\right) \quad , \tag{D.54}$$

$$D_{12}=\frac{\mu}{b^2}\left[\left(k^2-q_c^2\right)b^2+2n\left(n-1\right)\right]Y_n\left(\hat{p}_cb\right)+2\frac{\mu_c\hat{p}_c}{b}Y_{n+1}\left(\hat{p}_cb\right) \quad , \tag{D.55}$$

$$D_{13}=\frac{2\mu_cn(n-1)}{b^2}J_n\left(\hat{q}_cb\right)-\frac{2\mu_cn\hat{q}_c}{b}J_{n+1}\left(\hat{q}_cb\right) \quad , \tag{D.56}$$

$$D_{14}=\frac{2\mu_cn(n-1)}{b^2}Y_n\left(\hat{q}_cb\right)-\frac{2\mu_cn\hat{q}_c}{b}Y_{n+1}\left(\hat{q}_cb\right) \quad , \tag{D.57}$$

$$D_{15}=2\mu_ck\hat{q}_cJ_n\left(\hat{q}_cb\right)-\frac{2\mu_c(n+1)k}{b}J_{n+1}\left(\hat{q}_cb\right) \quad , \tag{D.58}$$

$$D_{16}=2\mu_ck\hat{q}_cY_n\left(\hat{q}_cb\right)-\frac{2\mu_c(n+1)k}{b}Y_{n+1}\left(\hat{q}_cb\right) \quad . \tag{D.59}$$

Considering the first and second kind of modified Bessel functions as the solutions to (2.61)-(2.63), the equations are written as

$$f=A_1I_n\left(\hat{p}r\right)+B_1K_n\left(\hat{p}r\right) \quad , \tag{D.60}$$

$$h_z=A_2I_n\left(\hat{q}r\right)+B_2K_n\left(\hat{q}r\right) \quad , \tag{D.61}$$

and

$$h_1=A_3I_{n+1}\left(\hat{q}r\right)+B_3K_{n+1}\left(\hat{q}r\right) \quad . \tag{D.62}$$

Substituting (D.50)-(D.52) to (2.95), we obtain

$$\lambda_c\left(p_c^2+k^2\right)\left[A_1 I_n\left(\hat{p}_c r\right)+B_1 K_n\left(\hat{p}_c r\right)\right]-$$
$$2\mu_c\left\{\left[A_1 I_n''\left(\hat{p}_c r\right)+B_1 K_n''\left(\hat{p}_c r\right)\right]+\frac{n}{r}\left[A_2 I_n'\left(\hat{q}_c r\right)+B_2 K_n'\left(\hat{q}_c r\right)\right]-\right. \tag{D.63}$$
$$\left.\frac{n}{r^2}\left[A_2 K_n\left(\hat{q}_c r\right)+B_2 K_n\left(\hat{q}_c r\right)\right]+k\left[A_3 I_{n+1}'\left(\hat{q}_c r\right)+B_3 K_{n+1}'\left(\hat{q}_c r\right)\right]\right\}\Big|_{r=b}=0 \quad .$$

Using equations (C.16)-(C.19), the coefficient D_{ij} of A_1, B_1, A_2, B_2, A_3 and B_3 are

$$D_{11}=\frac{\mu_c}{b^2}\left[\left(k^2-q_c^2\right)b^2+2n(n-1)\right]I_n\left(\hat{p}_c b\right)-\frac{2\mu_c\hat{p}_c}{b}I_{n+1}\left(\hat{p}_c b\right) \quad , \tag{D.64}$$

$$D_{12}=\frac{\mu}{b^2}\left[\left(k^2-q_c^2\right)b^2+2n(n-1)\right]K_n\left(\hat{p}_c b\right)+2\frac{\mu_c\hat{p}_c}{b}K_{n+1}\left(\hat{p}_c b\right) \quad , \tag{D.65}$$

$$D_{13}=\frac{2\mu_c n(n-1)}{b^2}I_n\left(\hat{q}_c b\right)+\frac{2\mu_c n\hat{q}_c}{b}I_{n+1}\left(\hat{q}_c b\right) \quad , \tag{D.66}$$

$$D_{14}=\frac{2\mu_c n(n-1)}{b^2}K_n\left(\hat{q}_c b\right)-\frac{2\mu_c n\hat{q}_c}{b}K_{n+1}\left(\hat{q}_c b\right) \quad , \tag{D.67}$$

$$D_{15}=2\mu_c k\hat{q}_c I_n\left(\hat{q}_c b\right)-\frac{2\mu_c(n+1)k}{b}I_{n+1}\left(\hat{q}_c b\right) \quad , \tag{D.68}$$

$$D_{16}=-2\mu_c k\hat{q}_c K_n\left(\hat{q}_c b\right)-\frac{2\mu_c(n+1)k}{b}K_{n+1}\left(\hat{q}_c b\right) \quad . \tag{D.69}$$

In terms of Z_n and W_n, (D.54) and (D.64) can be written as (D.1)

$$D_{11}=\frac{\mu_c}{b^2}\left[\left(k^2-q_c^2\right)b^2+2n(n-1)\right]Z_n\left(\hat{p}_c b\right)+\frac{2\gamma_1\mu_c\hat{p}_c}{b}Z_{n+1}\left(\hat{p}_c b\right)$$

where $\gamma_1 = 1$ when Z_n is J_n or $\gamma_1 = -1$ when Z_n is I_n. Similarly, (D.56) and (D.66) can be written as (D.3)

$$D_{13}=\frac{2\mu_c n(n-1)}{b^2}Z_n\left(\hat{q}_c b\right)-\frac{2\gamma_2\mu_c n\hat{q}_c}{b}Z_{n+1}\left(\hat{q}_c b\right)$$

where $\gamma_2 = 1$ when Z_n is J_n or $\gamma_2 = -1$ when Z_n is I_n. (D.59) and (D.69) can be written as (D.6)

$$D_{16} = 2\gamma_2 \mu_c k \hat{q}_c W_n(\hat{q}_c b) - \frac{2\mu_c (n+1)k}{b} W_{n+1}(\hat{q}_c b)$$

where $\gamma_2 = 1$ when W_n is Y_n or $\gamma_2 = -1$ when W_n is K_n.

D.2 The determinant of D when $n = 0$

When n=0, the determinant of D becomes

$$\det(\mathbf{D}) = \begin{vmatrix} D_{11} & D_{12} & D_{13} & D_{14} & D_{15} & D_{16} & D_{17} \\ D_{21} & D_{22} & D_{23} & D_{24} & D_{25} & D_{26} & D_{27} \\ D_{31} & D_{32} & D_{33} & D_{34} & D_{35} & D_{36} & D_{37} \\ D_{41} & D_{42} & D_{43} & D_{44} & D_{45} & D_{46} & D_{47} \\ D_{51} & D_{52} & D_{53} & D_{54} & D_{55} & D_{56} & D_{57} \\ D_{61} & D_{62} & D_{63} & D_{64} & D_{65} & D_{66} & D_{67} \\ D_{71} & D_{72} & D_{73} & D_{74} & D_{75} & D_{76} & D_{77} \end{vmatrix}$$

$$= \begin{vmatrix} D_{11} & D_{12} & 0 & 0 & D_{15} & D_{16} & 0 \\ 0 & 0 & D_{23} & D_{24} & D_{25} & D_{26} & 0 \\ D_{31} & D_{32} & 0 & 0 & D_{35} & D_{36} & 0 \\ D_{41} & D_{42} & 0 & 0 & D_{45} & D_{46} & D_{47} \\ 0 & 0 & D_{53} & D_{54} & D_{55} & D_{56} & 0 \\ D_{61} & D_{62} & 0 & 0 & D_{65} & D_{66} & 0 \\ D_{71} & D_{72} & 0 & 0 & D_{75} & D_{76} & D_{77} \end{vmatrix}$$

$$= \begin{vmatrix} D_{11} & D_{12} & D_{15} & D_{16} & 0 & 0 & 0 \\ D_{31} & D_{32} & D_{35} & D_{36} & 0 & 0 & 0 \\ D_{41} & D_{42} & D_{45} & D_{46} & D_{47} & 0 & 0 \\ D_{61} & D_{62} & D_{65} & D_{66} & 0 & 0 & 0 \\ D_{71} & D_{72} & D_{75} & D_{76} & D_{77} & 0 & 0 \\ 0 & 0 & D_{25} & D_{26} & 0 & D_{23} & D_{24} \\ 0 & 0 & D_{55} & D_{56} & 0 & D_{53} & D_{54} \end{vmatrix} \tag{D.70}$$

where we have used the property $\det(\mathbf{D}') = -\det(\mathbf{D})$ if $\mathbf{D}'$ is the matrix that results when two rows or columns are interchanged. Using Cramer's rule (Anton, 1981, pp. 69-84),

$$\det(\mathbf{D}) = \begin{vmatrix} D_{11} & D_{12} & D_{15} & D_{16} & 0 & 0 & 0 \\ D_{31} & D_{32} & D_{35} & D_{36} & 0 & 0 & 0 \\ D_{41} & D_{42} & D_{45} & D_{46} & D_{47} & 0 & 0 \\ D_{61} & D_{62} & D_{65} & D_{66} & 0 & 0 & 0 \\ D_{71} & D_{72} & D_{75} & D_{76} & D_{77} & 0 & 0 \\ 0 & 0 & D_{25} & D_{26} & 0 & D_{23} & D_{24} \\ 0 & 0 & D_{55} & D_{56} & 0 & D_{53} & D_{54} \end{vmatrix}$$

$$= D_{23} D_{54} \begin{vmatrix} D_{11} & D_{12} & D_{15} & D_{16} & 0 \\ D_{31} & D_{32} & D_{35} & D_{36} & 0 \\ D_{41} & D_{42} & D_{45} & D_{46} & D_{47} \\ D_{61} & D_{62} & D_{65} & D_{66} & 0 \\ D_{71} & D_{72} & D_{75} & D_{76} & D_{77} \end{vmatrix} - D_{53} D_{24} \begin{vmatrix} D_{11} & D_{12} & D_{15} & D_{16} & 0 \\ D_{31} & D_{32} & D_{35} & D_{36} & 0 \\ D_{41} & D_{42} & D_{45} & D_{46} & D_{47} \\ D_{61} & D_{62} & D_{65} & D_{66} & 0 \\ D_{71} & D_{72} & D_{75} & D_{76} & D_{77} \end{vmatrix}$$

$$= \begin{vmatrix} D_{11} & D_{12} & D_{15} & D_{16} & 0 \\ D_{31} & D_{32} & D_{35} & D_{36} & 0 \\ D_{41} & D_{42} & D_{45} & D_{46} & D_{47} \\ D_{61} & D_{62} & D_{65} & D_{66} & 0 \\ D_{71} & D_{72} & D_{75} & D_{76} & D_{77} \end{vmatrix} \begin{vmatrix} D_{23} & D_{24} \\ D_{53} & D_{54} \end{vmatrix} . \qquad \text{(D.71)}$$